

Institute of Medical Engineering and Medical Physics
Cardiff University



In-Vivo Biomechanical Properties of Kager's Fat Pad: Investigating Previous Hypotheses

A thesis submitted for the Degree of Philosophy Doctorate
August 2010

Written by: Ahmad Ali Ghazzawi
Supervisors: Prof. L D M Nokes
Dr. C B Byrne

UMI Number: U518158

All rights reserved

INFORMATION TO ALL USERS

The quality of this reproduction is dependent upon the quality of the copy submitted.

In the unlikely event that the author did not send a complete manuscript and there are missing pages, these will be noted. Also, if material had to be removed, a note will indicate the deletion.



UMI U518158

Published by ProQuest LLC 2013. Copyright in the Dissertation held by the Author.
Microform Edition © ProQuest LLC.

All rights reserved. This work is protected against
unauthorized copying under Title 17, United States Code.



ProQuest LLC
789 East Eisenhower Parkway
P.O. Box 1346
Ann Arbor, MI 48106-1346

Acknowledgements

To the late Mr Ali Atta Ghazzawi whose support and dedication were always unparalleled. To my family whose patience, support and financial security made it possible to complete this PhD.

It has been a great pleasure to have Prof Len Nokes & Dr Carl Byrne as my supervisors for being extremely supportive and encouraging in every stage of this research. I am grateful to have learned a great deal from them.

Many thanks also go out to Dr Neil Pugh, Cardiff & Vale Hospital NHS Trust, for his guidance to use the ultrasound machine, and for his invaluable insight to imaging analysis and research.

A special thanks to Matthew Beasley whose comments made the drafts into a thesis.

Last but not least, to all the groups whose support was constructive, namely MRI Unit at the Medical Engineering and Medical Physics, Cardiff University Brain Research & Imaging Centre (CUBRIC), and the School of Engineering mechanical workshop, Thank you!

Declaration

This work has not previously been accepted in substance for any degree and is not concurrently submitted in candidature for any other higher degree.

Signed: .....(Candidate) Date: 7/6/2011.....

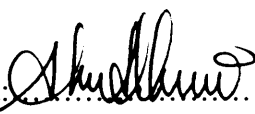
Statement 1

This thesis is being submitted in partial fulfilment of the requirements for the degree of ...PhD.....(insert as appropriate PhD, MPhil, EngD)

Signed: .....(Candidate) Date: 7/6/2011.....

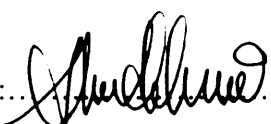
Statement 2

This thesis is the result of my own independent work/investigation, except where otherwise stated. Other sources are acknowledged by explicit references.

Signed: .....(Candidate) Date: 7/6/2011.....

Statement 3

I hereby give consent for my thesis, if accepted, to be available for photocopying, inter-library loan and for the title and summary to be made available to outside organisations.

Signed: .....(Candidate) Date: 7/6/2011.....

Summary

Kager's fat pad (KFP) is located in Kager's triangle between the Achilles tendon (AT), the calcaneal superior tuberosity (CST) and Flexor Hallucis Longus (FHL) muscle & tendon. Although the consequences of its removal are unclear, KFP can be subjected to removal for arthroscopic access. The biomechanical functions of KFP were not established by previous studies. However, literature review showed that KFP is lined by a synovial membrane, its posterior-distal wedge (described in this study as the protruding wedge (PW)) shares the superior wall of the retrocalcaneal bursa (RB) and it can be observed moving into and out of the bursal space during ankle plantarflexion and dorsiflexion respectively. KFP was also shown to contain blood vessels and neural supply. Such features prompted hypotheses that KFP performs important biomechanical roles including assisting in the lubrication of the AT subtendinous area, distributes stress at the AT enthesis, acts to protect AT vascular supply, distributes the retrocalcaneal bursal pressure, assists in load bearing and removes debris from within the retrocalcaneal bursa caused by wear and tear.

KFP has come under increasing investigation since strong indications were found that it serves as more than just a space filler, to further understand its biomechanical functionality within AT enthesis organ. KFP is found to have anchorage to the surrounding tissues, located in encapsulated (or 'air tight') regions, lined by synovial membranes and slide within its respective motion ranges. On the other hand, while histological studies found fibrosis tissue as the main content of the knee meniscus, it can only be found in the tip of KFP's PW. Blood vessels can be found in the proximal region of KFP. To assist in further understanding the in-vivo biomechanical functions of KFP within AT enthesis organ, a number of studies were carried out, initially utilizing testing methods previously used to establish functions of the knee meniscus and initial studies on KFP.

A previous study hypothesized a number of techniques to control the motion of PW during ankle flexion including: (i) FHL muscle activities, (ii) displacement of the Calcaneus bone, or (iii) pressure change within the retrocalcaneal bursa. Consequently, this research first examined the influence of FHL activity and ankle activity type on KFP's motion using both dynamic ultrasound imaging and surface Electromyogram (sEMG). Inter-volunteer results showed PW's sliding distance (PWSD) was independent of FHL activities. Additionally, PWSD was found to increase with increasing load on AT (in the plantarflexion direction). It was also noted that PWSD was dependant on a change in the AT insertion angle, which acts

to change the pressure within the retrocalcaneal bursa, supporting hypotheses that PW's motion is influenced by the change in pressure within RB.

Further testing examined load and flexion angle influences on KFP's motion and sliding distance. Results showed that PW slides to its maximum range when the ankle is flexed in the plantarflexion direction against loads of 2 kgs and over. A strong relation was also found between AT insertion angle and the location of PW's tip. A hysteresis of PW was observed in this study, as the tip of PW was lagging during its motion. Therefore, the hysteresis was tested with a high refresh rate (36 fps). Results showed PW hysteresis is evident, with no clear statistical relation to load and flexion pace AT. Furthermore, the thickness of PW was found to decrease during dorsiflexion and increase in the ankle plantarflexion direction. Magnetic resonance imaging (MRI) was used to study shape, area, and volume changes of KFP between ankle plantarflexion and neutral positions. Although area in the sagittal plane appeared to decrease on average by 10% (SD = 2.4%) between ankle plantarflexion and neutral positions, no obvious volume changes were detected as the area of KFP in the transverse plane increased from ankle plantarflexion to neutral positions by approximately 10.2% (SD = 2.14%), which indicates that KFP behaves as a non-compressible tissue in-vivo. This, in addition to the existence of fibrosis in PW's tip, support hypotheses that PW can assist in load bearing within the AT enthesis organ. AT bends were observed in this study using US scanning, and were typically found when the ankle was flexed passively or actively against low loads (0-1 kg). AT kinks were found typically below the KFP anchorage to AT and only momentarily (max of 0.2s), suggesting KFP can reduce AT kinking during flexion. This research helped establish and support speculations that KFP provides important functions to the AT enthesis organ. The consequences of KFP removal are hence likely to affect lubrication, pressure distribution, load bearing, and consequently, increasing the wear and tear level within AT enthesis as an effect of lack of dynamic lubrication.

Table of Contents

Acknowledgement	ii
Summary	iii
Table of Contents	v
List of Abbreviations	ix
List of Figures	x
List of Tables	xv
1. Chapter 1: Introduction	1
2. Chapter 2: Kager’s Fat Pad (KFP)	7
2.1. Introduction	8
2.2. Anatomy of Kager’s Fat Pad	9
2.2.1. Location & Shape	9
2.2.2. Anchorage & Fibrosis	9
2.2.3. Sheaths & Retinaculae	10
2.2.4. Vascularity & Neural Supply	10
2.3. Biomechanics of Kager’s Fat Pad: Hypotheses	17
2.3.1. Lubrication	17
2.3.2. Pressure & Load Bearing Properties.	17
2.3.3. Protective Properties of Kager’s Fat Pad	18
2.3.4. Motion	18
2.4. Discussion	20
2.5. Conclusions	23
2.6. Next Chapter	23
3. Chapter 3: Quantifying the motion of Kager’s Fat Pad	24
3.1. Introduction	25
3.2. Materials & Methods	26
3.2.1. Surface Electromyogram (sEMG) Monitoring of FHL	26
3.2.1.1. Electrode Positioning	28
3.2.1.2. Skin Preparation	28
3.2.2. Dynamic Ultrasound (US) Testing of PW Sliding Distance.	30
3.2.3. Pilot Studies	33
3.2.3.1. Protocol Evaluation	33

3.2.3.2. Effects of Probe's Location & Angle Over PWSD .	34
3.2.4. Volunteer Selection & Preparation	38
3.2.5. Study Protocol	38
3.3. Results	39
3.3.1. sEMG Data	39
3.3.2. Dynamic US	40
3.4. Discussions	51
3.5. Conclusion	52
3.6. Next Chapter	52
4. Chapter 4: Effects of Ankle Load & Flexion Angle Effects on PW's Motion	53
4.1. Introduction	54
4.2. Materials & Methods	55
4.2.1. US Examination of PW Sliding Distances	55
4.2.2. Plantarflexion Loading Rig	55
4.2.3. Ankle Flexion Angle Measurement	56
4.2.3.1. US Examination of AT Insertion Angle	56
4.2.3.2. Goniometer Measurement of Angle Flexion Angle	56
4.2.4. Pilot Studies	62
4.2.4.1. Plantarflexion load Range	62
4.2.4.2. Protocol Evaluation	62
4.2.4.3. Ankle Flexion Speed	63
4.2.5. Volunteers Selection and Preparation	64
4.2.6. Study Protocol	64
4.2.7. Statistical Analysis	64
4.3. Results	65
4.3.1. Ankle Flexion Angle vs. AT Insertion Angle	65
4.3.2. Examining PWSD & PWD Variations Against Ankle Load	65
4.4. Discussions	76
4.5. Conclusion	78
4.6. Next Chapter	78
5. Chapter 5: Kager's Fat Pad's In-Vivo Load Bearing	79
5.1. Introduction	80
5.2. PW Hysteresis	81

5.2.1. Materials and Methods	84
5.2.1.1. Ultrasound Examination of PW Hysteresis	84
5.2.1.2. Pilot Study	84
5.2.1.2.1. AT Thickness Variation During Ankle Flexion	84
5.2.1.3. Ultrasound Examination Protocol	85
5.2.2. Volunteer Preparation & Selection	85
5.2.3. Statistical Analysis	85
5.2.4. Hysteresis Results	87
5.3. AT Bending	94
5.4. Assessing KFP Area, Shape & Volume Variations	97
5.4.1. Materials & Methods	97
5.4.1.1. MRI Examination	97
5.4.1.2. Pilot Study	98
5.4.1.2.1. MRI Study Protocol Evaluation	98
5.5. Results	101
5.5.1. MRI Examination	101
5.6. Discussion	109
5.7. Conclusion	111
5.8. Next Chapter	111
6. Chapter 6: Discussion	112
7. Chapter 7: Conclusions & Future Work	117
7.1. Conclusions	118
7.2. Future Work	121
7.2.1. Investigating Outside the ‘Control’ Group	121
7.2.2. Investigating the effects of lifestyle on PW’s motion	121
8. References	123
Appendix I	- Knee Meniscus	133
II	- sEMG System (Principles & Implementation)	139
III	- Background to Ultrasound Imaging	155
IV	- Background to MR Imaging	160
VI	- Paper Publication	168

List of Abbreviations

AFA	Ankle Flexion Angle
AT	Achilles tendon
ATIA	AT insertion angle
ATR	AT related pad of Kager's fat pad
ATRD	ATR's displacement
ATT	AT thickness
BMI	Body mass index
CST	Calcaneal superior tuberosity
CSTL	CST lining
CUBRIC	Cardiff University Brain Research and Imaging Centre
DAQ	Data acquisition card
DFP	Dorsiflexion position
DP	Deep pad of Kager's fat pad
FHL	Flexor Hallucis Longus
FOV	Field of view
fps	Frames per second
IMEMP	Institute of Medical Engineering and Medical Physics
KFP	Kager's fat pad
LED	Light emitting diodes
MRI	Magnetic resonance imaging
NFP	Neutral flexion position
PFP	Plantarflexion position
PSU	Power supply unit
PW	Protruding wedge of Kager's fat pad
PWD	Distance between PW's tip and most proximal point of AT insertion
PWSD	PW's sliding distance
PWT	PW's thickness
RB	Retrocalcaneal bursa
SD	Standard deviation
sEMG	surface Electromyogram
US	Ultrasound

List of Figures

- Figure 1.1:** A diagram illustrating the anatomical location of Kager's fat pad
- Figure 1.2:** Flow Chart of the PhD showing the tests carried out during this research
- Figure 2.1:** MRI scan in the Saggital plane of KFP
- Figure 2.2:** A histological section of AT enthesis in the saggital plane
- Figure 2.3:** A hemisection of the AT enthesis in the saggital plane illustrating the fibrous connections of KFP
- Figure 2.4:** Histological section of KFP in the saggital plane
- Figure 2.5:** Schematics illustrating the retinaculae surrounding KFP
- Figure 2.6:** Doppler ultrasound images of KFP in the saggital plane illustrating the increase in blood flow during Achilles tendonitis
- Figure 2.7:** Ultrasound imaging of a volunteer's hind foot in the saggital plane during ankle flexion illustrating motion of PW
-
- Figure 3.1:** The sEMG system implemented for this study
- Figure 3.2.:** A posterior view of the ankle showing electrodes position and location
- Figure 3.3:** The US system used for this research. Toshiba Aplio.
- Figure 3.4:** US images of KFP taken in the saggital plane with the probe placed on AT midline to measure PWSD

Figure 3.5: Comparing 2 PW sliding distance measurement methods, straight line and PW path measurement

Figure 3.6: A digital photo illustrating US probe's position and angle against AT

Figure 3.7: Illustrating influences of probe's location on AT and its angle over PWSD

Figure 3.8: sEMG data from this test

Figure 3.9: US images illustrating PW motion between plantarflexion and dorsiflexion during passive-, active-unloaded-, and loaded ankle flexions

Figure 3.10: PWSD during passive ankle flexion drawn against age

Figure 3.11: PWSD during unloaded active ankle flexion drawn against age

Figure 3.12: PWSD during loaded active ankle flexion drawn against age

Figure 3.13: PWSD during loaded active ankle flexion drawn against BMI

Figure 3.14: PWSD during loaded active ankle flexion drawn against body height

Figure 3.15: PWSD during loaded active ankle flexion drawn against body weight

Figure 3.16: PWSD during passive ankle flexion compared to PWSD during unloaded active ankle flexion

Figure 3.17: PWSD during unloaded ankle flexion compared to PWSD during loaded ankle flexion

Figure 4.1: Illustrates landmarks used to measure PWSD & PWD from sagittal ultrasound images

Figure 4.2: A photograph of the implemented loading rig. Main advantages over commercial rigs are the minimum offset load, unrestricted ankle flexion and allows US probe to be placed unrestricted

Figure 4.3: The electronics goniometer used for this study (25mm Blade Sensor, Gill Sensors Ltd)

Figure 4.4: A schematic illustrating how the goniometer rotates at the ratio of 2:1 during flexion

Figure 4.5: Illustrating the relationship between ATIA and AFA, when flexing against 100g and 5kg loads.

Figure 4.6: Relationship between PWSD and plantarflexion load (100g - 5kg)

Figure 4.7: Relationship between minimum PWD and load (100g - 5kg)

Figure 4.8: Relationship between ATIA and AFA at 100g load

Figure 4.9: Relationship between ATIA and AFA at 5kg load

Figure 4.10: Graphs comparing the relationship between PWD and ATIA in three volunteers with a 'dome' shaped CST

Figure 4.11: Relationship between PWD and ATIA 2 volunteers with a straight looking CST

Figure 4.12: A graph comparing the relation between PWD and ATIA, A PW hysteresis was found

Figure 4.13: A graph showing no hysteresis in one volunteer with a straight looking CST.

- Figure 5.1:** Typical hysteresis graphs drawing the distance between PW's tip and AT insertion point (PWD) against maximum range of AT insertions angle (ATIA). In certain flexion angle regions (circles), PW hysteresis was observed
- Figure 5.2:** AT thickness was measured in 3 different sites. Results showed AT thickness was uniform during ankle flexion
- Figure 5.3:** Graphs showing the relationship between ATIA and the distance between PW's tip and the most proximal point of AT in 3 different volunteers
- Figure 5.4:** Results graphs of 3 volunteers illustrating PW hysteresis. Hysteresis greater than error bars is consistent only in the plantarflexion region
- Figure 5.5:** Saggital US images taken showing the fibrous tip of PW
- Figure 5.6:** ATR displacement (ATRD) during ankle flexion was calculated by measuring the distance between the most distal point of ATR and the closest point of CST in a straight line
- Figure 5.7:** A graph illustrating the relationship between ATR displacement against AT insertion angle
- Figure 5.8:** Saggital US images measuring PW thickness
- Figure 5.9:** US images taken in the saggital plane showing AT kinks during ankle plantarflexion position
- Figure 5.10:** US images showing AT kinks reducing with increased AT load
- Figure 5.11:** Area and Volume measurement are carried out by highlighting the area of KFP in every slice, and using the Reconstruct® software to construct the 3D model, and hence the volume of KFP

Figure 5.12: A sagittal MRI image of a volunteer. comparing ankle neutral flexion to plantarflexion positions at AT midline, AT-CST angle changed on average from 19.2° to 30.4° , FHL-CST angle changed from 79.2° to 55° , and FHL-AT angle (or FHL-soleus angle) changed from 43.4° to 33.2°

Figure 5.13: A bar graph illustrating the changes in Kager's triangle's angles

Figure 5.14: Illustrates the change in KFP area between ankle plantarflexion and neutral positions

Figure 5.15: Bar graph illustrating the KFP volume in all 5 volunteers between ankle plantarflexion and neutral positions

Figure 5.16: A sagittal MRI image showing the number of transverse slices needed to show KFP. The 0.2T machine produces 10% uncertainty, where the 3T scanner has a maximum of 3.3% uncertainty when collecting transverse images. The 3T machine was also able to detect PW's tip in all volunteers

List of Tables

- Table 2.1:** A list of previous findings through literature review of Kager's Fat pad. This table also includes a number of main questions that are investigated within this PhD.
- Table 3.1:** Both methods of calculating PWSD were compared in volunteers with a non-straight shaped CST.
- Table 3.2:** Typical results of this pilot study. Repeatability testing was carried out on PWSD while ankle was flexed actively (no load). Pilot study was repeated at 90° knee angle, and on the second ankle (knee at 180° & 90°).
- Table 3.3:** A typical change in PWSD results illustrated. Results on the pilot study showed PWSD is consistent when the probe is placed within 40° of the perpendicular line against AT, and within 5 mm from AT midline.
- Table 4.1:** Testing the gear installed to increase the electronics goniometer's range
- Table 4.2:** Pilot study results showing differences in PWSD and PWD during 4s ankle flexion cycle, compared to 2s ankle flexion cycle
- Table 5.1:** Specifications of both MRI scanners available for this study
- Table 5.2:** Measurement uncertainty of both 0.2T and 3T MRI scanners for this study
- Table 5.3:** Comparing the changes in angles (highlighted in Figure 5.12) between ankle neutral and plantarflexion positions
- Table 5.4:** Results of KFP area changes using 0.2T MRI scanner
- Table 5.5:** KFP volume variation results from the 0.2T MRI scanner

Table 5.6: KFP Area and volume change results from the 3T MRI scanner

Table 5.7: 3T MRI scanner showing ATR area change between ankle plantarflexion and neutral position

Table 5.8: 3 T MRI scanner showing ATR area change between ankle plantarflexion and neutral position.

Table 7.1: List of the main findings of this PhD

Appendix II:

Principles of the electromyogram

Chapter 1

Introduction

Kager's Fat Pad (KFP), also known as the pre-Achilles fat pad, is an encapsulated adipose tissue occupying the space in Kager's triangle, whose boundaries are adjacent to three main anatomical structures, namely the Flexor Hallucis Longus (FHL) muscle and tendon anteriorly, the calcaneal superior tuberosity (CST) inferiorly, and the Achilles tendon (AT) posteriorly, as shown in Figure 1.1. KFP has three distinctive sections, namely the AT related (ATR), the deep pad (DP), and the protruding wedge (PW). The PW is connected to both AT and Calcaneus by fibrous connecting tissues [1] and can be observed sliding into retrocalcaneal bursal space during plantarflexion, and retracts during dorsiflexion [1-3], the location of which is a common site of overuse injuries in sport [1,4,5]. KFP is clinically considered as a radiological landmark [4,6] surrounded by a number of retinaculae tissues to stabilise their related tendons [7-9] and limit (or guide) its motion.

Fat pads can be found in a number of locations within the human body including ankles, knees, hips and elbows [5,8,10]. Benjamin et al, 2004 [5] carried out an extensive study to locate the different fat pads within or adjacent to entheses, and categorised them according to four features; **Endotenon**, which lies within the films of loose connective tissue separating adjacent fascicles in a tendon or ligament; **Epitenon**, which lies in the loose connective tissue on the surface of the tendon or ligament; **Meniscoid**, which is a feature of meniscal folds of synovium that project into subtendinous bursae; and **Insertional Angle fat**, which occupies the space between the tendon/ligament and the bone as the tendon/ligament approaches its enthesis obliquely. By definition, KFP is regarded an insertional angle and meniscoid fat pad.

In addition to being contained by a synovial membrane [1-3,10,11], KFP's motion led to speculating a number of biomechanical functions of KFP and indicated a higher importance to the AT enthesis organ than previously understood. Previously, the knee meniscus used to be subjected to removal for arthroscopic access in the knee, only to establish later the degenerative effects of meniscal removal on the knee joint [12-14]. Similarly, KFP currently can be subjected to removal for arthroscopic access as its biomechanical importance was not yet fully established and is clinically considered as no more than a fat tissue occupying the Kager's triangle's space. Previous studies suggested that KFP serves a number of biomechanical functions including load bearing [10,14], protecting the AT vascular supply [16-18], and assisting in lubricating the subtendinous region [1,15], and hence, helping prevent injury by reducing wear and tear within the AT enthesis organ [15]. This PhD research is focused on investigating the hypothesised in-vivo biomechanical functions of KFP within the AT enthesis organ.

Recent studies showed that the vascularisation of AT extends to KFP [16-18]. Although KFP was found rich in neural supply [1,5,15], no previous studies suggest KFP being a source of pain as opposed to sensing the pain or ankle's flexion angle. For instance, a reported case of myopericytoma showed that the individual suffered discomfort, but did not complain of pain [19]. Pain may be caused by bursitis or tendonitis [1-3,5,15] or as a result in the damage or distortion of KFP borders.

Although detailed studies on KFP are limited, it is only speculated that KFP has similar functions as other insertional fat pads such as Hoffa's and Infrapatellar fat pads within the knee joint [5]. A number of other functions were hypothesised for KFP including mainly dynamic lubrication [1,5], maintaining the bursal pressure at AT's enthesis [1-3,5,10,16,20], protecting AT vascular supply [1,16] and removing dead cell debris within AT enthesis caused by wear and tear [21]. Fat pads were also found to have healing and remodelling properties following graft harvest surgeries [22]. The deformation of the KFP during foot flexion has not been studied, which can help support or refute KFP's motion mechanism and its in-vivo biomechanical functions within the AT enthesis organ. Previous in-vitro studies showed KFP has lubrication, load bearing and pressure distribution properties [1,16], however no previous studies established in-vivo functionality of KFP.

This PhD aims at investigating the in-vivo functions of KFP as part of the AT enthesis organ in order to serve to better understand its functional biomechanics. Its physiological and biomechanical features need further studying in order to obtain a wider understanding that may serve to ensure quicker healing following an acute traumatic injury, better sports injury management, or lead to a better way of ankle joint management. This study utilized the testing methods carried out on joint biomechanics and established in vivo tests on KFP to evaluate its in-vivo biomechanical functions following the flow diagram below, Figure 1.2. The next chapter lists the anatomical details of KFP established and hypothesized by literature review

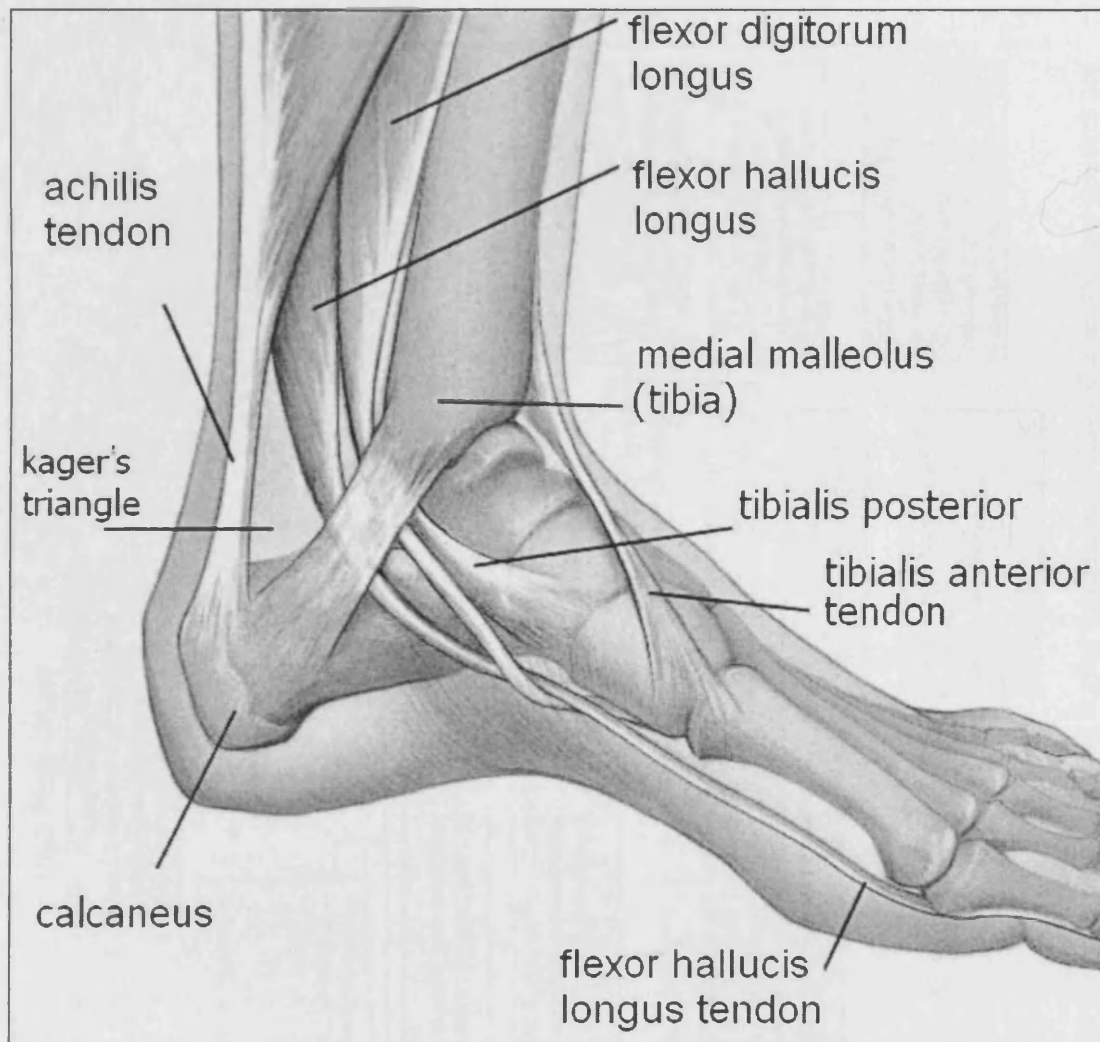


Figure 1.1: A diagram illustrating the anatomical location of Kager's fat pad (KFP), which is found in Kager's triangle. KFP's boundaries are adjacent to Flexor Hallucis Longus muscle and tendon anteriorly, the calcaneal superior tuberosity inferiorly, and the Achilles tendon posteriorly

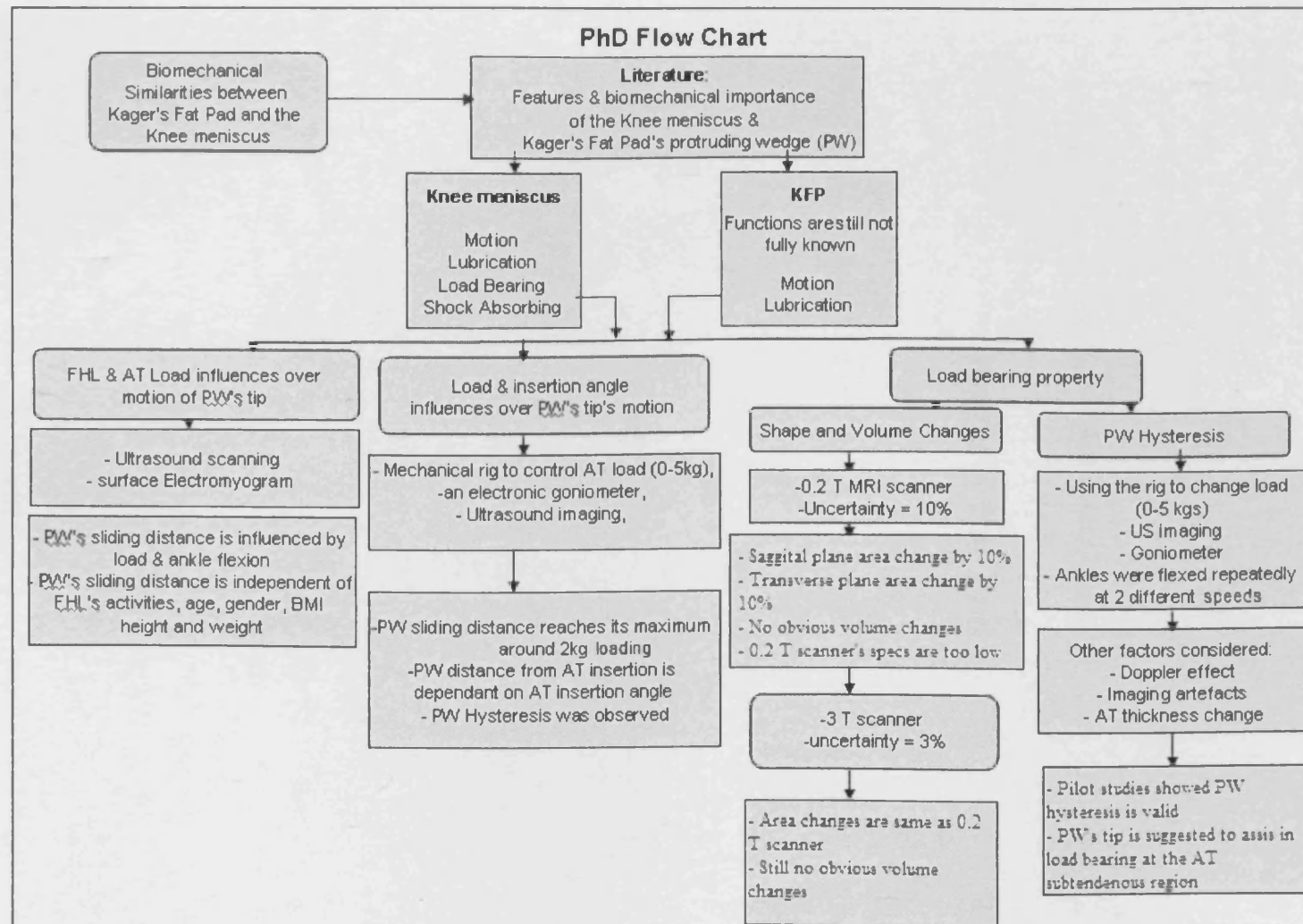


Figure 1.2: Flow Chart of the PhD showing the tests carried out during this research. Since the anatomical features are found similar between KFP and the knee meniscus (details in Chapter 2). This PhD is aimed at assessing the biomechanical functions of KFP using tests carried out previously to test the knee meniscus and KFP. PW = protruding wedge, FHL = Flexor hallucis longus muscle and tendon

Chapter 2

Kager's Fat Pad

2.1 Introduction

Kager's fat pad (KFP) is a mass of adipose tissue that is found within Kager's triangle space between the Achilles tendon (AT), Flexor Hallucis Longus muscle (FHL), and the calcaneal superior tuberosity (CST). Clinically, KFP can be used as a radiographic landmark [4] and was previously hypothesized to act as a variable space filler by moving into the retrocalcaneal bursa (RB) [2]. Although the consequences of KFP's removal are still unknown, it is subjected to resection for arthroscopic access [23]. Previous in-vitro studies suggested that KFP holds similar appearance and consistency to a fat tissue [16]. Current studies hypothesize important biomechanical functions that KFP may play within the AT enthesis organ [15,24]. KFP can be regarded as an insertional angle and meniscoid fat pad, as it occupies the space between AT and the Calcaneus, and in addition, has a feature of meniscal folds of synovium that project into RB [5,15,20]. KFP's anatomical features and hypothesised functions can be categorized as;

- Location & Shape
- Anchorage & Fibrosis
- Retinaculae & Sheaths
- Vascularity
- Motion

This chapter highlights the current understanding about KFP.

2.2 Anatomy of Kager's Fat Pad

2.2.1 Location & Shape

Reported sites where fat pads can be found in the human body include ankles, knees, hips, elbows and wrists [5,8,10,25]. Kager's fat pad is located in Kager's triangle space between the AT, FHL muscle and tendon, and CST, and in some cases, Kager's triangle space can extend to the soleus muscle (Figure 2.1) depending on the space of Kager's triangle. KFP as a result has a triangular shape in the sagittal plane. KFP consists of three distinctive sections, namely the AT related (ATR); which is adjacent to AT, the deep pad (DP); which is located between FHL and the CST, and the protruding wedge (PW); which seems to extend from the deep pad over the CST to the superior wall of RB.

2.2.2 Anchorage & Fibrosis

Previous histological studies [1,8,15] showed that KFP is contained in a synovial membrane lining, and a synovial invagination was present separating the ATR from PW (Figure 2.2). Fibrous Anchors were found attaching ATR posteriorly to the anterior wall of AT by fibrous strands [16]. DP and PW are attached to the calcaneus by the periosteum (Figure 2.3). Such fibrous links are speculated to stabilize KFP proximally and anteriorly [16]. A fibrous tip is typically found at the distal tip of PW [1,16] (Figure 2.4). It is suggested that PW's fibrous tip assists in distributing stress and load and shock absorbing within AT enthesis organ [14,16,28,29] since fibrosis is suggested to be caused by sustaining external compression [26,27].

2.2.3 Sheaths & Retinaculae

In addition to the synovial membranes containing KFP, the fibrous paratenon sheath (or “false tendon sheath”) contains ATR pad securing it to the AT. Anteriorly, the KFP appears to be separated from plantar muscle tendons (FHL, flexor digitorum longus and tibialis posterior) by retinaculae, which also assist in containing KFP within Kager’s triangle. These retinacula are superior extensor, superior and inferior peroneal retinacula (Figure 2.5), suggesting that KFP is surrounded by air tight sealing [8,9,30, 31]. Therefore, KFP was hypothesized to assist in reducing the pressure change within RB during ankle flexion [15,20].

2.2.4 Vascularity & Neural Supply

Histological studies have shown the presence of blood vessels within KFP that are part of the AT visualization network [16]. However, Doppler ultrasound shows no vascular activities in a healthy KFP. Recent investigations showed that during AT injuries such as tendonitis, blood flow was evident within ATR [16-18,21] (Figure 2.6). This suggests that KFP serves to protect the vascular supply for AT allowing higher level of vascularity. It is unclear whether the intensity of blood flow is area dependant or uniformly distributed however previous studies showed AT vasculature depends on age and exercise [32,33].

Neural supply was found evident within the fat pad [16-18,21]. This was suggested to provide KFP with sensory features, as the hindfoot is a common site to feel pain such as AT tendonitis [1].

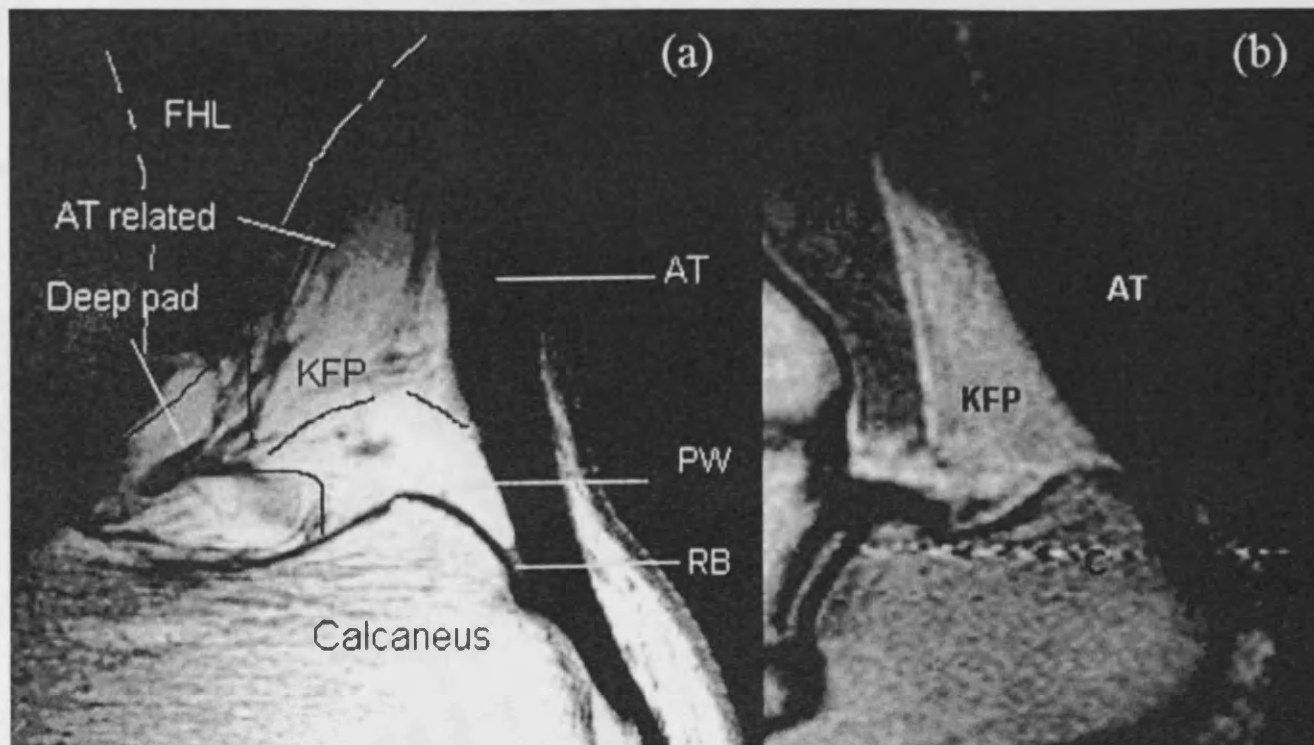


Figure 2.1. (a) KFP has 3 distinctive parts; the AT-related pad that is connected to AT, the deep pad which is closest to FHL, and the protruding wedge (PW) which is a wedge shaped pad, closest to AT insertion point. (b) In some cases KFP can be seen to extend to the soleus muscle (S).

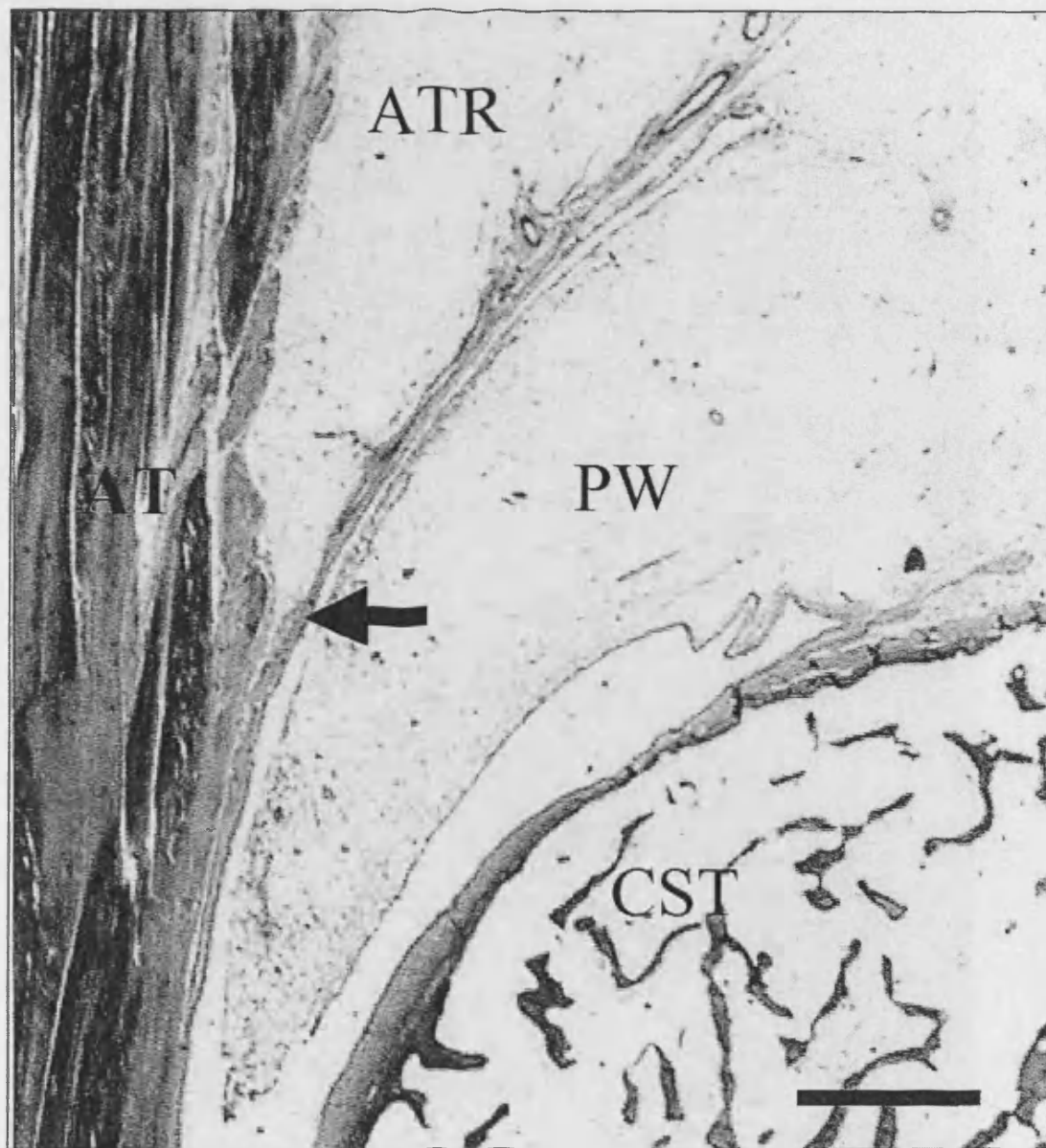


Figure 2.2: A histological section of AT enthesis in the sagittal plane. A fibrous anchorage is found between the Achilles tendon (AT) and AT related fat pad (ATR) (arrow). Scale bar = 1 mm [16]

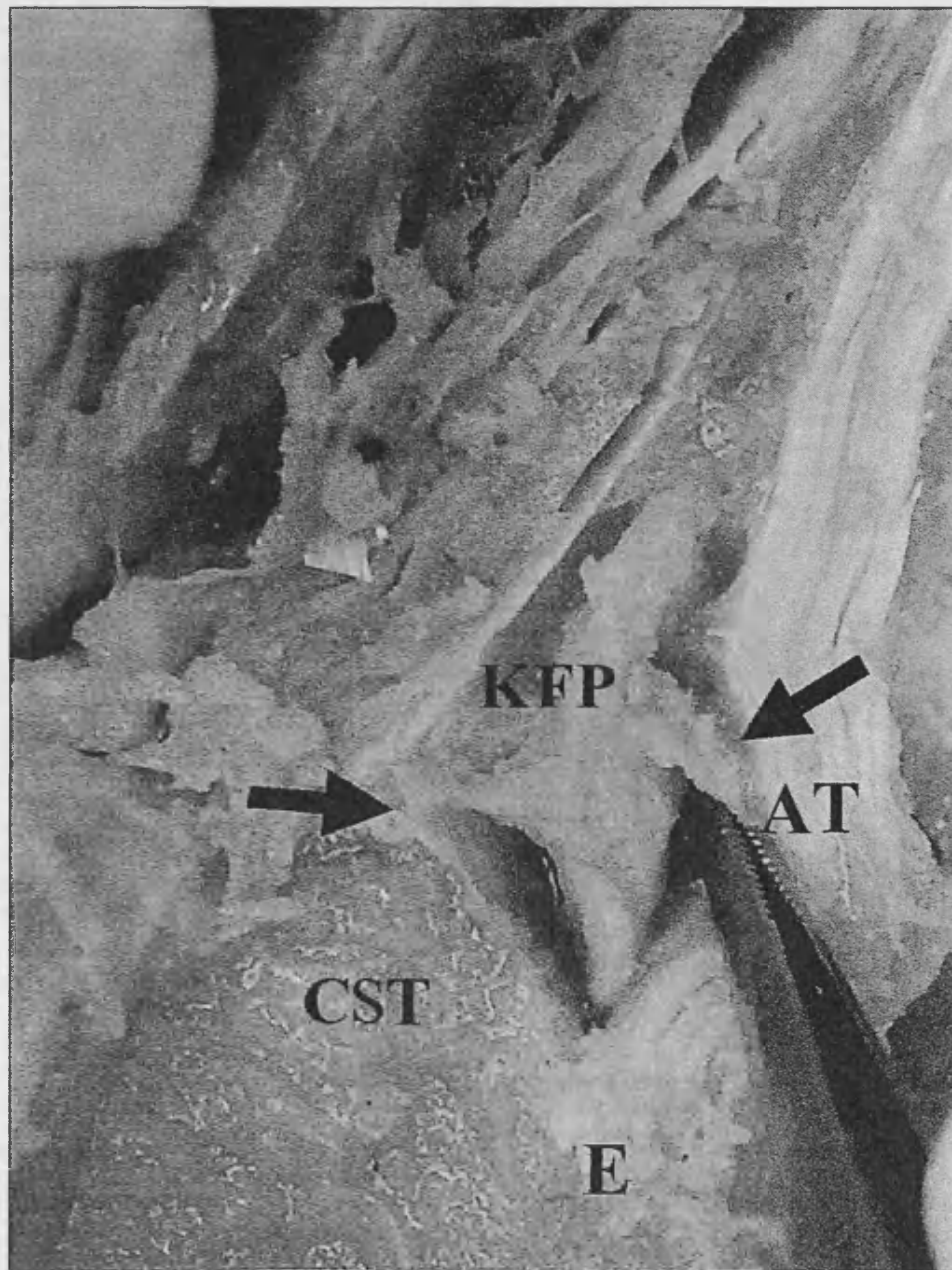


Figure 2.3: A hemisection of the AT enthesis in the sagittal plane illustrating the fibrous connections between KFP and Achilles tendon (AT) and Calcaneal superior tuberosity (CST), (arrows). These anchors secure KFP anteriorly and posteriorly to its location [16].
E = AT enthesis

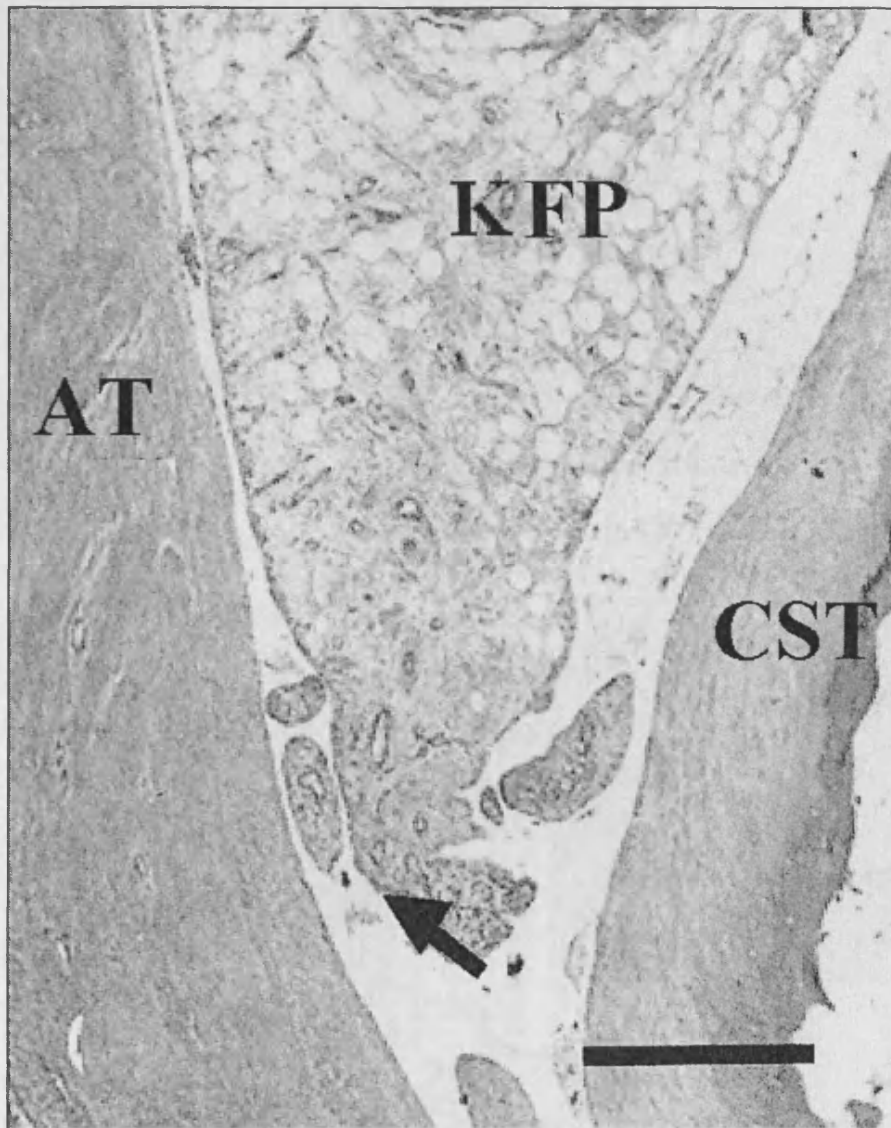


Figure 2.4: Histological section of KFP in the sagittal plane showing the fibrous tip of the protruding wedge (PW). Typically, fibrosis (arrow) is found at the sliding tip of PW. Scale bar = 300 μm [16]. AT = Achilles tendon, CST = Calcaneal superior tuberosity

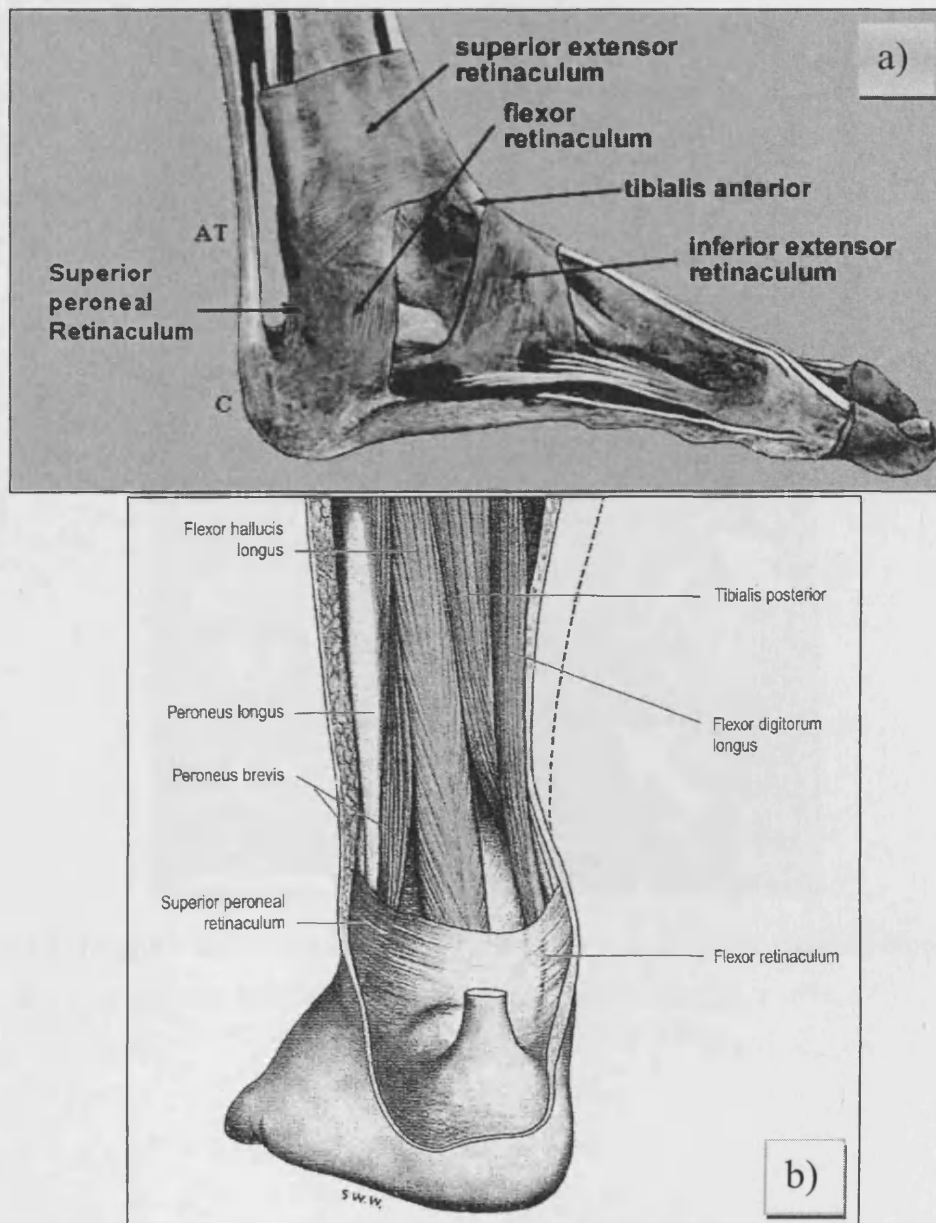


Figure 2.5: (a) A schematic of an adult's foot. In addition to the deep fascia, KFP is also surrounded by peroneal, superior extensor and flexor retinaculae. These also assist in sealing KFP in air tight containment. AT = Achilles tendon, C = Calcaneus bone. **(b)** A diagram of a typical hind foot of an 8 year old child. Flexor and superior peroneal retinaculae are illustrated between KFP and posterior wall of FHL and deep plantarflexion muscles [30,34].

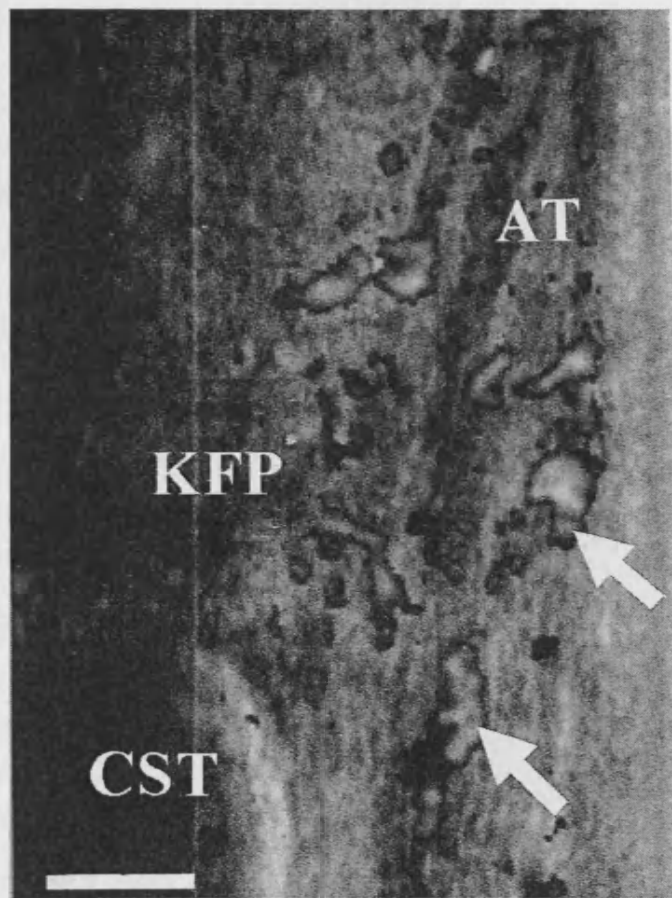


Figure 2.6: Doppler ultrasound images of KFP in the sagittal plane showing blood flow during a case of Achilles tendonitis (arrows). Scale bar = 4 mm [16]

2.3 Biomechanics of Kager's Fat Pad: Hypotheses

Although direct studies about KFP are limited, a number of studies have hypothesised, indicated, or discussed the possible biomechanical importance of KFP within AT entheses organ. PW's motion is speculated to provide a number of biomechanical advantages to AT, the CST and RB including lubrication, load bearing, stress distribution and immuno-protective functions.

2.3.1 Lubrication

Theobald et al, 2006 [1] showed that KFP is contained within a synovial membrane and synovial fluid presence was evident in RB [2,3,20]. The contact area between PW and AT and calcaneal superior tuberosity, or AT entheses, is suggested to be lubricated by PW as it protrudes into and retracts from the bursal space during ankle motion. In-vitro testing of bovine KFP found synovial fluid being excreted when the fat pad is pressed [16]. This suggested that pure fluid film lubrication provides a hydrodynamic lubrication at KFP-bone interface [1,15].

2.3.2 Pressure & Load Bearing Properties

Although previous ultrasound in-vivo studies of KFP suggested PW does not increase the 'pulley' area of AT during ankle flexion [1,15], suggesting that KFP may not serve as a load bearer, in-vitro testing on bovine fat pads suggested KFP can reduce load against the calcaneal superior tuberosity of up to 39% as the contact area increases [16]. A number of in-vivo studies speculate pressure properties of KFP by reducing pressure change within RB during ankle flexion [2,3,20], and suggest PW's fibrous tip may serve as a shock absorber [26-29]. In-vitro testing of KFP showed a pressure reduction of up to 30% as the ankle flexion angle increased to the maximum dorsiflexion position [16].

2.3.3 Protective Properties of Kager's Fat Pad

Literature review showed that PW can also act to clear its contact areas with AT and calcaneal superior tuberosity from any dead cells caused by wear and tear [21]. As the tip of PW retracts away from AT insertion point during dorsiflexion, it removes debris from the subtendinous region. KFP was also speculated to protect AT's vascular network by containing part of AT's vascular network [5,7,15-18]. As fat pads can be considered as cell regeneration sources [35], it can be speculated that KFP performs cell replacement for dead cells within AT entheses.

2.3.4 Motion

KFP can be observed to move during ankle flexion [1-3,36] within the RB space. PW slides into the bursal space as the ankle is flexed from dorsiflexion to plantarflexion positions. PW slides in the opposite direction as the ankle is flexed in the opposite direction (Figure 2.7). PW motion appears to be the main factor that allows KFP to have the speculated mechanical advantages within AT entheses, although the motion's characteristics are unclear. Three possible PW movement mechanisms have previously been hypothesized [1]: (1) as a consequence of the superior displacement of the calcaneus; (2) the PW is pulled into the bursa caused by pressure change within RB; and (3) FHL muscle contractions act to move the fat pad. Since the anchorage was evidently found between KFP and CST, CST was observed to pull PW's distal wall in the opposite direction of PW's tip motion, and hence invalidating the first theory as a mechanism for PW motion.

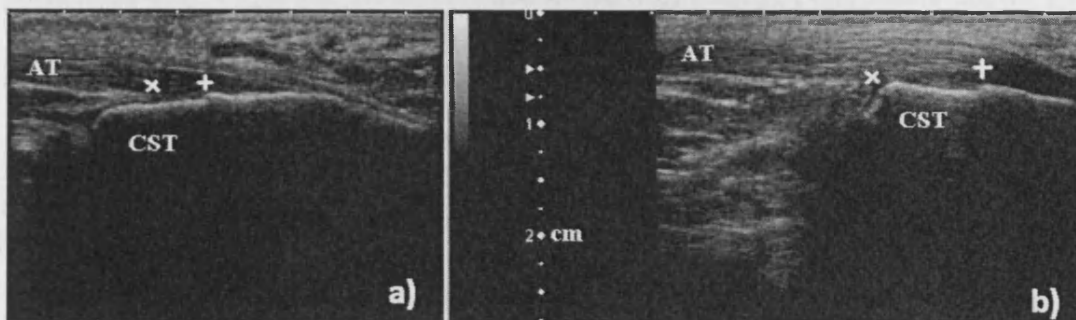


Figure 2.7: Ultrasound imaging of a volunteer's hind foot in the sagittal plane during ankle flexion, while volunteer was in the prone position on a testing bed. As the ankle flexes from (a) plantarflexion, to (b) dorsiflexion the tip of PW (X) slides away from AT insertion point (+). Scale bar provided by US images is in the middle.

2.4 Discussion

KFP is an adipose tissue located in Kager's triangle between AT, FHL and CST. KFP is encapsulated by a synovial membrane and consists of adipose cells, which allows PW high mobility within AT enthesis. KFP is divided to 3 pads; AT-related, deep pad, and PW. KFP is attached to AT and CST by fibrous anchorage, sheaths, and retinaculae, and forms the anterior superior wall of RB. Previous Doppler US examinations demonstrated vascular supply within KFP during AT tendonitis, proving blood vessels found inside KFP are connected to the AT blood supply network, and hence demonstrating blood flow within KFP. Neural network was also evident within KFP suggesting sensory functions for KFP.

KFP is still widely considered to serve predominantly as a variable space filler, with hypothesised secondary functions providing a mechanical advantage to the Achilles tendon enthesis organ by moving into and out of RB during ankle flexion. This motion was debated to also cause KFP to serve as a load bearer but US examination [16] showed no obvious signs suggesting in-vivo load bearing by comparing images taken from the 3 ankle flexion positions (plantarflexion, neutral and dorsiflexion). No real time studies were found on KFP's load bearing. It is still not fully established how KFP behaves in-vivo in real time, however, animal testing showed that cadaver KFP, when removed, behaves as a fat tissue [16]. PW's motion is also suggested to minimize pressure changes within RB space during ankle flexion, to have an immuno-protective role within RB - removing dead cell debris produced by wear and tear of its lining tissues and to provide subtendinous lubrication promoting low wear, suggesting KFP may provide tendon protection and injury prevention [15].

The consequences of KFP removal in humans is not known, however, animal studies showed that fat pad removal can alter the growth of the related tendon by up to 25% in rabbits [37]. Although removing KFP may provide better arthroscopic access to the hindfoot region and symptomatically relieve pain, animal testing showed it encourages growth of scar tissue causing pains and limiting the dorsiflexion range [37,38,45]. Literature review also suggests fat pad removal can influence the biomechanics of the

joint in question [38]. Although studies showed neural supply within KFP, it is not clear where the pain feeling originated from. Harish et al [39] reported a case of myopericytoma in KFP, however, the subject did not complain of pain. Furthermore, fat pads in general were shown to have healing properties [22]. No studies were found that quantified fat pads healing, or to establish if the healing is caused by internal factors (cell regeneration) or external influences (blood supply).

Features	Kager's Fat Pad
Shape	Triangular in the saggital plane Shape changes between 'L' and 'J' during flexion Do area & volume change during ankle plantar- & dorsi-flexion?
Location	Occupying Kager's triangle between AT, FHL and CST
Anchorage	Fibrous connections linking the KFP to AT and superior calcaneal tuberosity. Fascial sheath and peroneal retinaculum surround the KFP causing an air tight seal
Fibrosis	PW usually has a fibrous tip Are fibrous tips visible in-vivo?
Vascularity	Small blood vessels pass through AT adjacent section of KFP branching from the posterior tibial and peroneal arteries
Movement	Protrudes into the retrocalcaneal bursa during plantarflexion and retracts during dorsiflexion What are the factors for PW's motion?
Load bearing	In-vitro testing suggested KFP minimizes load upon AT enthesis by 40% Can PW bear load in-vivo?
Healing	Fat pads in general were suggested to heal after a number of injuries. No regeneration after partial removal
Consequences of removal	Shortening of AT during growth phase. Speculated to cause lack of protection of AT blood supply, lubrication and load or stress distribution, increasing wear and tear

Table 2.1: A list of previous findings through literature review of Kager's Fat pad. This table also includes a number of main questions that are investigated within this PhD.

2.5 Conclusions

As the motion of PW is found to be the common factor between most hypothesized functions, this PhD focuses on examining the characteristics of PW's motion. Published studies that focused on KFP and PW were scarce. In addition, since KFP was found to hypothetically perform a number of important biomechanical roles within AT enthesis organ, this PhD's experiments were based on methods and measurement techniques that were evaluated to measure either KFP or other insertional fat pads, in order to help prove or refute KFP's hypothesized biomechanical functions. Three main experiments were carried out to;

- Determine the PW's sliding distance (PWSD) during ankle flexion in a healthy, or 'control' group, and investigating any obvious influences of FHL activities on PWSD.
- Evaluate the influences of ankle loads, and ankle flexion angle on PWSD and PW's distance from the most proximal point of AT insertion (PWD).
- Study the possibility of PW's load bearing function by measuring the changes of KFP area and volume changes.

2.6 Next Chapter

Chapter 3 details the first test that was carried out in this PhD. Aimed at assessing the hypothesized influences of PW's motion, the test used a dynamic ultrasound imaging and a surface electromyogram (sEMG) to study the influences of FHL's contractions and ankle load on the motion of PW's tip.

Chapter 3

Quantifying the Motion of Kager's Fat Pad

2.7 Introduction

As KFP is contained within a synovial membrane and consists of adipose cells, this was shown to allow PW high mobility within AT enthesis [15]. PW's motion is speculated to serve a number of biomechanical advantages to AT enthesis including minimizing pressure changes within the retrocalcaneal bursa during ankle flexion [20] and removing dead cells from within RB produced by wear and tear of its lining tissues [21]. In addition, this motion is restricted due to the fibrous anchorage and retinaculae surrounding the AT enthesis region, allowing PW to slide into the retrocalcaneal bursal space and out during plantarflexion and dorsiflexion, respectively, in a sealed environment.

Although no previous studies have quantified or explained PW's motion yet, three possible PW movement mechanisms have been hypothesized [1,16]:

- (1) As a consequence of the displacement of the calcaneus,
 - (2) The PW is pulled into the bursa caused by pressure change within the bursal space during ankle flexion,
- And,
- (3) FHL muscle contractions act to move the fat pad.

This study aims to measure the normal range of motion of PW by measuring its sliding distance (PWSD) during ankle flexion in healthy volunteers, and to establish obvious influences of FHL and ankle load over PWSD, to examine KFP hypothesised mechanisms of PW's motion and its biomechanical functions within the AT enthesis organ.

2.8 Materials & Methods

A number of techniques were used to measure the PWSD and any obvious influences that FHL and ankle load have on PWSD. A surface Electromyogram (sEMG) was placed on the FHL muscle belly, while using dynamic ultrasound imaging to scan and measure the sliding distance of PW.

2.8.1 Surface Electromyogram (sEMG) Monitoring of FHL

To monitor the FHL activity during ankle flexion, a single channel sEMG system was required. The surface electrodes provide a non invasive approach to measuring the muscle activity and ensure volunteer comfort. In addition, using invasive electrodes (needle electrodes) can affect the results directly by interacting with the moving tissues in the AT enthesis region, which can restrict the muscle's motion, and hence, the results.

Within this research, a computer was provided, as well as a 16-channel data acquisition (DAQ) device (Datalink DT9800) from a previous project at the Institute of Medical Engineering and Medical Physics (IMEMP), where this research was carried out. Commercially available sEMG devices have prices varying between £350 and £10k depending on the specifications and options included in the purchase. Systems that allow data acquisition for offline processing started from £3k. Note that this represents the average prices of the commercially available options.

It was most cost effective and efficient to design and build a sEMG pre-amplifier circuit to be connected to the already available DT9800 DAQ card. The implemented system consisted of a sEMG pre-amplifier circuit, a PC provided for the PhD research, a LabVIEW package which was installed using the School of Engineering's license, the DT9800 multi-channel DAQ board, and 3 surface electrodes for each test (2 potential difference electrodes and one reference electrode) (Figure 3.1). Implemented sEMG system's design, calibration and testing are detailed in Appendix II.

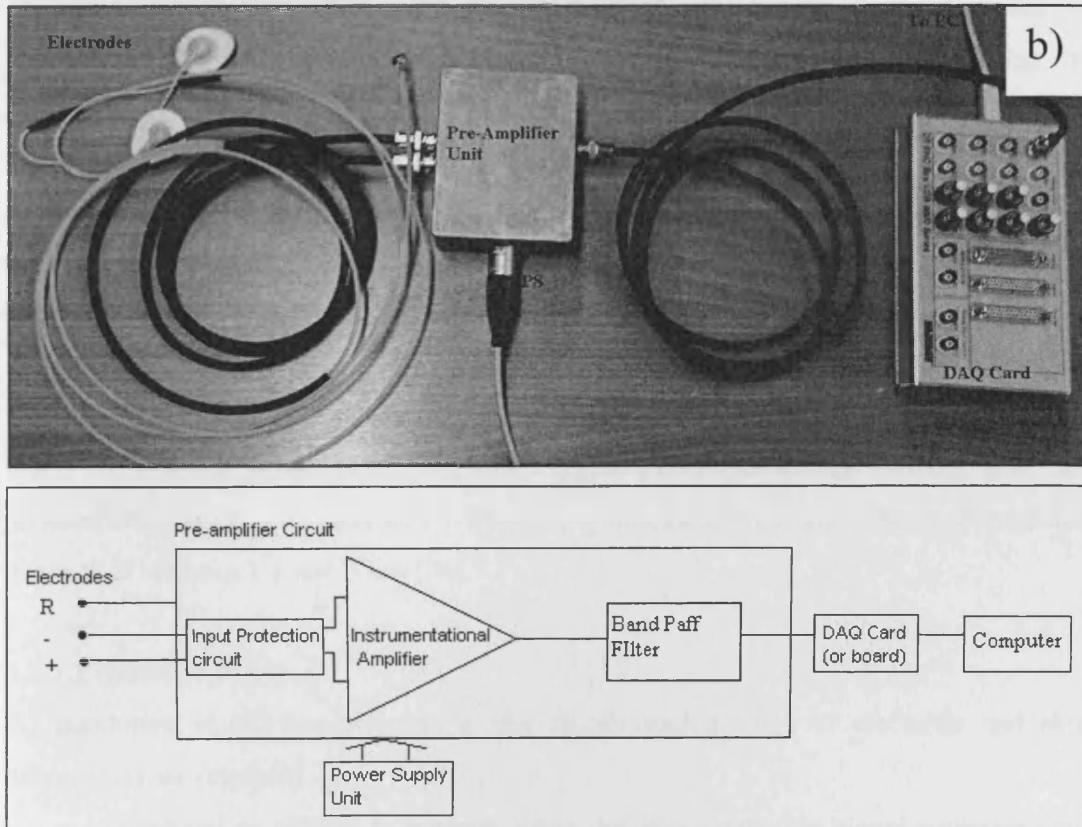


Figure 3.1: The sEMG system implemented for this study consisted of (a) surface electrodes, pre-amplifier unit to increase the EMG signals from less than 1mV to around 10V (gain of 10,000), a DAQ card to transfer EMG signals from the preamplifier to the PC, which has a LabVIEW software code to process, save and view the EMG results. (b) The preamplifier unit consisted of an input protection circuit to save both the volunteer and the preamplifier from static electricity, an instrumentational amplifier to measure and amplify the potential difference between the two electrodes and a band pass filter to allow only EMG signals (between 100 and 500 Hz) to pass without attenuation. Details in Appendix I. PSU = power supply unit.

3.2.1.1 Electrode Positioning

The main limitations of sEMG electrodes are the depth of the muscle to examine and the area where the muscle in question is closest to the skin (skin-muscle area). Placing the electrodes in the right position is therefore essential. Figure 3.2 highlights the most convenient point for the sEMG electrodes to be placed [74], laterally, about 10 cm superiorly from the heel (Figure 3.2). As electrical signals travel along the muscle fibres, both electrodes should be positioned along the fibre lines. Areas of tattoos and scar tissues should be avoided for a better skin conductivity.

The separation distance between the bipolar electrodes increases the signal's amplitude when the distance is increased, but this reduces impedance match between skin and preamplifier circuit and increases possible physiological crosstalk. The recommended distance is between 1.5 and 2 cm [74].

3.2.1.2 Skin Preparation

To maximize signal conductivity, a few recommended steps of electrode and skin preparation are required:

- Using gel or alcohol to remove, when possible, subtle but signal contaminating factors on the skin like hair, dead skin, make-up, and creams and oils
- Apply adhesive and conductive gel, pre-gelled electrodes are recommended
- Small electrodes are preferred, to increase localization of measurement. The smaller the electrode the higher the impedance values, improving skin-circuit conductivity [75]
- Manually locating muscle belly region during muscle contractions for the correct electrode position

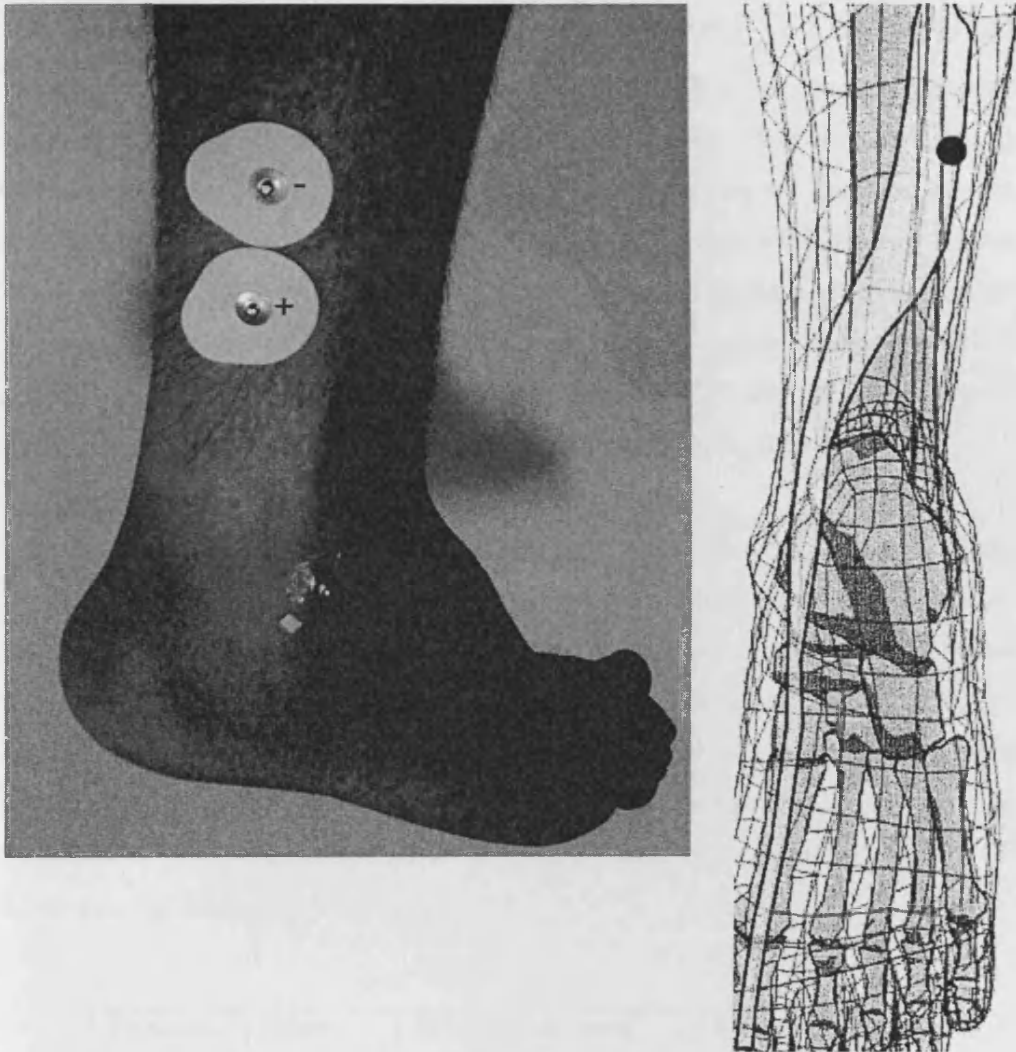


Figure 3.2: Right) A posterior view of the ankle showing electrodes locations on FHL (+ & -) and a reference electrode on a joint bone (R). **Left)** A schematic of the ankle highlighting with the black dot the electrode's position to pick up neural signal of FHL belly. About 10-15cm superiorly from the heel's most proximal point [74]

2.8.2 Dynamic Ultrasound (US) Testing of PW Sliding Distance

A dynamic ultrasound (US) scanner (Toshiba Aplio - with a linear transducer operating at 12 MHz, Figure 3.3) was used to measure PWSD during ankle flexion in the sagittal plane. Dynamic US imaging was previously used to accurately measure abnormalities and motion distances on KFP [1,16], and other soft tissues [40,41]. Still images were extracted from video scans using VirtualDub© software package (MPEG2 1.6.15). The two images showing the maximum ankle plantarflexion and dorsiflexion positions were used to measure PWSD. Prominent features within the CST and AT insertion point were used as anatomical landmarks to measure PWSD consistently (Figure 3.4).

Two methods were considered to measure PWSD; by measuring PW actual motion line, or measuring the straight line between two landmarks representing PW's motion limits (as used in a previous study [1]). A pilot study was carried out to compare both methods (Figure 3.5). The difference between both methods was on average 11% (standard deviation = 2%) depending on the shape of CST (Table 3.1). T-test showed results are significantly different between both methods. Measuring the actual path distance, therefore, is adopted to measure PWSD since it measures the line that PW's tip slides on while moving during ankle flexion.

Volunteer number	Straight line (mm)	PW sliding path (mm)
1	10	11
2	7	8
3	9.5	10.5
4	13	14.5
5	6	6.5

Table 3.1: Both methods of calculating PWSD were compared in 5 volunteers with a non-straight shaped CST. Results from PW sliding path consistently showed higher results than straight line measurement, on average, 11%. T-test showed a significant difference between the two methods.

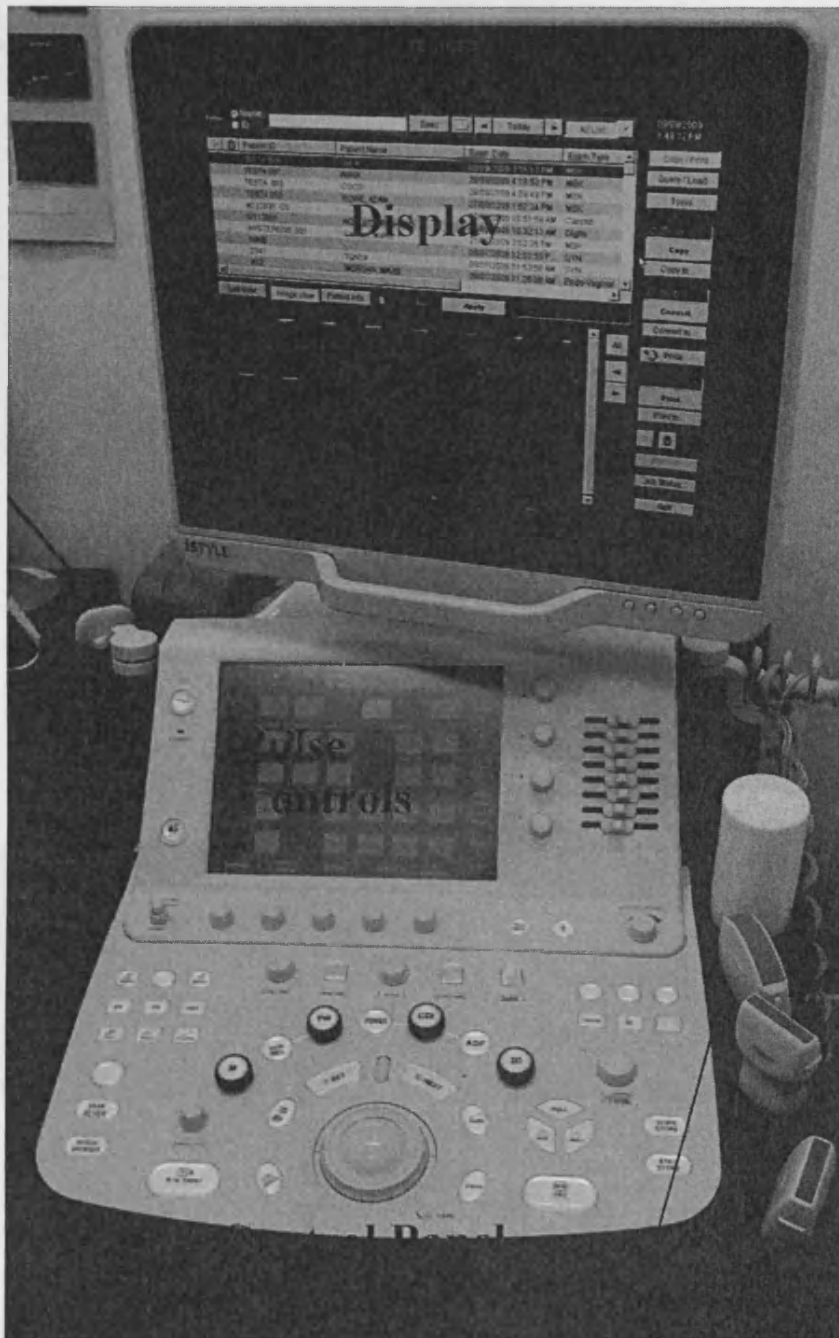


Figure 3.3: The US system used for this research. Toshiba Aplio. The transducer used produces linear US waves at 12 MHz. US image video files were stored in the hard disk and transferred for the PC for offline measurements.

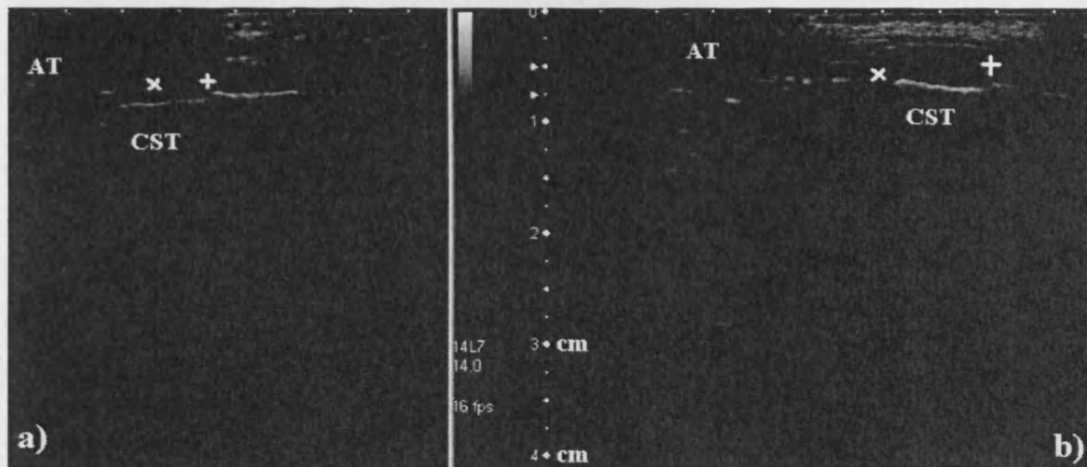


Figure 3.4: US images of KFP taken in the sagittal plane with the probe placed on AT midline. To measure PWSD, AT most proximal insertion point (+) and the tip of PW (x) were used as landmarks. The change in PW location between ankle plantarflexion (a) and dorsiflexion (b) with respect to AT insertion point reflects PWSD. Scale bar in the centre (cm)

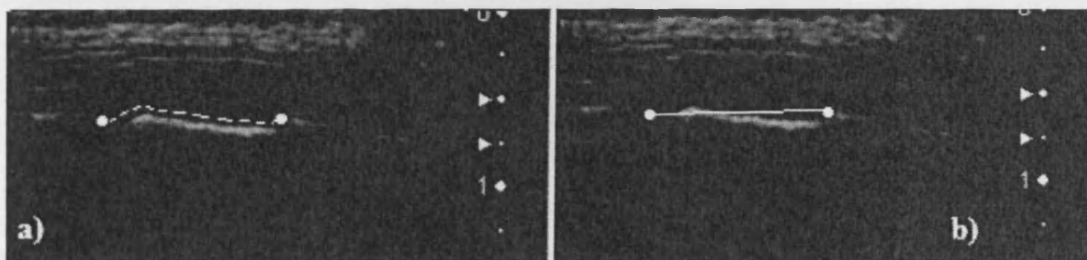


Figure 3.5: Magnified (x2) US images of Figure 3.4, comparing PW path measurement (left) = 11 mm to straight line measurement (right) = 10 mm. Scale is on the right hand side of each image (cm)

2.8.3 Pilot Studies

2.8.3.1 Protocol Evaluation

A pilot study was performed to test the overall performance and consistency of the method as well as evaluating the protocol by repeating it on 5 volunteers (section 3.2.5) five times. The protocol produced US images that confirmed fat pad's motion in all volunteers. The sEMG system successfully detected FHL activities in all volunteers. Table 3.2 for typical results of one of the volunteers for this pilot study shows PWSD had a coefficient of variance < 0.125 , with a maximum variance of 0.5mm in distance measurements¹. These findings were consistent with all volunteers, making this method a consistent method to measuring PWSD and FHL activities.

The pilot study was extended to test contralateral differences of PWSD by repeating the protocol for both ankles and any obvious effects of knee angle by repeating the protocol while the knee was at a different flexion angle (90° and 180°). Results showed no contralateral differences in PWSD (variation coefficient < 0.125). No changes were found in PWSD when knee flexion angle was changed (variation coefficient < 0.125). Therefore, the protocol was carried out on one ankle and at one knee flexion angle.

	1 st scan	2 nd scan	3 rd scan	4 th scan	5 th scan
Unloaded Flexion (mm)	10	10.5	10	10	9.5
Knee at 90° (mm)	10.5	10	9.5	10	10.5
2 nd Ankle (mm)	9.5	9.5	10	10.5	10.5

Table 3.2: Typical results of this pilot study. The ankle was scanned 5 times to measure the PWSD of the same volunteer while ankle was flexed actively against no load when knee is at 180° , the scans were repeated at 90° knee angle and on the second ankle (knee at 180°).

¹ The limit of accuracy to measuring distances from the US system is 0.4mm, as mentioned in the system testing & calibration report.

3.2.3.2 Effects of Probe's Location & Angle Over PWSD

Previous studies indicated that the wall shape of the retrocalcaneal part of the calcaneus is asymmetrical [44], which means PW's tip can slide on an uneven surface. Although scans were taken on the AT midline, by drawing a line for repetitiveness, this pilot study was carried out to study the possible effects of changing the probe's location and/or angle, with respect to AT's midline using a manual goniometer to measure angles of the probe against AT from images taken by a digital camera (Figure 3.6). The probe was moved along the AT in the sagittal plane in steps of 5 mm. To test the probe's angle effect on the sliding distance results, the US probe was placed at a perpendicular angle against AT, the angle was changed at increments of 20°.

It was found that as long as the US probe was located near the AT midline (± 5 mm from AT width) and was aligned with the long axis of the foot ($\pm 40^\circ$), PWSD still has the same variation coefficient < 0.125 (Figure 3.7). This pilot study was carried out on only 5 volunteers, therefore, a line was drawn on volunteers' AT midline using a body marker to eliminate possibilities of the test extended to examine if the force applied by placing the probe of AT's midline would influence the reading. The volunteers were scanned 5 times with the force applied increasing from softly placing the probe on the skin surface to just enough force to be noticeable with slight volunteer discomfort. The results were consistent results of PWSD and PWD except when the force applied caused slight discomfort as it started causing the location of PW's tip to change. This means the results are consistent until the force applied by placing the probe is noticeable by the volunteer. As CST can differ in shape across different slices on the sagittal plane [16], which means changing the location during testing can affect PWSD results. Therefore, a skin marker was used to draw a line over AT midline in order to acquire all images from the same line for each volunteer. Human reading error was kept to minimum as data was collected by the same researcher.

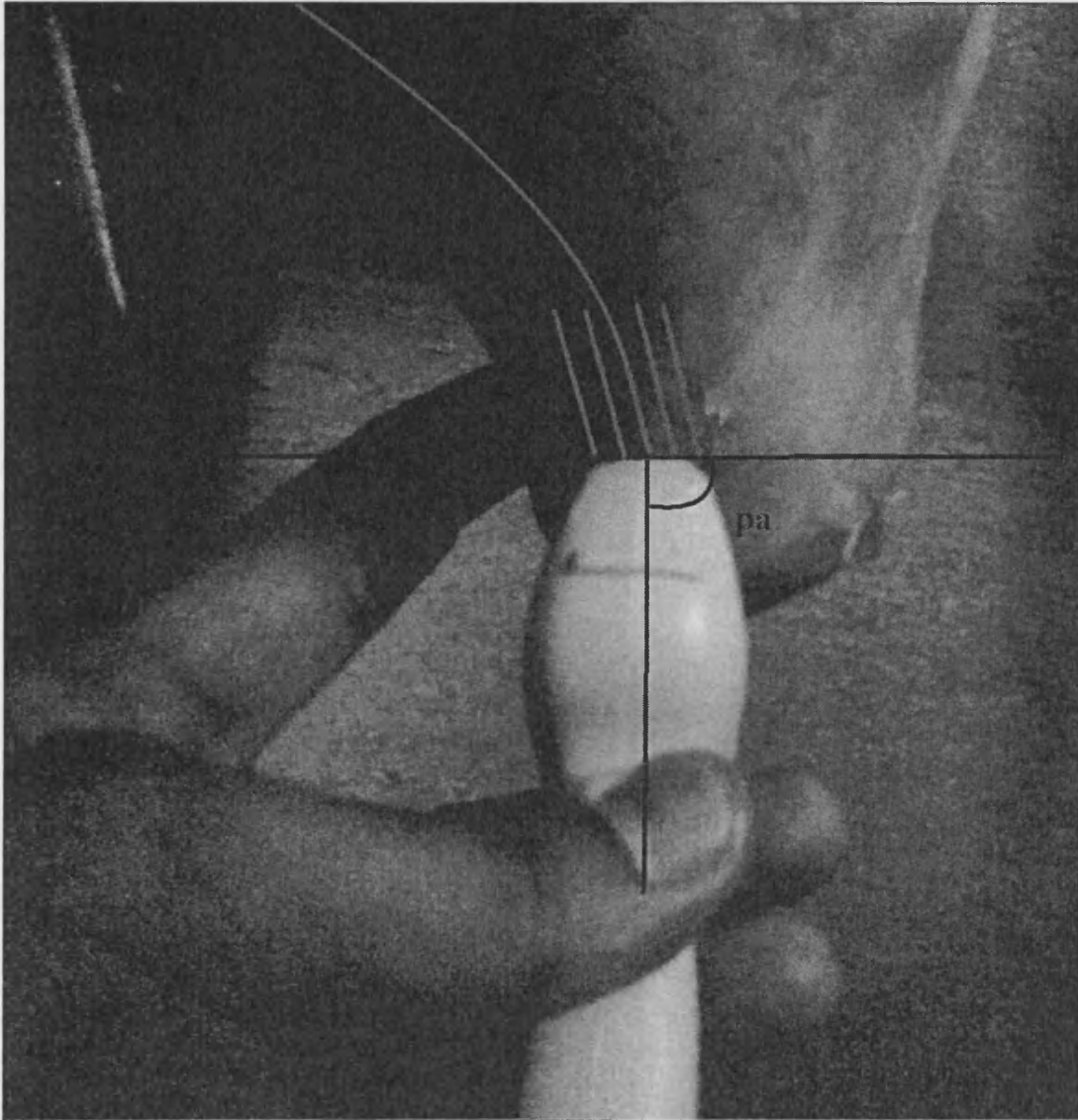


Figure 3.6: A digital photo illustrating US probe's position and angle against AT. To scan KFP, US probe is placed on AT midline along the axis of the foot. A pilot study tested the effects of probe's angle (pa) and changing probe's location from AT midline (ATM). Probe's angle is measured with respect to the coronal plane.

Probe's Angle (°)	Average PWSD (mm)	Probe's Distance from AT midline (mm)	Average PWSD (mm)
30	5	*	*
50	12	+10	8
70	12.5	+5	12.5
90	13	Midline (0)	12.5
110	12.5	-5	13
130	12.5	-10	9.5
150	6	*	*

Table 3.3: A typical change in PWSD results illustrated. Results on the pilot study showed PWSD is consistent when the probe is placed within 40° of the perpendicular line against AT (as shown in figure 3.6), and within 5 mm from AT midline. Probe's angles were rounded to the nearest 5° and a skin marker was used to draw 5 mm lines across AT. * = no readings were obtained as the images were unclear to read.

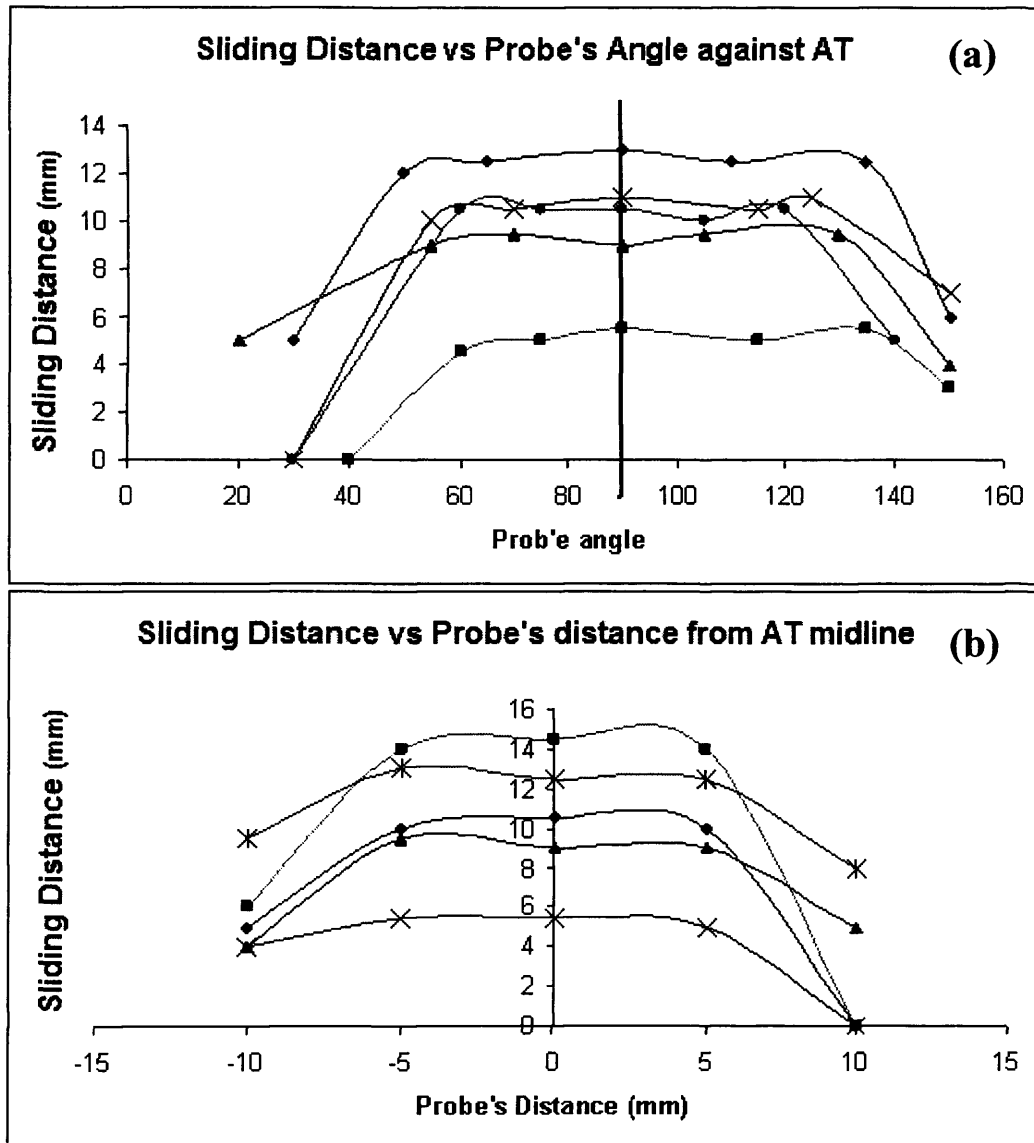


Figure 3.7: (a) Results from testing effect of changing probe's angle against AT (90° being perpendicular as in Figure 3.6) in 5 volunteers (5 lines), showed consistent PWSD (variation coefficient < 0.125) within 30° from the foot axis line 90° . (b) Results from testing effect of probe's location with respect to AT midline, showed consistent PWSD measurements within 5 mm from the AT midline

2.8.4 Volunteer Selection & Preparation

Volunteers invited had to be healthy and have gone through no major surgeries or injuries in the ankle or knee. Raosoft Inc. software was used to calculate the required sample size [42]. With expected confidence level increased to 95% the required sample size is 21.

Since this study requires using NHS equipment, in collaboration with Cardiff & Vale Hospital NHS Trust, ethical approval was obtained from the NHS ethical committee at the Cardiff & Vale Hospital. (Volunteer information sheet is attached in Appendix III)

2.8.5 Study Protocol

The hindfoot of 25 healthy volunteers (8 females & 17 males, age 20-57, BMI 19-29) was scanned using US imaging. FHL activity was monitored using sEMG. The test was devised into four parts to establish FHL's influence over PWSD, and detect any obvious influences of ankle loading on PWSD.

1. FHL only (without ankle flexion). Subjects stood up on a double foot stance on a step with the big toe suspended over the step. Subjects flexed their big toe repeatedly through its full range of flexion
2. Passive ankle flexion. Subjects laid prone on the examination bed allowing unrestricted ankle flexion. An assistant placed an open palm on the subject's dorsum to fully flex & extend the subject's ankle repeatedly, through the full range.
3. Active ankle flexion – Unloaded. Subjects laid prone, with their knees fully extended. Subjects actively flexed & extended their ankle through its full range.
4. Loaded ankle flexion – Loaded. Subjects stood in a single foot stance on a step. Subjects fully flexed & extended their ankle, against their body weight. A grip was available for balance support.

2.9 Results

2.9.1 sEMG Data

Although sEMG data had different values from one individual to another, intra-volunteer data had consistent characteristics between the different parts of the protocol. For each part of the protocol sEMG data had the following general appearance (Figure 3.8)

1. FHL only. During big toe flexing only, sEMG signals were evident in all volunteers, proving the presence of FHL muscle activities during 'FHL only'.
2. Passive Ankle Flexion. No obvious sEMG signals were detected in any of the 25 volunteers. During pilot study, a number of volunteers showed minimal EMG activities. Previously the assistant held the volunteer's ankle with hands gripped around the foot and calf in no specific manner. This resulted in some volunteers experiencing involuntary muscle contractions caused by the pressure applied on the ankle while manually flexing it. Once the flexion method was modified, full FHL muscle relaxation was evident.
3. Active Ankle Flexion – Unloaded: sEMG data was observed in all volunteers. Signal amplitudes increased by 10% on average compared to FHL only test.
4. Active Ankle Flexion – Loaded: sEMG data was on average 40% higher in amplitude compared to 'FHL only' section.

2.9.2 Dynamic US

During ankle plantarflexion a number of observations were common across all individuals: (1) the ATR shifts upwards; (2) DP moved downwards; (3) PW slid over CST into the bursal space. These movements were reversed during dorsiflexion.

1. FHL only: No PW motion was observed (PWSD = zero)). PW only seemed to move when the AT insertion angle changed. The deep fat pad was observed to move as the FHL contracted or flexed.

2. Passive ankle flexion: PW was observed to slide a distance 1.5 – 9 mm (mean = 4.8 mm, SD = 1.57).

3. Active ankle flexion – Unloaded: The range of PWSD increased to 2.5 – 11 mm (mean = 7.4 mm, SD = 0.76). PW moved to within 2.5 – 5.5 mm of the most proximal point of the AT insertion.

4. Active ankle flexion – Loaded: PWSD reached 3.5 – 17.5 mm (mean = 11.2 mm, SD = 3.33). The distance between the tip of PW and the most proximal point of the AT insertion reduced to 0.5 – 2 mm (Figure 3.9).

Calculating the correlation coefficients of result groups and comparing readings using Wilcoxon matched pairs test² showed no significant difference between PWSD and body mass index (BMI)³, weight, height, age or gender (in passive ankle flexion, active ankle flexion and loaded ankle flexion) (Figures 3.10-3.15). PW was found to slide further when the AT was loaded as opposed to unloaded ($r^2 = 0.84$). Statistical analysis showed the two groups are statistically different ($P < 0.01$). Similarly, PWSD during active ankle flexion was greater than during passive ankle flexion ($P < 0.01$), highlighting a strong linear relationship between PWSD and ankle load ($r^2 = 0.87$) (Figures 3.16 & 3.17).

² T-test was not used as the results were not evenly distributed, hence, non-parametric testing was utilized

³ BMI is calculated using the equation, $BMI = \frac{weight}{height^2}$

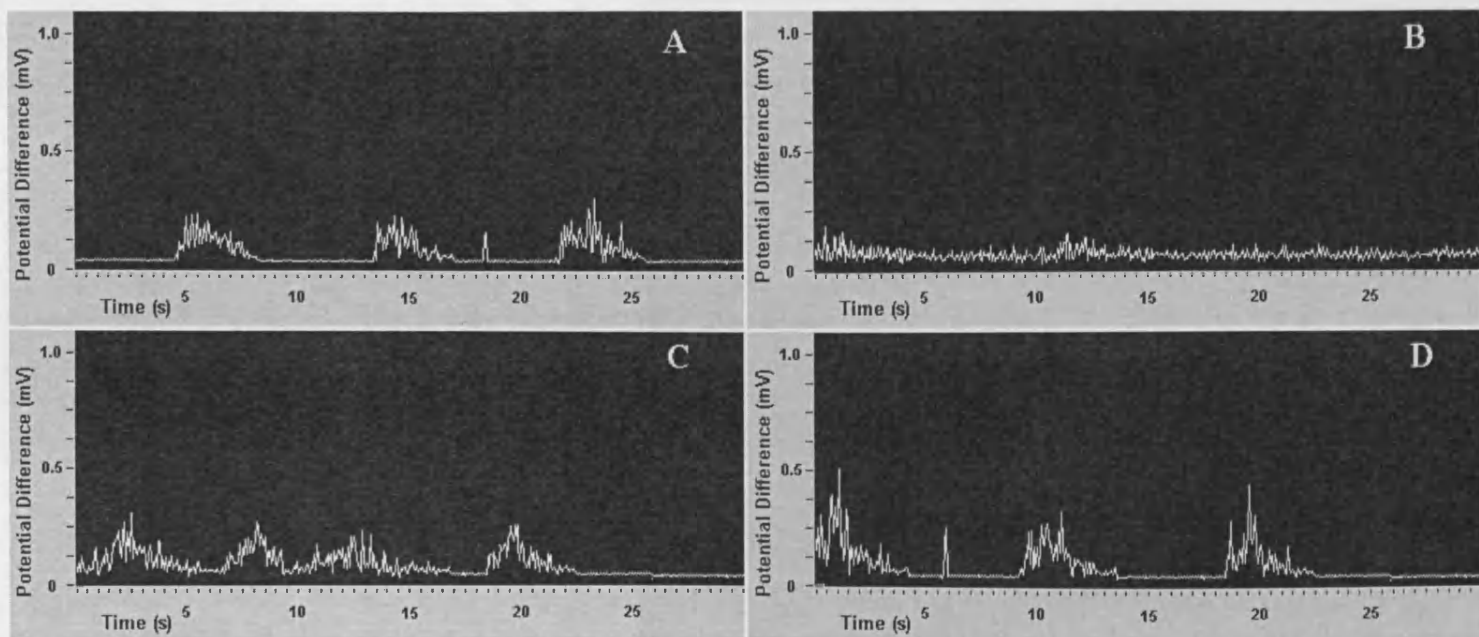


Figure 3.8 sEMG data on one volunteer monitoring of FHL. During FHL only (A), FHL activities were evident as the big toe was actively flexed. No FHL activities were detected during passive ankle flexion (B). During active ankle flexion – unloaded condition (C), EMG data were 10% higher on average compared to FHL only. EMG results increased by 40% under loaded conditions (D) compared to FHL only. This shows FHL activities were observed in all parts of the protocol except during passive ankle flexion.

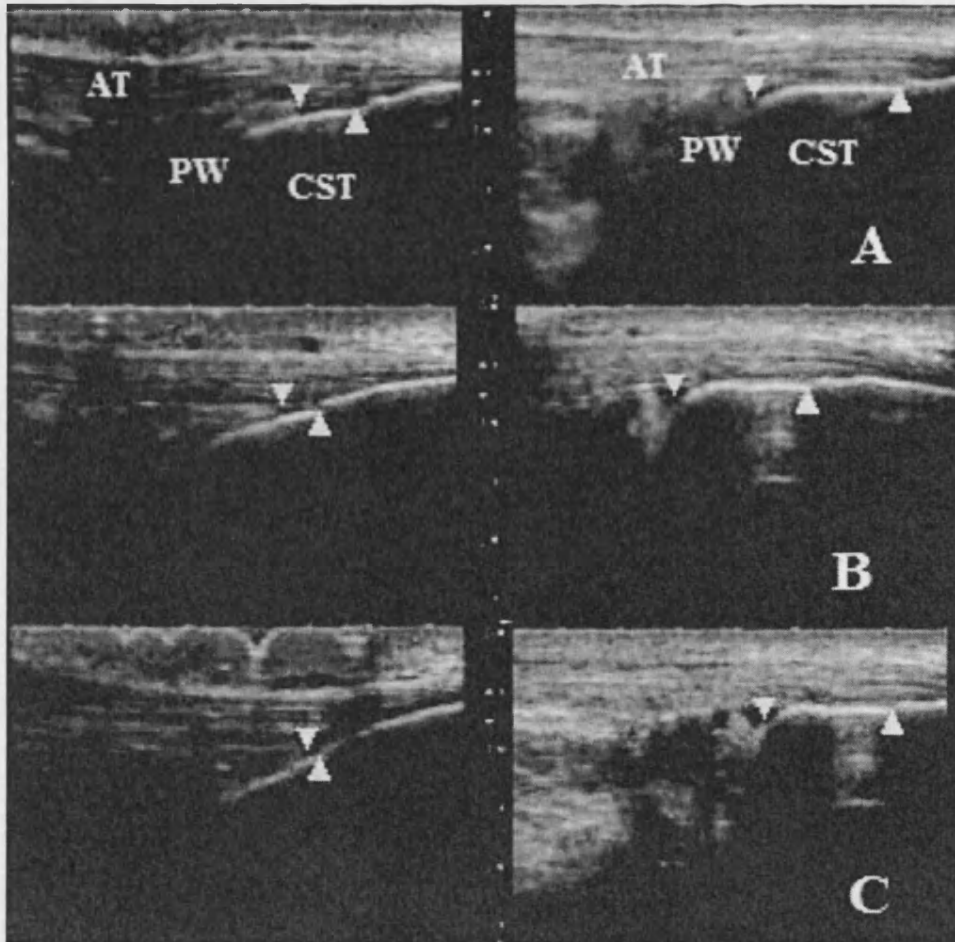


Figure 3.9: US images illustrating PW motion between plantarflexion (left) and dorsiflexion (right). **(A)** PW sliding was evident during passive flexion. **(B)** PW travelled further during active flexion – unloaded, compared to passive flexion. **(C)** Under active flexion – loaded conditions, PWSD travelled to its maximum range, in some cases PWSD was observed to reach the AT insertion point during maximum plantarflexion. ▼ = tip of PW, ▲ = most proximal point of AT insertion, AT = Achilles tendon, PW = protruding wedge, CST = calcaneal superior tuberosity. Scale bar (cm)

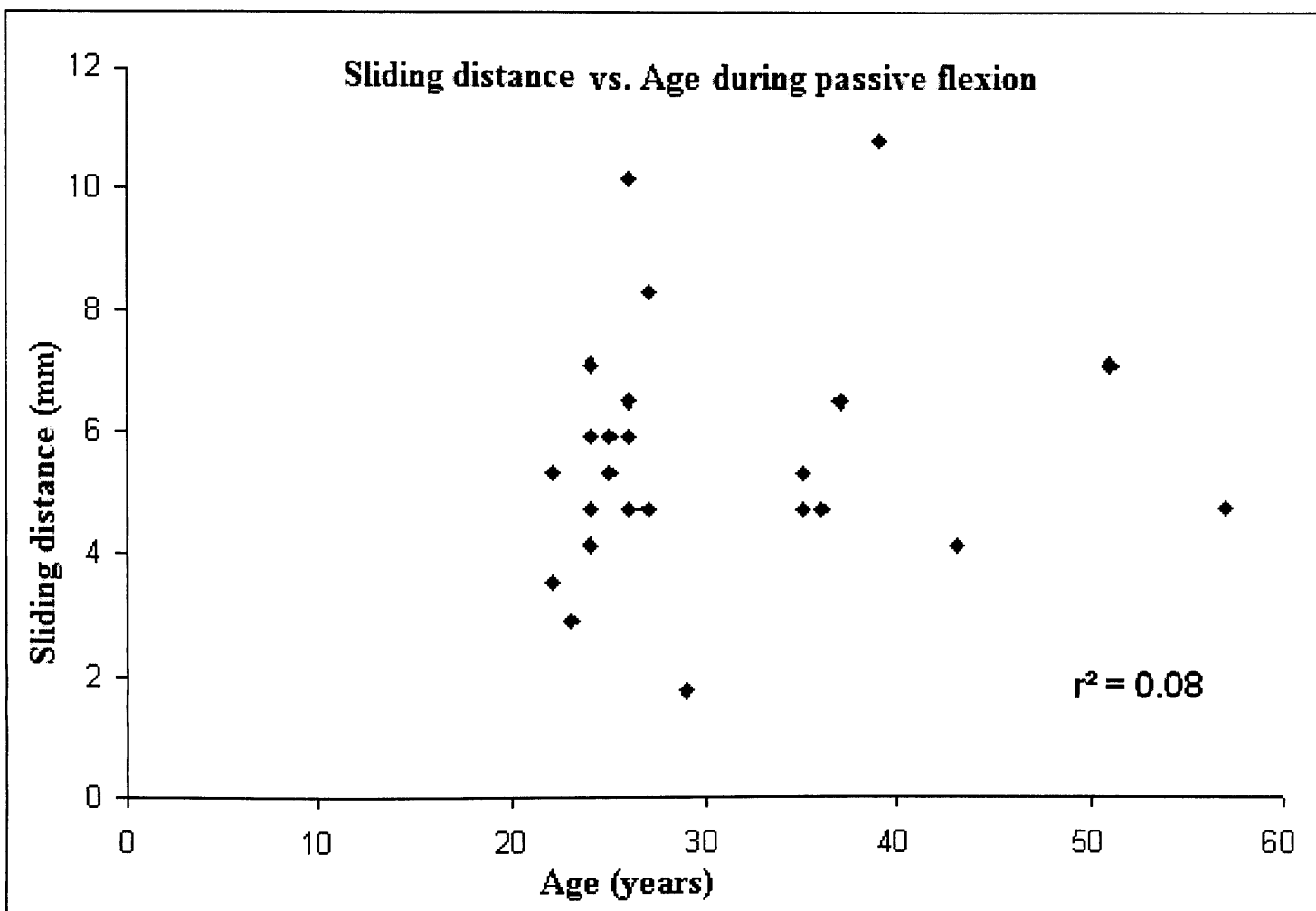


Figure 3.10: PW's sliding distance (PWSD) during passive ankle flexion showed no obvious relationship with age.

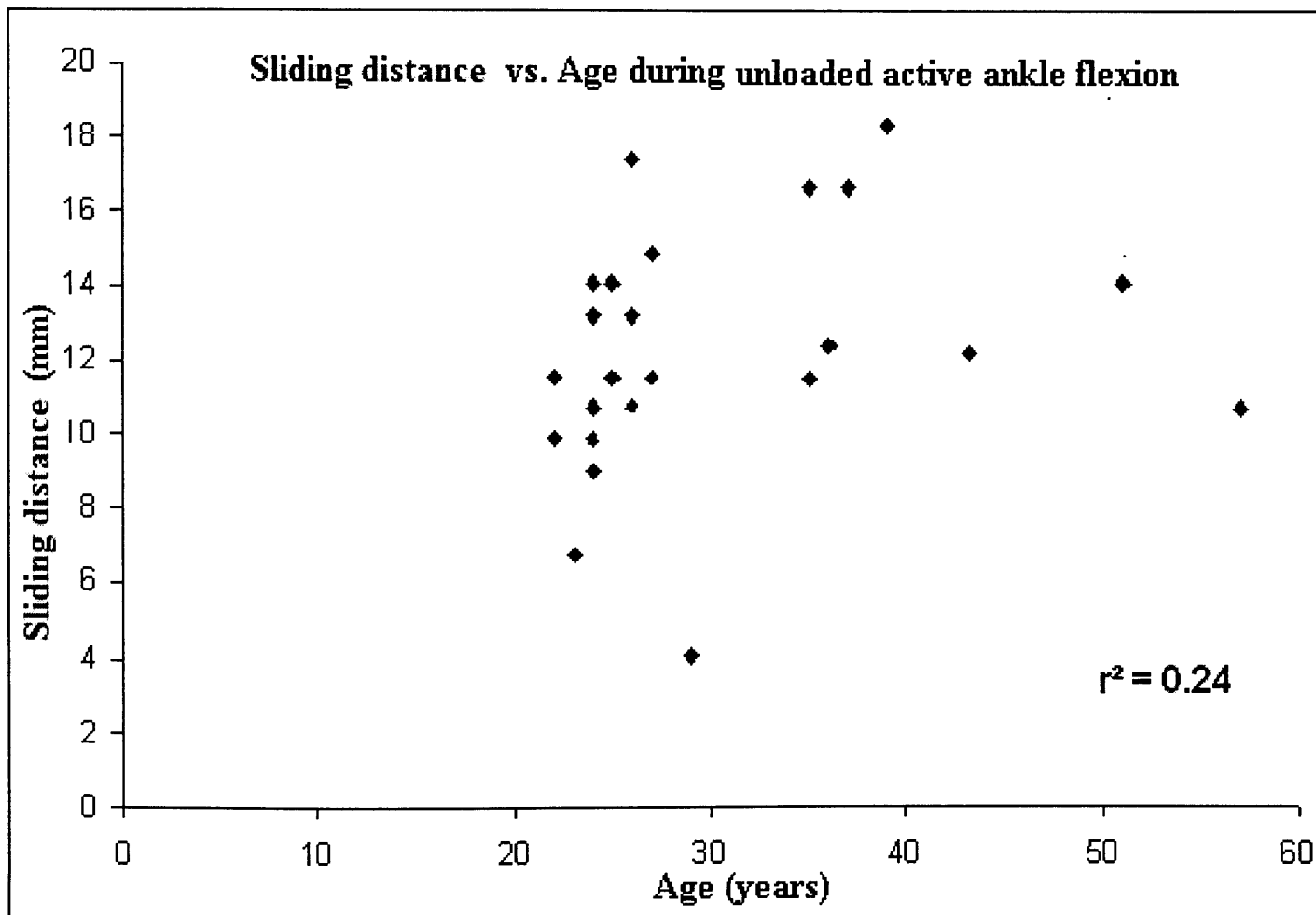


Figure 3.11: PWSD during active ankle flexion (unloaded) showed no obvious relationship with age.

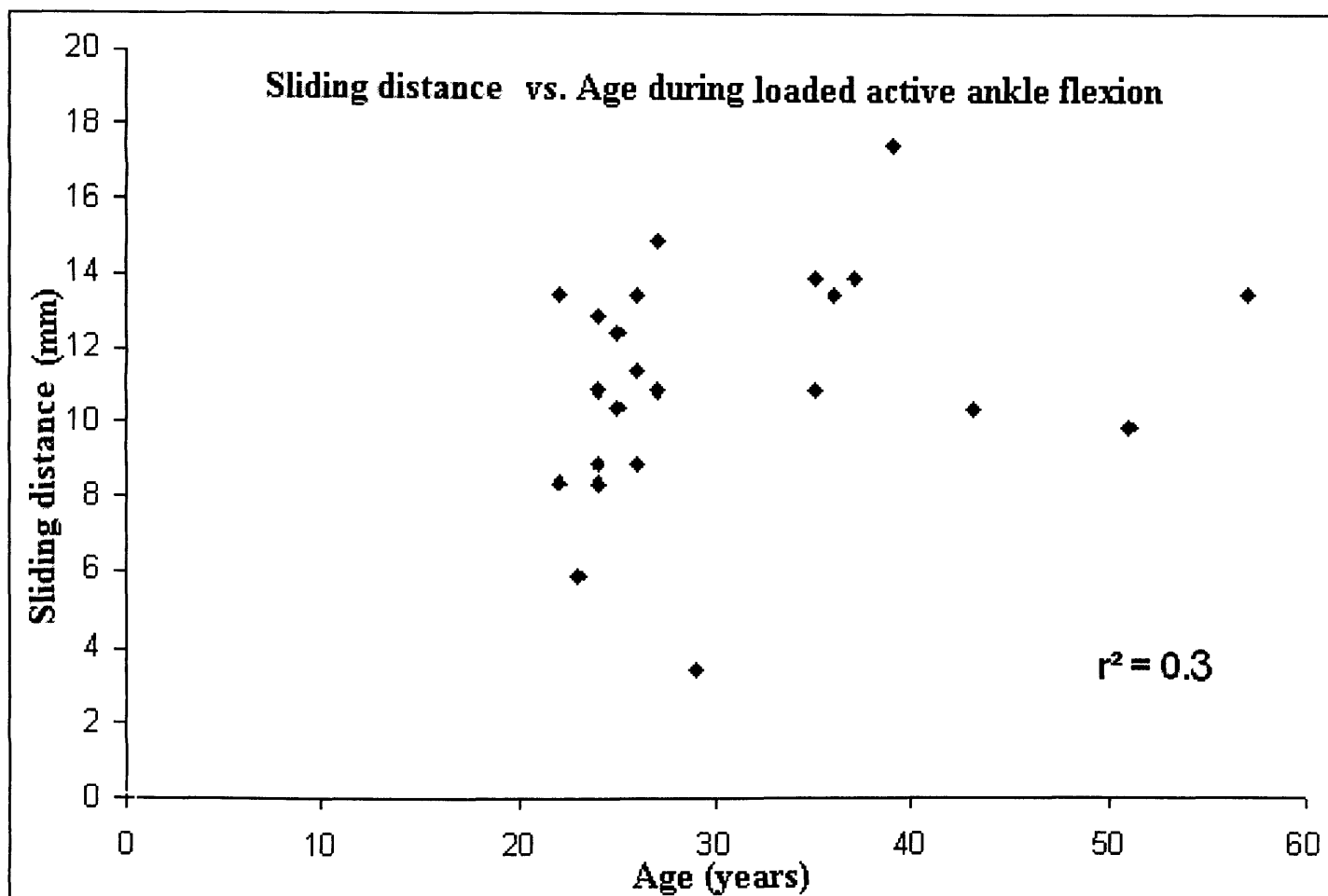


Figure 3.12: PWSD during active ankle flexion (loaded) showed no obvious relationship with age.

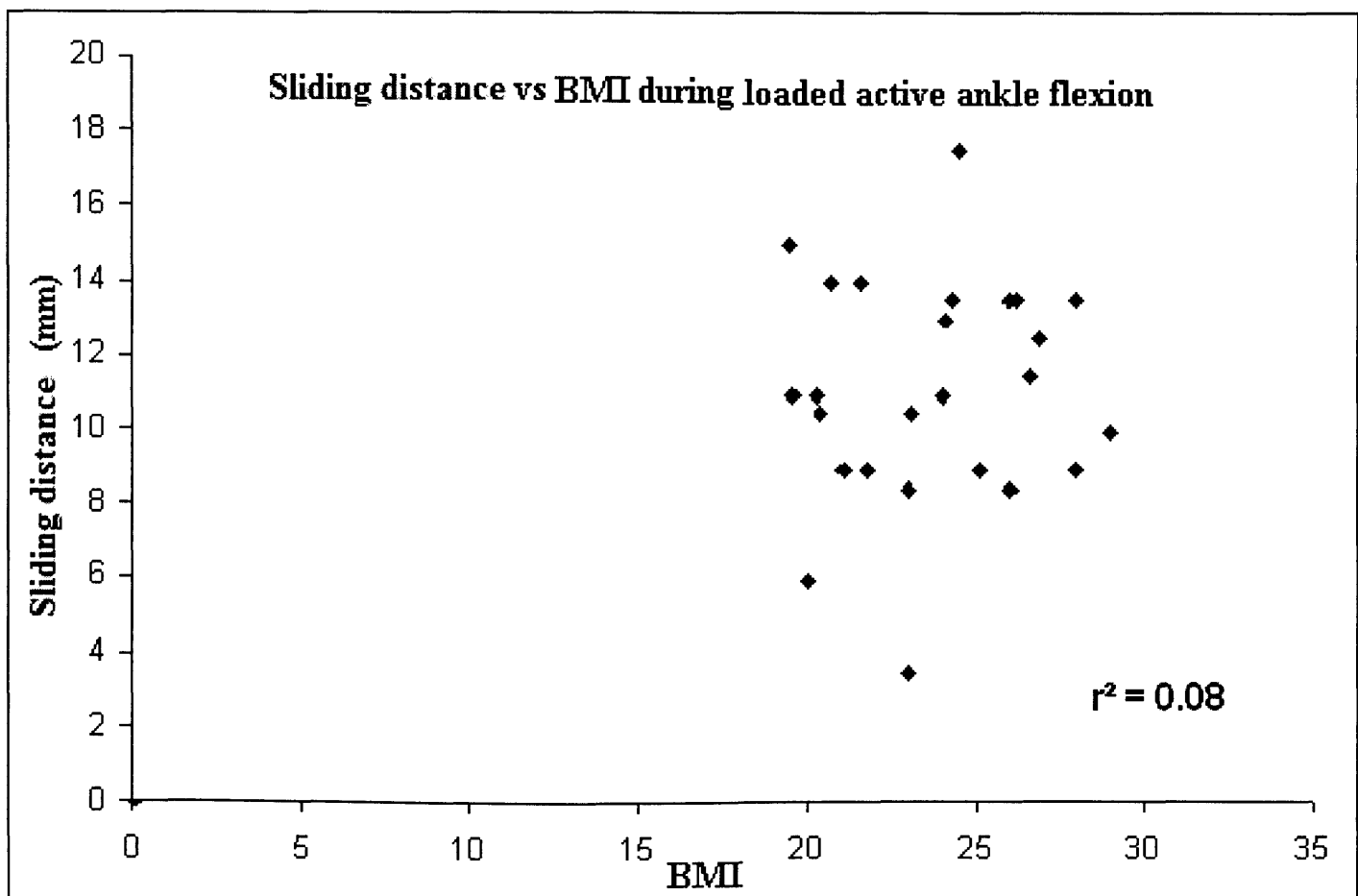


Figure 3.13: PWSD during active ankle flexion (loaded) showed no obvious relationship with body mass index (BMI).

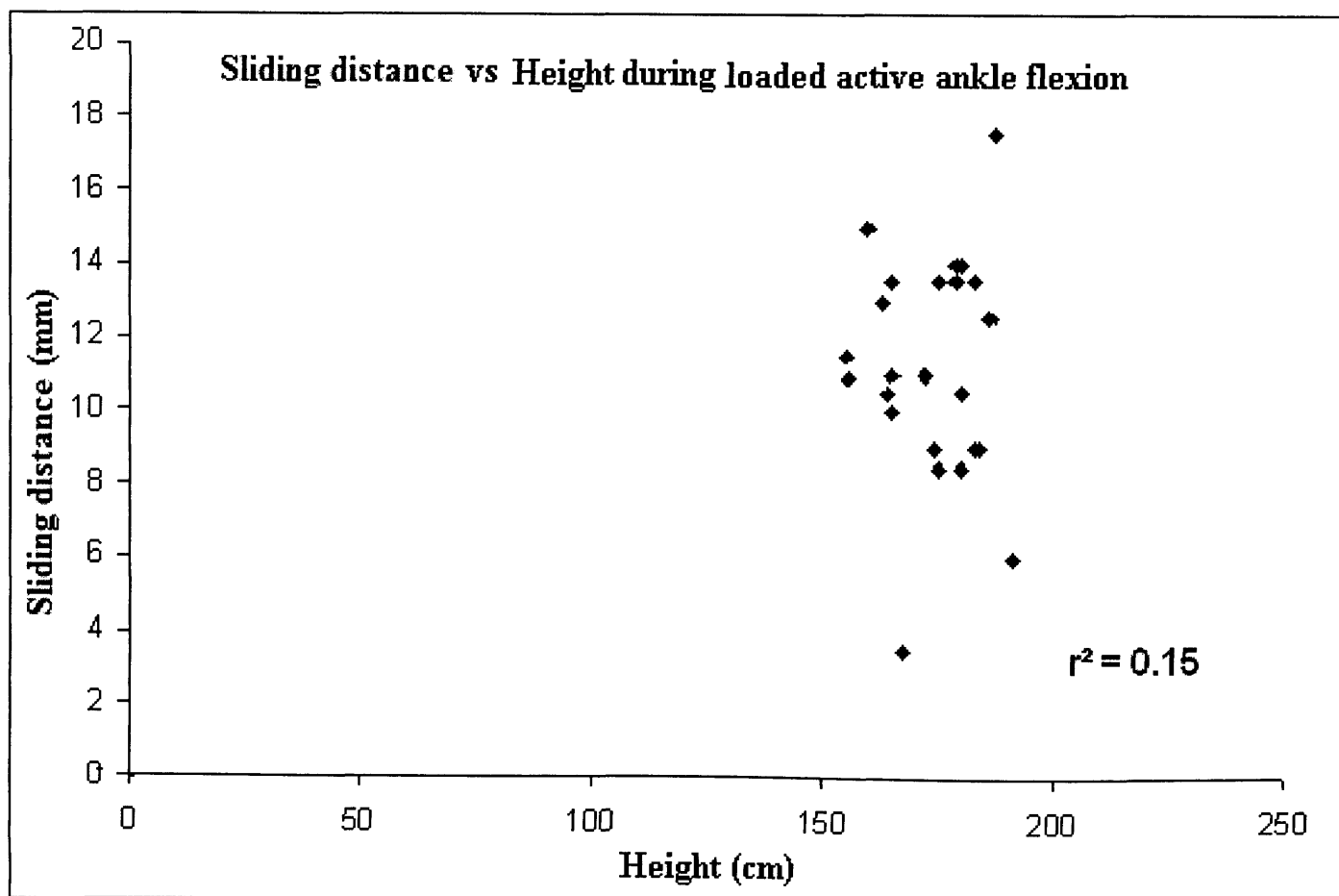


Figure 3.14: PWSD during active ankle flexion (loaded) showed no obvious relationship with volunteer's height.

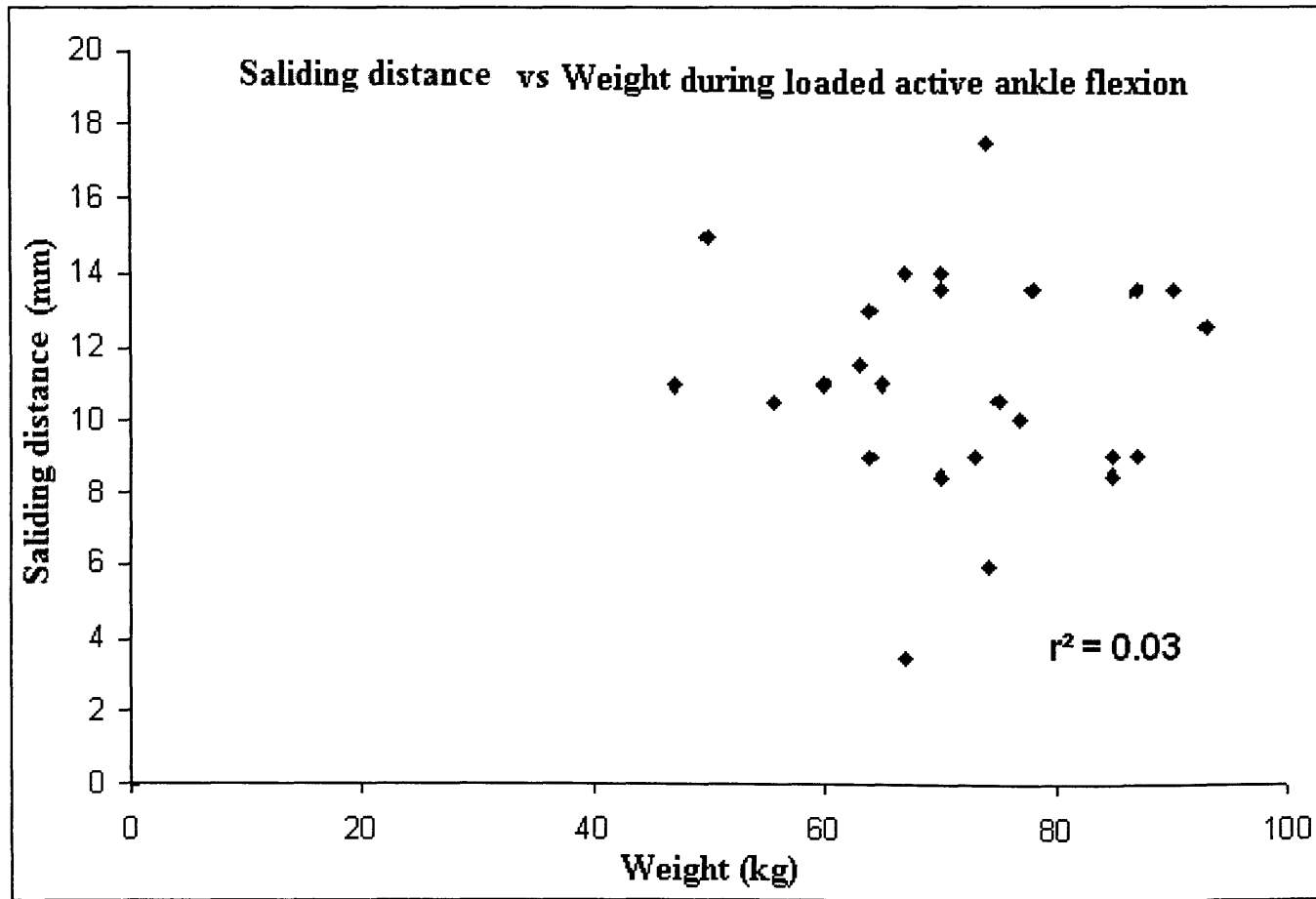


Figure 3.15: PWSD during active ankle flexion (loaded) showed no obvious relationship with volunteer's weight.

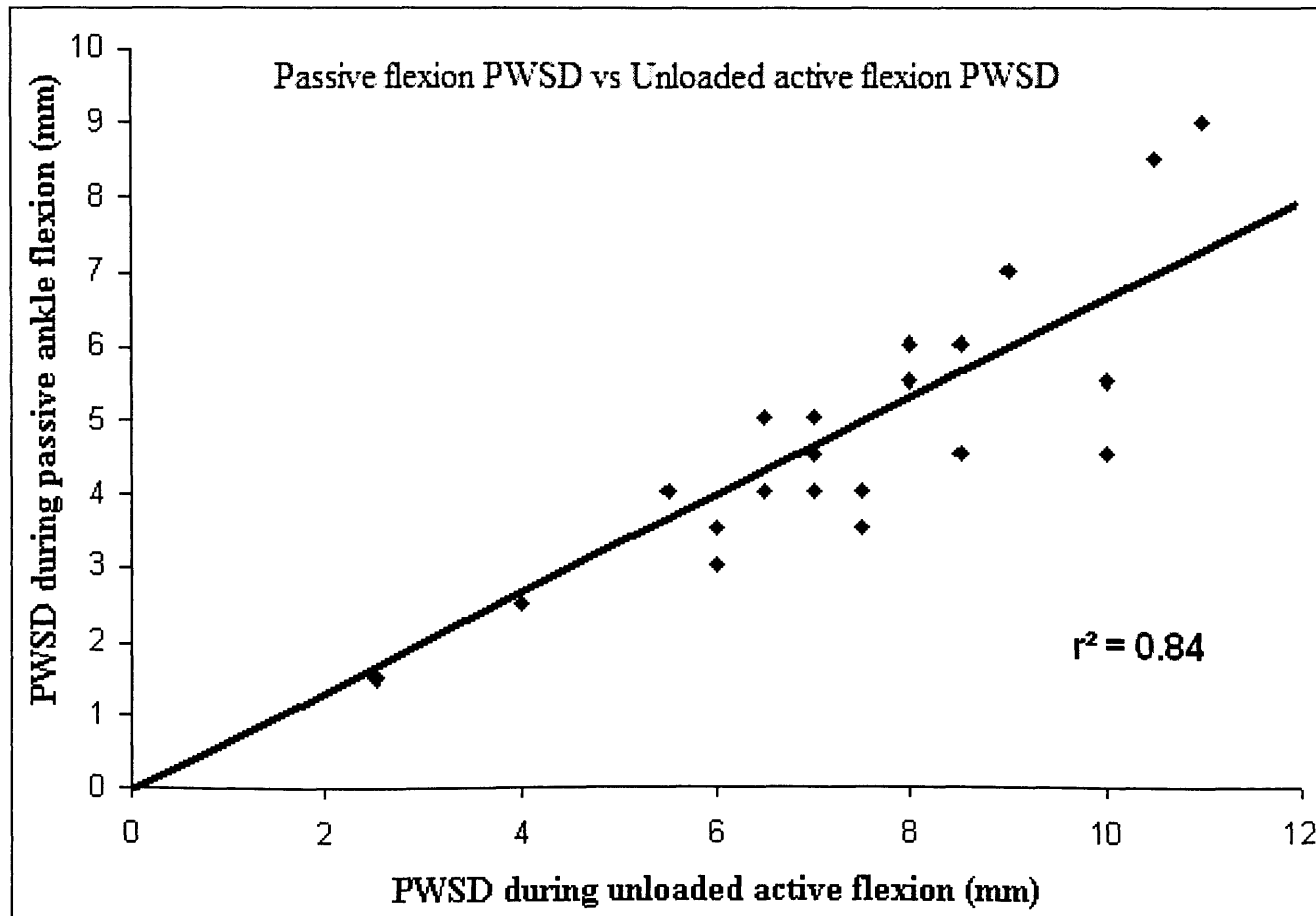
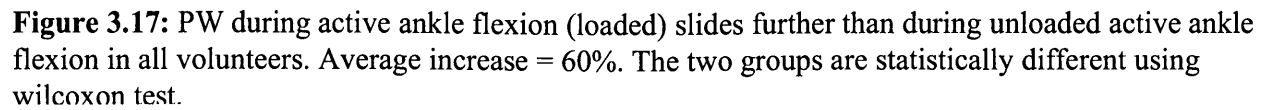


Figure 3.16: PW during active ankle flexion (unloaded) slides further than during passive ankle flexion in all volunteers. Average increase = 60%. The two groups are statistically different, using wilcoxon test.



2.10 Discussion

Literature review suggested that FHL contractions can be a factor to control movement of the protruding wedge. During active ankle flexion (loaded and unloaded) and FHL only, sEMG data showed FHL activities in all volunteers; and although DP was observed to move with FHL's activities, no PW motion was recorded during 'FHL only'. In addition, during passive ankle flexion PW motion was observed in all volunteers, with no obvious FHL contractions. This shows no influence of FHL over the position of PW, and hence, suggests PW's motion mechanism is not encouraged by FHL activities as previously was theorized. Inter-volunteer results also showed that PWSD is not influenced by age, gender, weight or BMI. PWSD increases between passive, active and loaded ankle flexion indicating PWSD is affected by load. This supports the hypotheses that PW serves to assist in subtendinous lubrication, promoting lower levels of wear and tear at high loads [15]. The relationship between load and PWSD can be speculated to be caused by the level of relaxation of AT. When the ankle is flexed in plantarflexion during passive or unloaded active flexion modes, AT was observed to start bending as the ankle reaches its maximum plantarflexion position (Figure 5.10). Such bends are affected by the load, where AT kept its straight shape at maximum plantarflexion position under maximum loading condition (Figure 5.11). The effect of loading and AT kinks were studied and reported in Chapters 4 & 5. Furthermore, PW was observed sliding to the distal extremity of the retrocalcaneal bursa under loading conditions, supporting suggestions that PW assists in removing dead cells from within the bursal space by being attached to the synovial membrane of the PW during ankle flexion and extension [21].

The anchorage between PW and the calcaneus was also considered as a controlling factor to PW's motion. Since PW motion is recorded against the direction of calcaneal rotation during ankle flexion, the motion of PW's tip is restricted by the anchorage rather than influenced by it. As PW's tip forms the superior synovial folds of the retrocalcaneal bursa [1,15,36], and the retrocalcaneal region is surrounded by retinaculae and fascia to support the AT from excessive bending [43], PW is still thought to have a strong relationship between its sliding distances and the insertion angle or AT entheses. However, it is still not clear whether PW motion is caused by this change in AT angle.

2.11 Conclusions

- PW's tip position was independent of FHL activities, gender, age, BMI, height, weight and foot orientation.
- The displacement of the calcaneus does not influence PW's motion.
- No contralateral differences were observed.
- PW was found to move with changing AT insertion angle, however, the extent of this relationship is still not established at this stage.
- A strong relationship exists between PWSD and ankle load, until PW's tip reaches the most proximal point of AT insertion.
- The extent of this movement supports concepts that PW assists in lubricating the subtendinous region, reducing the level of wear at high levels of loading; subsequent benefits may include the PW assisting in removing dead debris caused by wear and tear within the retrocalcaneal bursa.

2.12 Next Chapter

Following the relationship found between ankle load and the motion of PW's tip, the next chapter describes the test carried out to assess the extent of influence ankle load has over PW's motion. In addition, the test examined the influence of ankle's flexion angle (or AT insertion angle) over PW's motion to better understand the nature of motion.

Chapter 4

Effects of Ankle Load & Flexion Angle on PW's Motion

2.13 Introduction

Results from previous testing (Chapter 3) indicated a strong relationship between PWSD and both plantarflexion loading and the AT insertion angle (ATIA), supporting speculations of the insertion angle controlling the motion of KFP [1,36]. However, results did not show the extent of such influences. Literature review suggested KFP performs an important role to reduce pressure change within the retrocalcaneal bursa during ankle flexion [1,3,4,21,36]. Studying the extent of these influences can help determine the mechanism of PW motion during ankle flexion and assist in understanding its biomechanical importance within the AT enthesis organ.

Having previously proved no influence of FHL over PW's position, this study is focused on investigating the extent of influence that both the plantarflexion loading and the flexion angle have on PWSD. This study will also examine PW's distance from the AT insertion point (PWD) during ankle flexion and the influence plantarflexion load and ankle flexion angle have on PWD.

2.14 Materials & Methods

A number of techniques were used to measure PWSD, PWD, ankle flexion angle and plantarflexion load control.

2.14.1 US Examination of PW Sliding Distances

The same dynamic US scanner used for the previous test (Toshiba Aplio - with a linear transducer operating at 12 MHz) was utilized to scan the hindfoot. To measure PWD and PWSD, the tip of PW and the most proximal AT insertion point were used as landmarks. The insertion angle was measured by drawing a line along AT fibre line and another over the most prominent features of CST (Figure 4.1). US images were also used to measure PWSD and the AT insertion angle (ATIA) using easily located landmarks.

4.2.2 Plantarflexion Loading Rig

As no commercial mechanical rigs or frames were available for this research, a rig was built to ensure;

- Full ankle flexion, which is unrestricted by the rig's components
- Enough space behind the ankles for the US transducer to scan the ankle
- Minimum offset load on the ankle

The mechanical frame was constructed using hollow stainless steel square tubs. The frame's components can be divided to 3 sections; volunteer interaction parts, load attachment parts and configurability (Figure 4.2). The two areas of contact between the volunteer and the rig are the knee rest and the ankle holder. Sitting on an external chair, volunteers place their knee on the knee rest and their ankles in the ankle holder. This arrangement eliminates offset weight caused by the volunteer's leg. The knee rest is made of a layer of sponge contained within a cotton sheet. The ankle holder's pivot can be aligned with the ankle's pivot and has a flexible flap at the metatarsal area to secure the foot to the rig. The load management parts consist of 2 pulleys holding a climbing rope (4mm thick, able to hold 50 kg⁴) that connects the ankle holder to the load bearer.

⁴ The climbing accessory rope was purchased from

Weights are placed on the bearer and are pulled against direction of gravity during ankle plantarflexion. The knee rest, ankle holder and the weights bar are all attached to the main chassis via sliding three-way connectors.

Ankle Flexion Angle Measurement

Principally, the flexion angle can be either measured from medical imaging techniques (US for real time imaging abilities), or by measuring the physical ankle flexion angle using electronic goniometers. Although using US images is limited to the US video refresh rate, the results reflect the effective ATIA, rather than the ankle's angle of flexion. Electronic goniometers require attaching a separate device to the volunteer's ankle or to the loading rig. Since no previous studies were found comparing both techniques, this study utilized both methods to monitor the ankle flexion angle and ATIA. This can also help evaluating the relationship between ATIA and ankle flexion angle (AFA).

2.14.1.1 US Examination of AT Insertion Angle

The AT insertion angle is measured from US images using anatomical landmarks (Figure 4.1). Using dynamic US imaging, ATIA is measured by locating anatomical landmarks, a straight line is drawn connecting prominent features of CST. The angle between this line and AT fibre line represents ATIA. This method was evaluated (pilot study, section 4.2.4.2) for repeatability and showed a maximum error of 2° (8%) with a variance coefficient < 0.125 (average error = 1° = 4%).

2.14.1.2 Goniometer Measurement of Ankle Flexion Angle

A number of goniometers were considered for this study. Pressure sensor based goniometers that can be attached to the ankle have high recording precisions (up to 0.1° accurately). However, goniometers that require strapping components to the ankle were not considered to avoid applying any restrictions on the ankle's freedom of flexion.

This study used a 25 mm® motion sensor from Gill Sensors Ltd (data sheet attached in appendix VI) (Figure 4.3). The sensor is made of 2 parts; an activator and a receiver. The activator is a 'U' shaped metallic sheet and as the receiver unit slides through it, the magnetic field around the receiver changes. The receiver gives an electrical signal with amplitudes that reflect the position of the receiver with respect to the activator. The goniometer was mounted on the ankle holder's pivot on the rig through designated holes on both the activator and receiver.

The goniometer's maximum range is 90°, where the ankle flexion range for this study's volunteers ranged between 55° to 100° (average 68°) (Pilot study section 4.2.4.2). In order to ensure recording full ankle flexion range of every volunteer, 2 gears were connected (40 tooth and a 20 tooth gears) to make a gear that rotates at the ratio of 2:1. This increased the goniometer's range to 180° (Figures 4.4), halving its precision as a trade off to increasing its range. A free software package was provided by Gill Sensors Ltd that provides real-time processing, at 1 kHz, and views time-stamped data, as well as storing the results for offline processing.

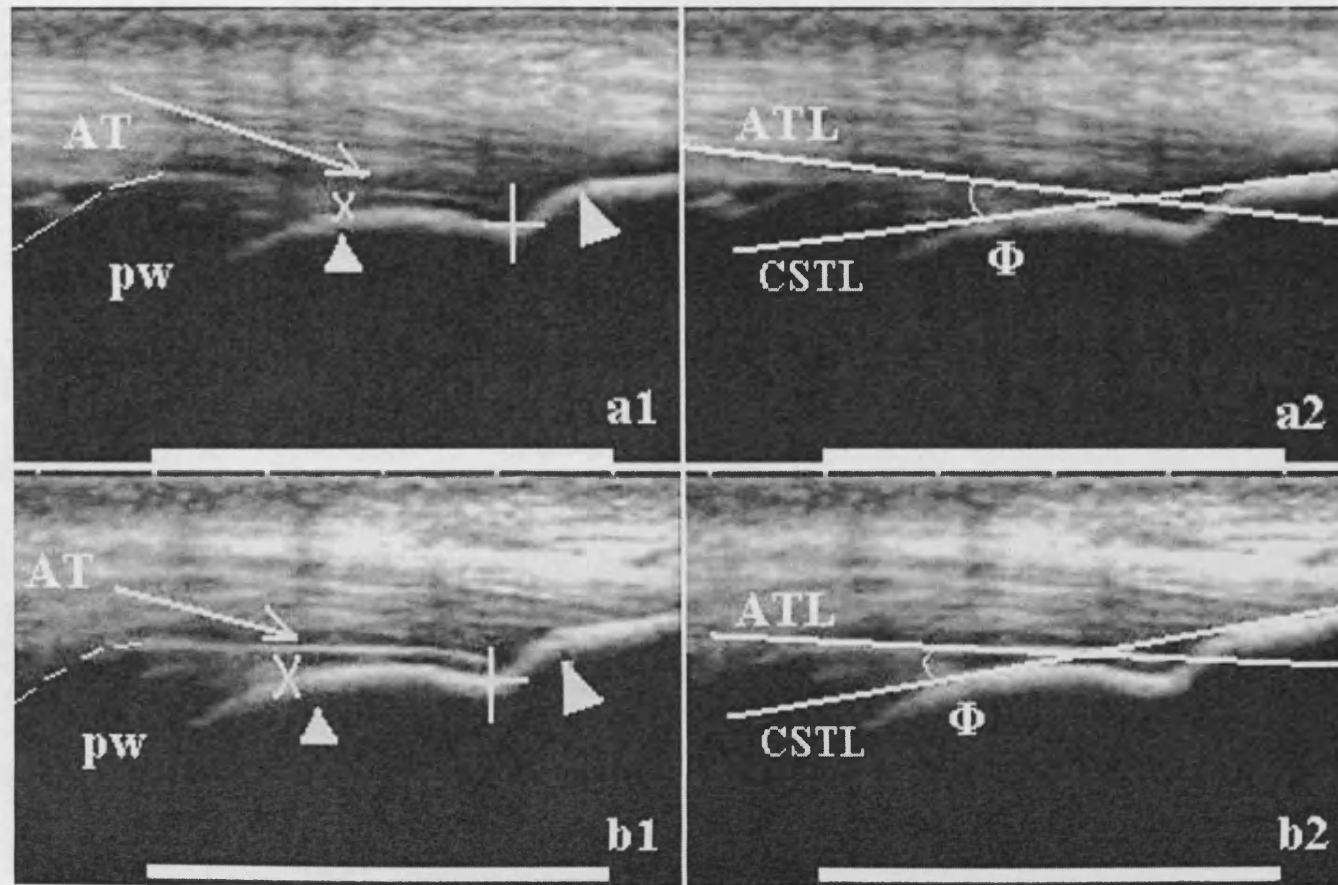


Figure 4.1: US images taken in the Saggital plane of a volunteer while flexing the ankle between maximum dorsiflexion and maximum plantarflexion positions. (a1 & b1) show anatomical landmarks used. To measure PWD, AT insertion point (+) and the tip of PW (x) were used. To measure ATIA (Φ) between AT and the posterior wall of CST, the anterior wall of AT (arrow) was used as the AT line (ATL), where CST line (CSTL) was drawn over the 2 most prominent points of the calcaneus (triangles). Dotted line represents the fibrous separation between AT-related pad and PW. Scale bar = 1 cm

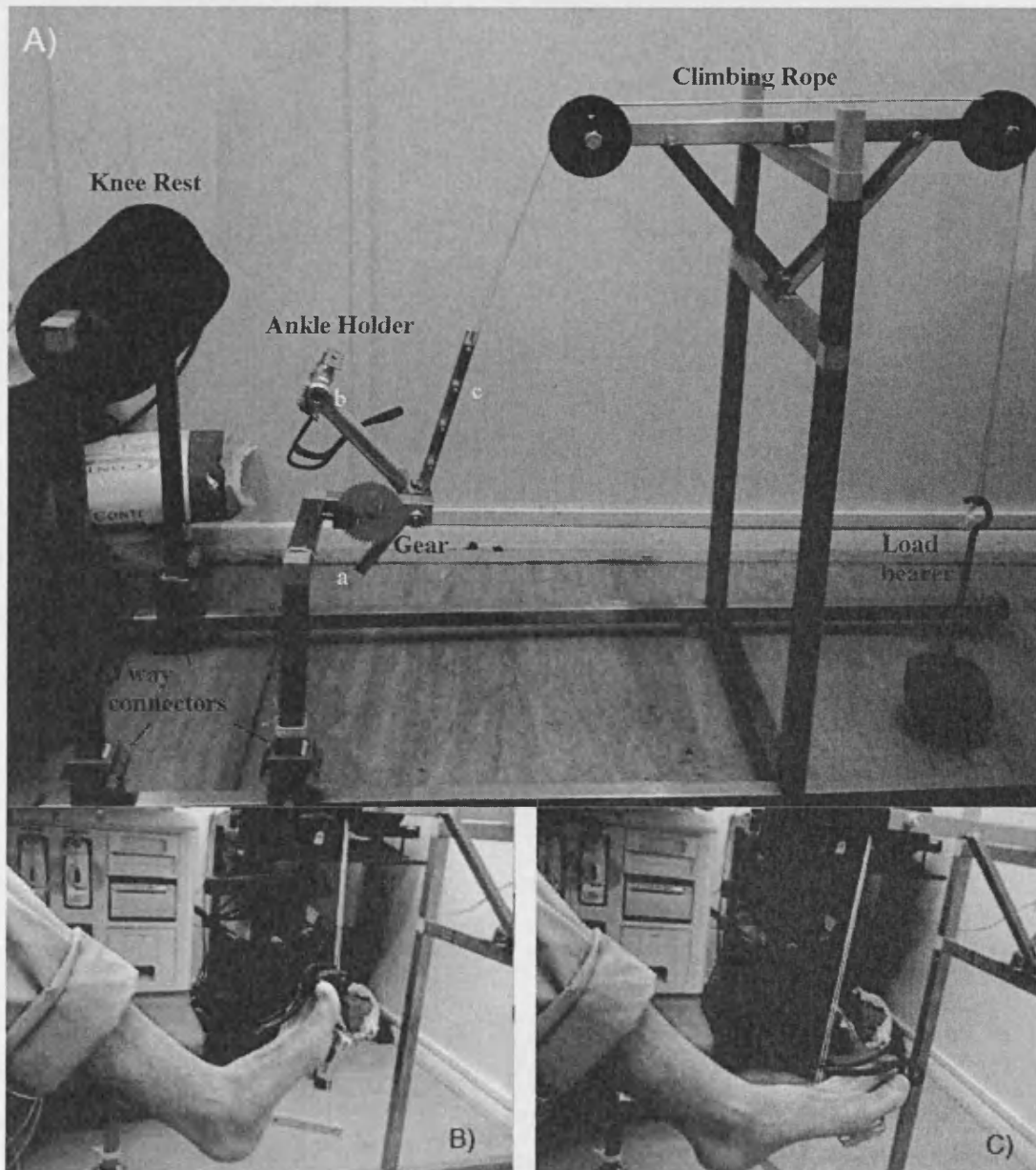


Figure 4.2: (A) A photograph of the implemented loading rig with 2 kgs loaded on the bearer. The load bearer is attached to the ankle holder via a 4mm climbing accessory rope in any of the 3 sites (a,b,&c), depending on the volunteer's range of ankle flexion. The rig allows unrestricted volunteer ankle flexing between dorsiflexion (B) and neutral positions (C). The knee rest and ankle holder arrangement eliminates offset weight caused by the volunteer's leg and the rig's components.

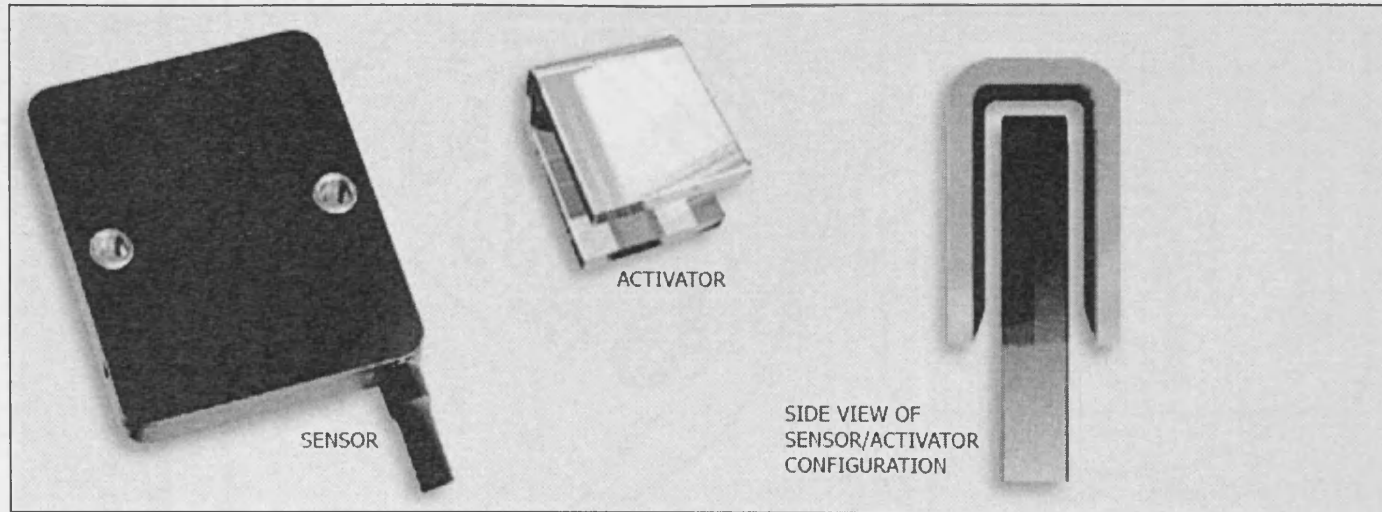


Figure 4.3: The electronics goniometer used for this study (25 mm Blade Sensor, Gill Sensors Ltd). It consists of a transmitter (ST) and a receiver (SR). Based on magnetic field detection, this receiver gives signals that reflect the position of the transmitter with respect to the receiver.

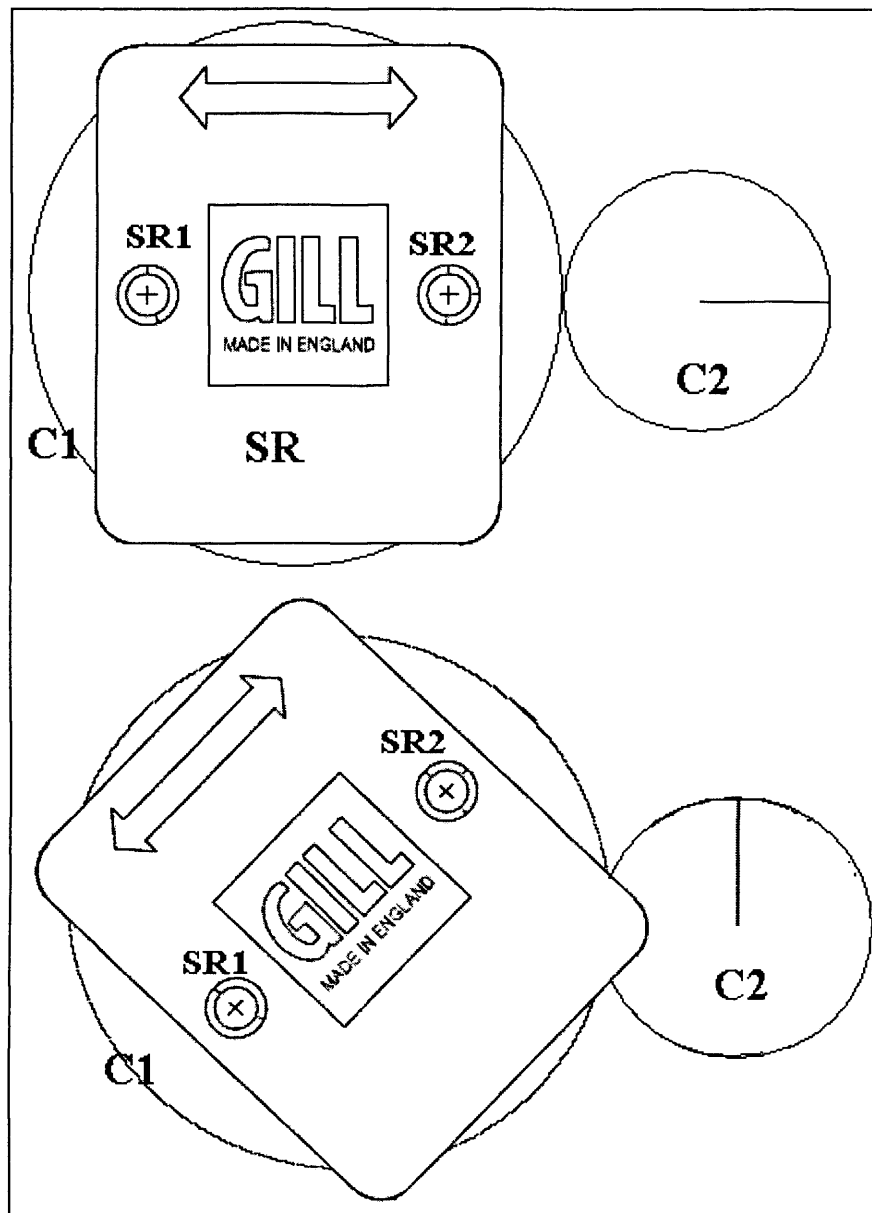


Figure 4.4: A schematic illustrating how the goniometer sensor's effective range was doubled by placing it on the larger gear (C1 from the previous figure 4.5). When C2 rotates at 90°, C1 rotates at 45°.

2.14.2 Pilot Studies

4.2.4.1 Plantarflexion Load Range

A pilot study was carried out to examine the level of loads required for this study. Loads were placed on a padded surface on the volunteers knees while sitting up on a chair. The hind foot of 5 volunteers was scanned during ankle flexion using dynamic US to determine PWSD. Since the plantarflexion load offset is constant for every individual, this test can indicate the range of loads that influence changes in PWSD. Loads used ranged from 1 kg to 30 kg, in addition to half body load (double foot stance) and full body weight (single foot stance). Results showed that PWSD reaches its maximum range against ankle loads of under 2 kgs for 4 volunteers and under 4 kg for 1 volunteer. The loads used for this study are 100 g, 500 g, 1 kg, 2 kg, and 5 kg.

4.2.4.2 Protocol Evaluation

The protocol was repeated 5 times on 2 volunteers. Repeatability results showed a maximum error of 0.5 mm (5%, variance coefficient < 0.125) in PWSD measurement, and a maximum error of 2° (8%, variance coefficient < 0.125) in measuring ATIA. The electronic goniometer is calibrated at the time of testing for each volunteer to set the baseline value (neutral position = 0°). Results showed each volunteer flexed their ankles to within 5° of the full flexion range. Mounted on the gears, the accuracy of the electronic goniometer was tested by manually rotating the ankle holder between 90° and -90° from the horizontal line using a manual goniometer (Table 4.1). The gears caused the goniometer to rotate at a ratio of 2:1 enabling accurate measurement of AFA across the entire flexion range.

Ankle holder's angle	90°	60°	30°	0°	-30°	-60°	-90°
Goniometer's angle	45°	30°	15°	0°	-15°	-30°	-45°

Table 4.1: Testing the gear installed between the electronic goniometer and the loading rig. Results showed that the gearing provided the required ratio of 2:1

4.2.4.3 Ankle Flexion Speed

Volunteers flexed their ankles at 2 different rates. A training session with a stopwatch was conducted prior to the test. First, ankles were flexed at a rate of 1 flexion cycle (plantarflexion - dorsiflexion – plantarflexion) in 4 seconds, similar to the average comfortable flexion speed that volunteers were found to do in chapter 3 results. This was repeated 5 times. The test was then repeated 5 times at the rate of 1 flexion cycle in 2 seconds. Results showed (Table 4.2) PW sliding speed initially (4s cycle) was on average 3.25 mm/s (SD = 0.75 mm) increasing to 7mm /s (SD = 1.7 mm) during 2s flexion cycles. However, no obvious changes were observed in PWSD, PWD, or PW hysteresis (Section 4.3.2) with changing PW sliding speed. T-test showed no significant difference.

Flexion speed	Maximum PWSD (mm)	Minimum PWD (mm)
4 s flexion cycle, 1 st scan	10.5	3
2 nd scan	10	3.5
3 rd scan	10.5	3
4 th scan	9.5	3
5 th scan	10	3.5
2 s flexion cycle, 1 st scan	10	3.5
2 nd scan	10.5	3.5
3 rd scan	9.5	3.5
4 th scan	10	3
5 th scan	10.5	3

Table 4.2: Pilot study results showing differences in PWSD and PWD during 4 s ankle flexion cycle, compared to 2 s ankle flexion cycle in one volunteer

2.14.3 Volunteers Selection & Preparation

For this test, volunteers had to have a healthy ankle and have no history of surgery within the ankle or any serious injuries. As previous testing showed no relation between PWSD and age, BMI, or gender, volunteers for this test were from similar age group (20-28).

2.14.4 Study Protocol

The hind foot of 5 volunteers (2 females & 3 males, Age 20-28, BMI 20-28) was scanned to look into the influences of ankle loading and ankle's flexion angle on PW motion, volunteers sat on a patient bed with their ankle attached to the loading rig. Volunteers flexed their ankles repeatedly between plantarflexion and dorsiflexion against incrementing loads (100 g, 500 g, 1 kg, 2 kg, and 5 kg). US images and goniometer data were time stamped and stored for offline processing to measure PWSD, PWD and ATIA.

2.14.5 Statistical Analysis

Statistical analysis of the data was performed using the t test (two-tailed) and Wilcoxon test. A significance level of 0.05 was adopted.

2.15 Results

2.15.1 Ankle Flexion Angle vs. AT Insertion Angle

Comparing Ankle flexion angle results obtained from the electronic goniometer against ATIA measured from US images. At 100g, a non linear relationship was found between ATIA and ankle flexion angle (Figure 4.5) in 4 of the volunteers. This relationship became linear or 'straighter' as the load increased. This relationship was found to be consistent in all volunteers. Statistical analysis carried out using Wilcoxon showed that the difference between ATIA and ankle flexion angle is significantly different in all volunteers.

2.15.2 Examining PWSD & PWD Variations Against Ankle Load

At 100g plantarflexion load, PWSD ranged from (2.5 – 5.5 mm (mean = 4 mm, SD = 0.52)). PWSD increases (Figure 4.6), and reaches the maximum range (4 – 12 mm (mean = 8 mm, SD = 3.08)) when the plantarflexion load is 2kg. On the other hand, PWD seemed to reach distance of (3.5 – 6.5 mm) under 100 g loading. PWD decreases exponentially (Figure 4.7) and reaches its minimum distance to AT most distal insertion point (2 – 4 mm) under 2 kg loading.

The effects of ATIA and load on PWD were examined from US images. PWD has a linear relationship with ATIA (Figures 4.8 & 4.9). The relationship between ATIA and PWD was consistent in all volunteers; however, this relationship varied slightly in graph shape between volunteers. Increasing load does not change the nature of this relationship, but increases the ATIA range (mean at 100 g load = 38°, at 5 kg = 49°). For this study's volunteers, the shape of CST was categorized into straight and single-dome shapes (for this study only, these categories do not include all CST shapes studied in previous studies [44]). Volunteers with similar CST shapes showed similar PWD-ATIA graphs (Figures 4.10 & 4.11).

The PWD-ATIA relationship shown above was measured only during the dorsiflexion part of ankle flexion cycle (ankle flexing from maximum plantarflexion position to

maximum dorsiflexion position). Calculating the PWD-ATIA relationship during plantarflexion (maximum dorsiflexion to maximum plantarflexion) showed a slight difference in PWD during ankle plantarflexion compared to dorsiflexion (Figure 4.12). This 'hysteresis' was found in 4 out of 5 volunteers, but was not consistent in shape. The volunteer with no hysteresis (Figure 4.13) has a maximum PWSD range of 4mm, which is not large enough to detect hysteresis in addition to the flat CST found in this volunteer's CST. As PW's motion seems to 'lag' during dorsiflexion and 'lead' during plantarflexion, it can be speculated that PW hysteresis assists in load bearing within the AT enthesis organ. As this study used a low refresh rate US video imaging, this provided a limited number of images to conclude if hysteresis is valid. Hence, further studying was required to support the findings of this test.

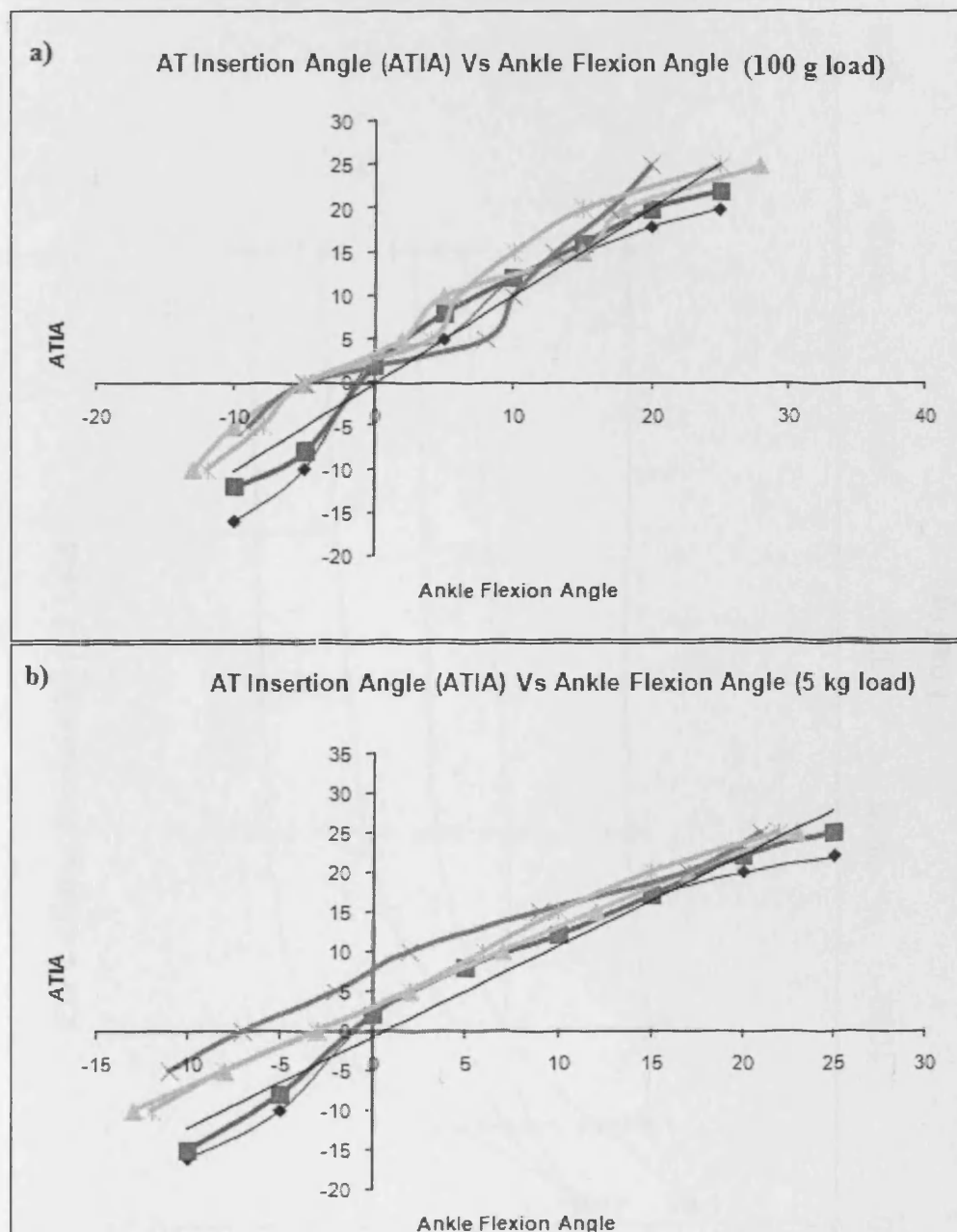


Figure 4.5: (a) Illustrating the non-linear relationship between ATIA and ankle flexion angle (AFA) under 100 g ankle load in the 5 volunteers. This relationship becomes more linear as the ankle load is increased to 5 kg (b). AFA is observed to increase at higher rate compared to ATIA during ankle plantarflexion position.

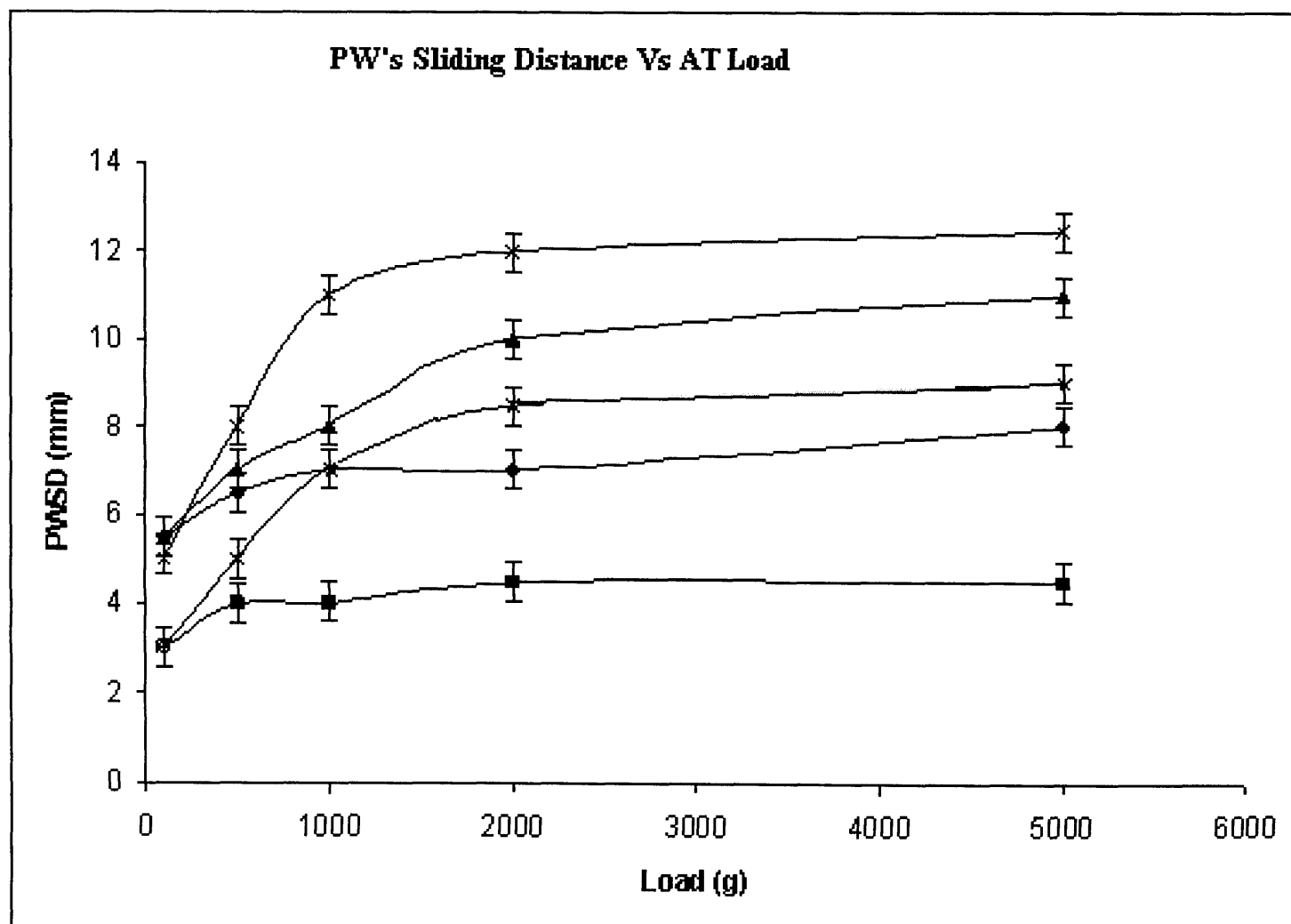


Figure 4.6: At 100g plantarflexion load, PWSD ranged from (2.5 – 5.5 mm). PWSD increases and reaches the maximum range (4 – 12 mm when plantarflexion load is 5 kg).

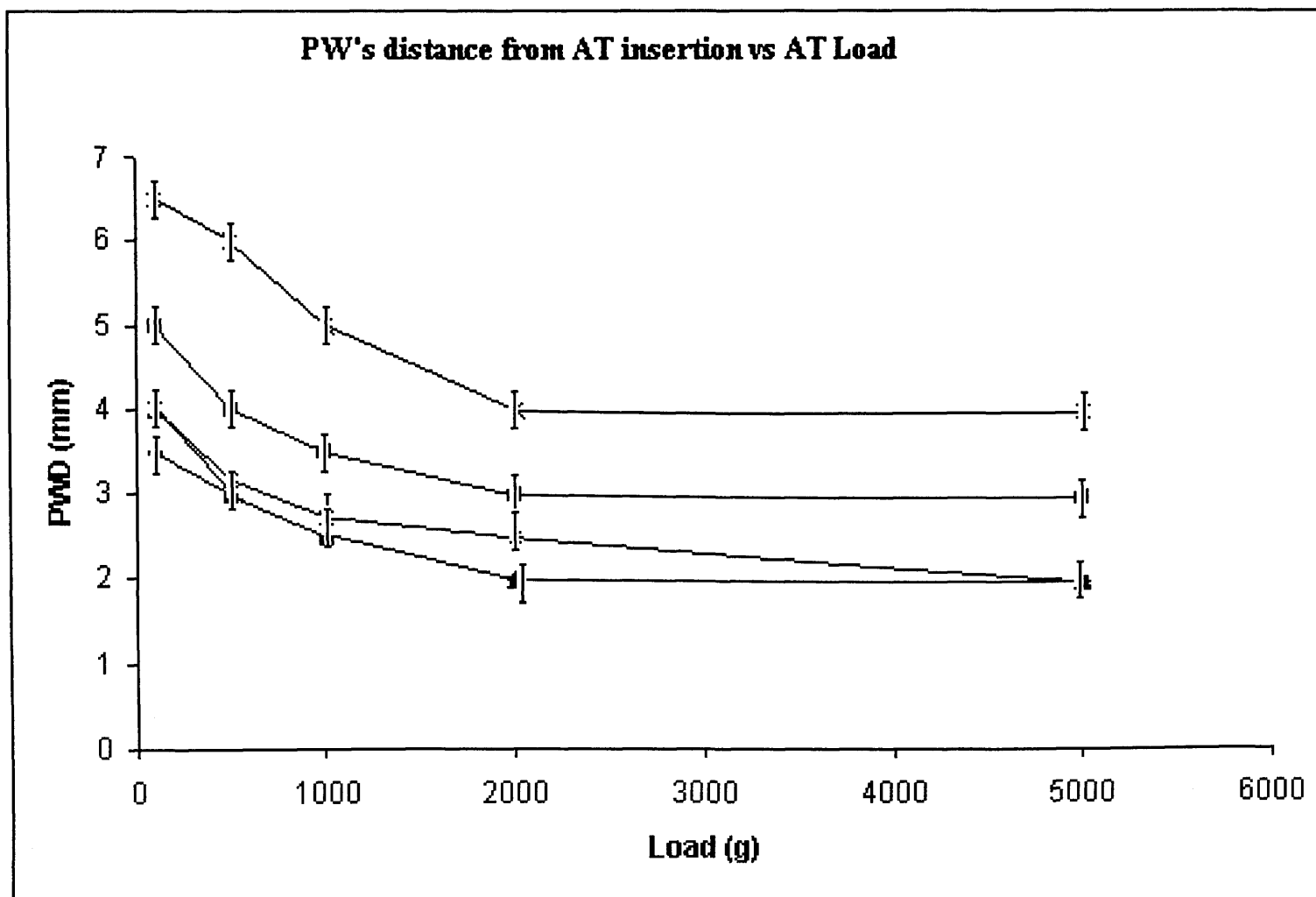


Figure 4.7: At 100g plantarflexion load, the distance between PW tip and most distal point of AT insertion (PWD) ranged from 3.5 – 6.5 mm. PWD decreases exponentially and reaches within 2 – 4 mm when plantarflexion load is 5kg.

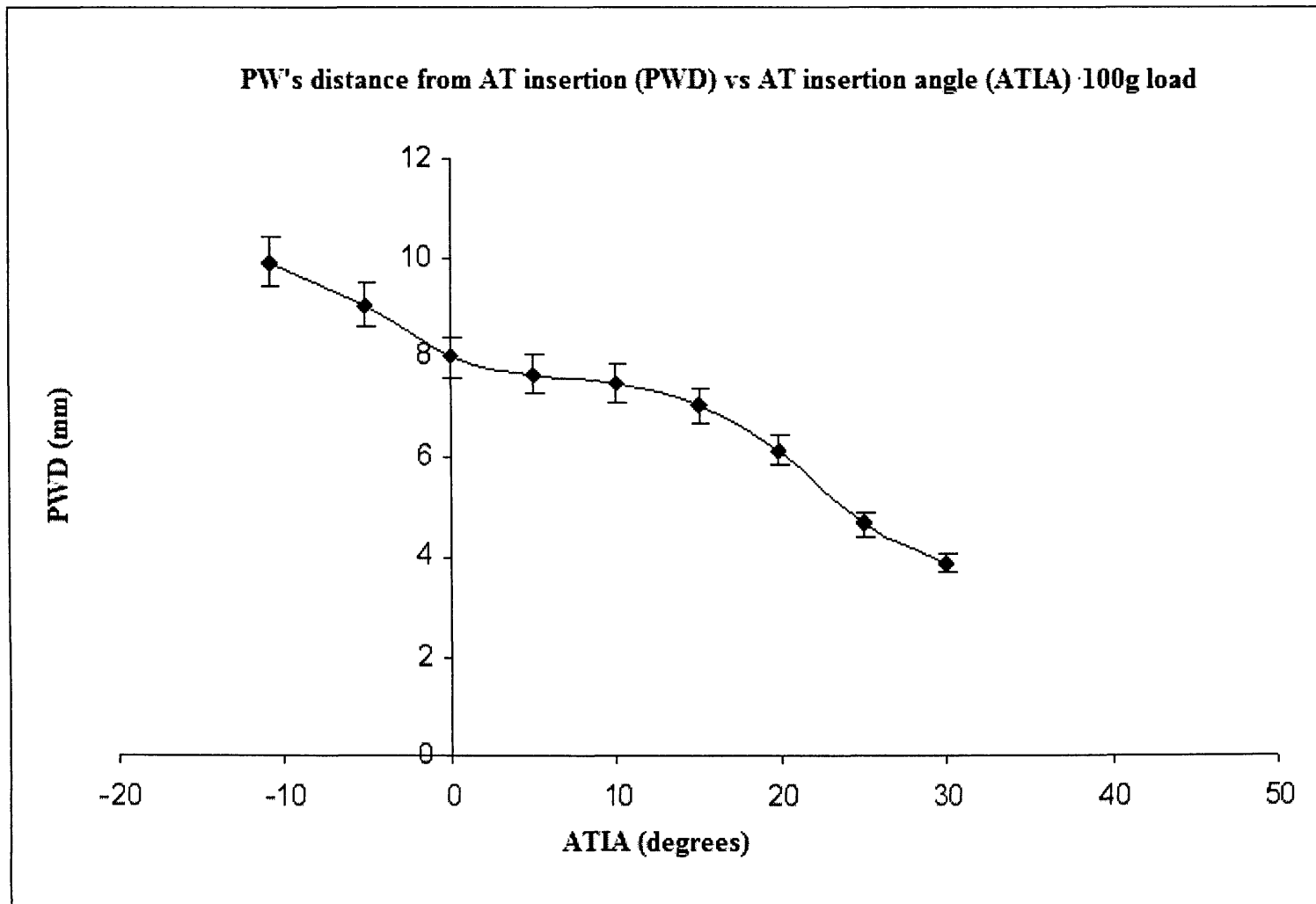


Figure 4.8: A result graph of one volunteer showing the relationship between PWD and ATIA when plantarflexion load = 100 g.

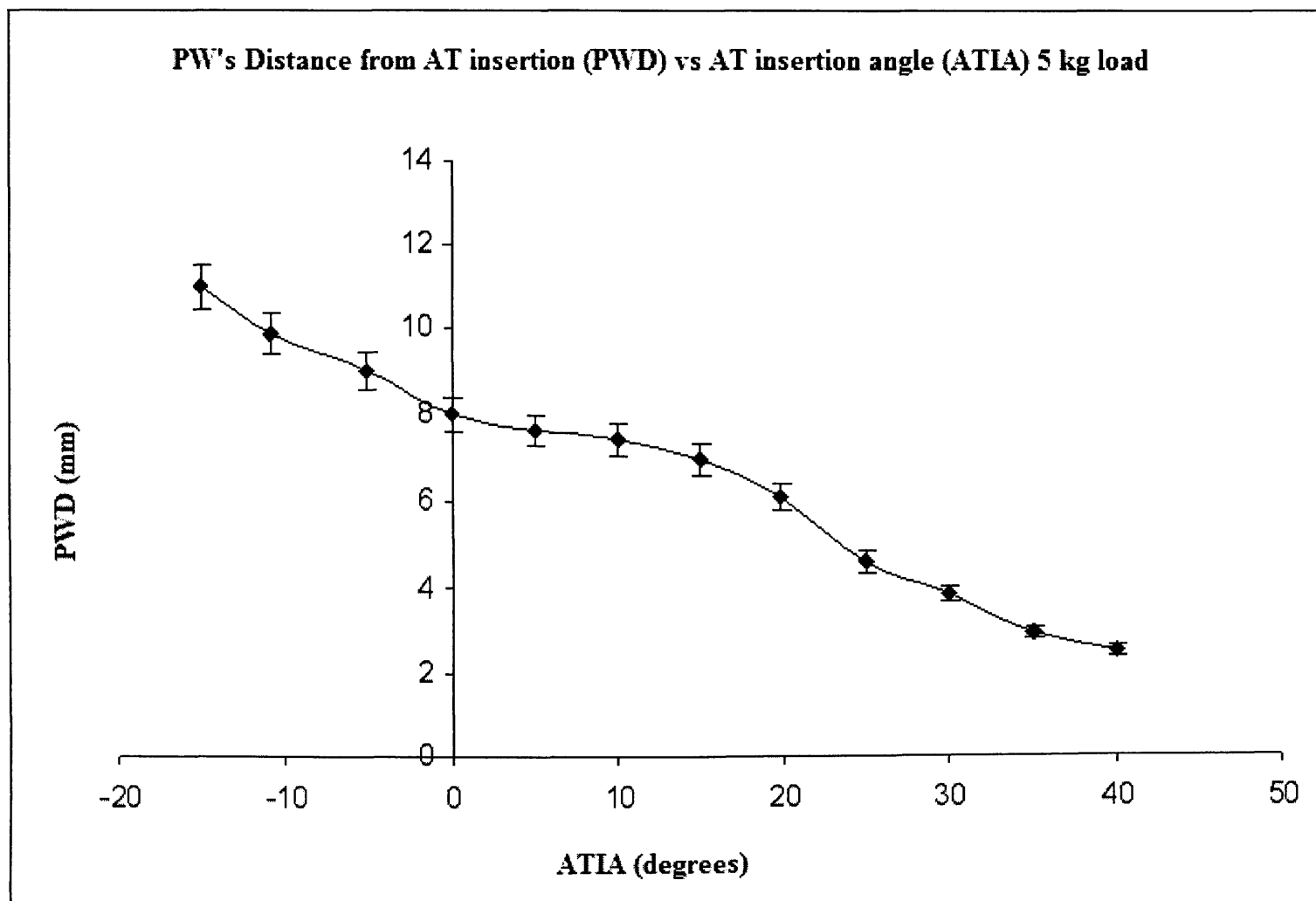
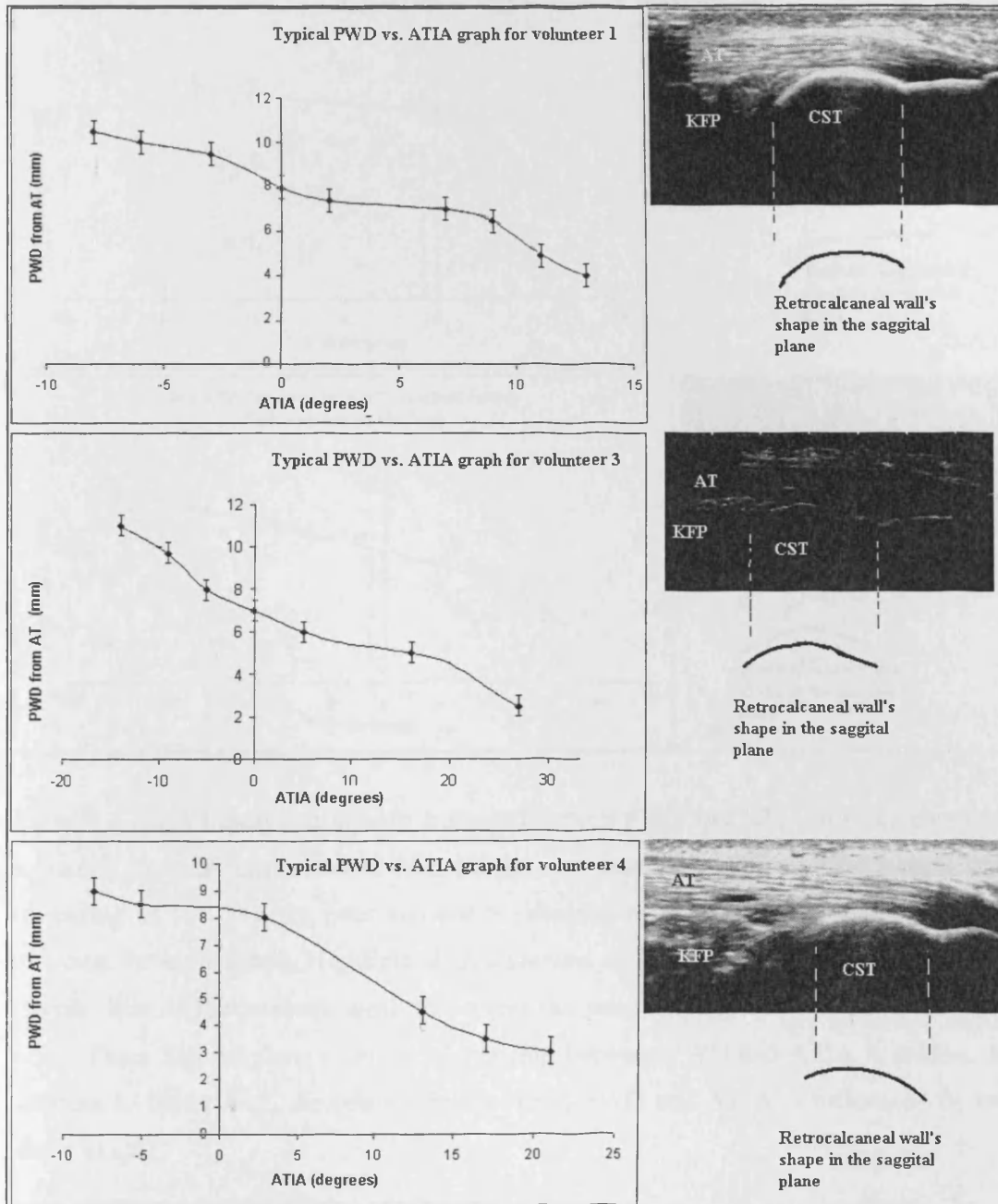
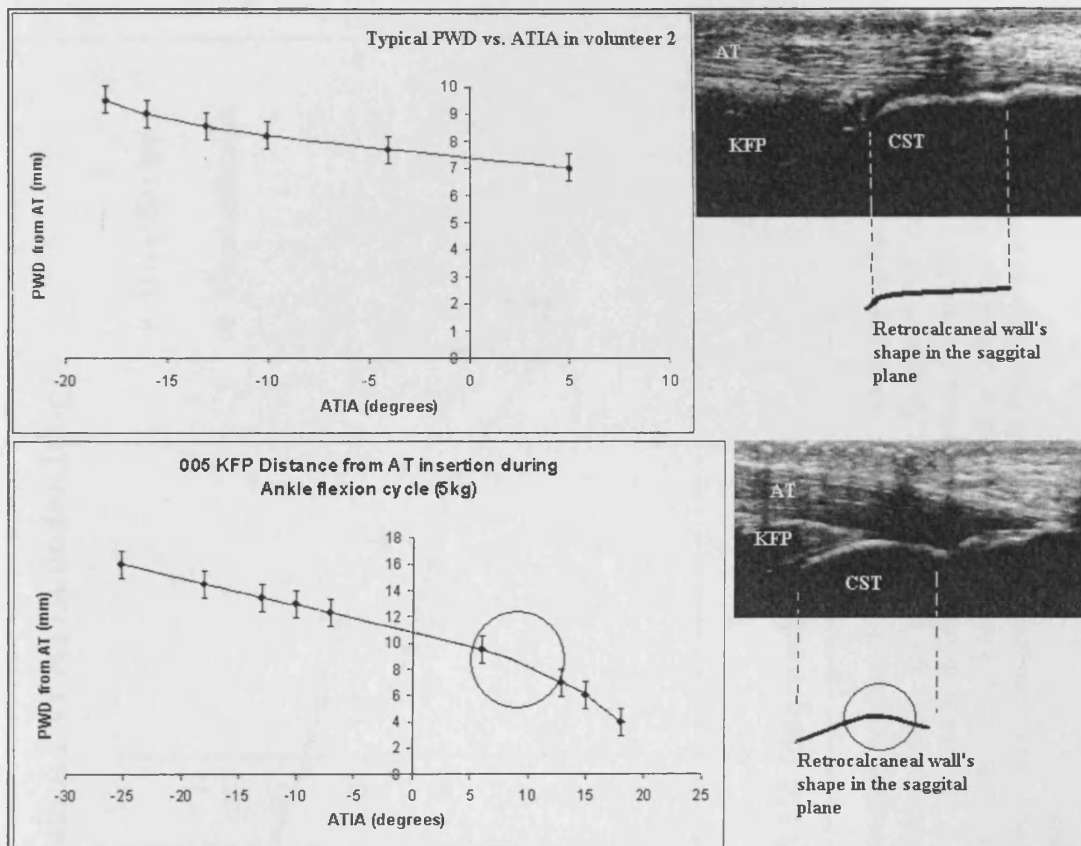


Figure 4.9: A result graph of the same volunteer as figure 4.3.2.C, the relationship between PWD and ATIA when plantarflexion load = 5 kg. It was observed that the curvature of the graph did not change, except ATIA appeared to reach higher ranges.



Figures 4.10: Graphs comparing the relationship between PWD and ATIA, with respect to the shapes of volunteers' CST. US images illustrate the shape of retrocalcaneal wall (the wall of CST upon which PW slides) in three volunteers is single dome shaped. The relationship between PWD and ATIA found is non-linear and reflected the dome shape.



Figures 4.11: A Linear relationship is found between PWD and ATIA in volunteers with a straight looking retrocalcaneal wall (**above**). A volunteer with a retrocalcaneal wall consisting of two straight lines showed a relationship between PWD and ATIA that reflected the same shape. Highlighted area showed as PW reached the point where the straight line of the retrocalcaneal wall meet, its pace increased towards AT insertion point. These Figures show a strong relationship between PWD and ATIA is evident. In addition to figure 4.12, the relationship between PWD and ATIA is influenced by the shape of CST.

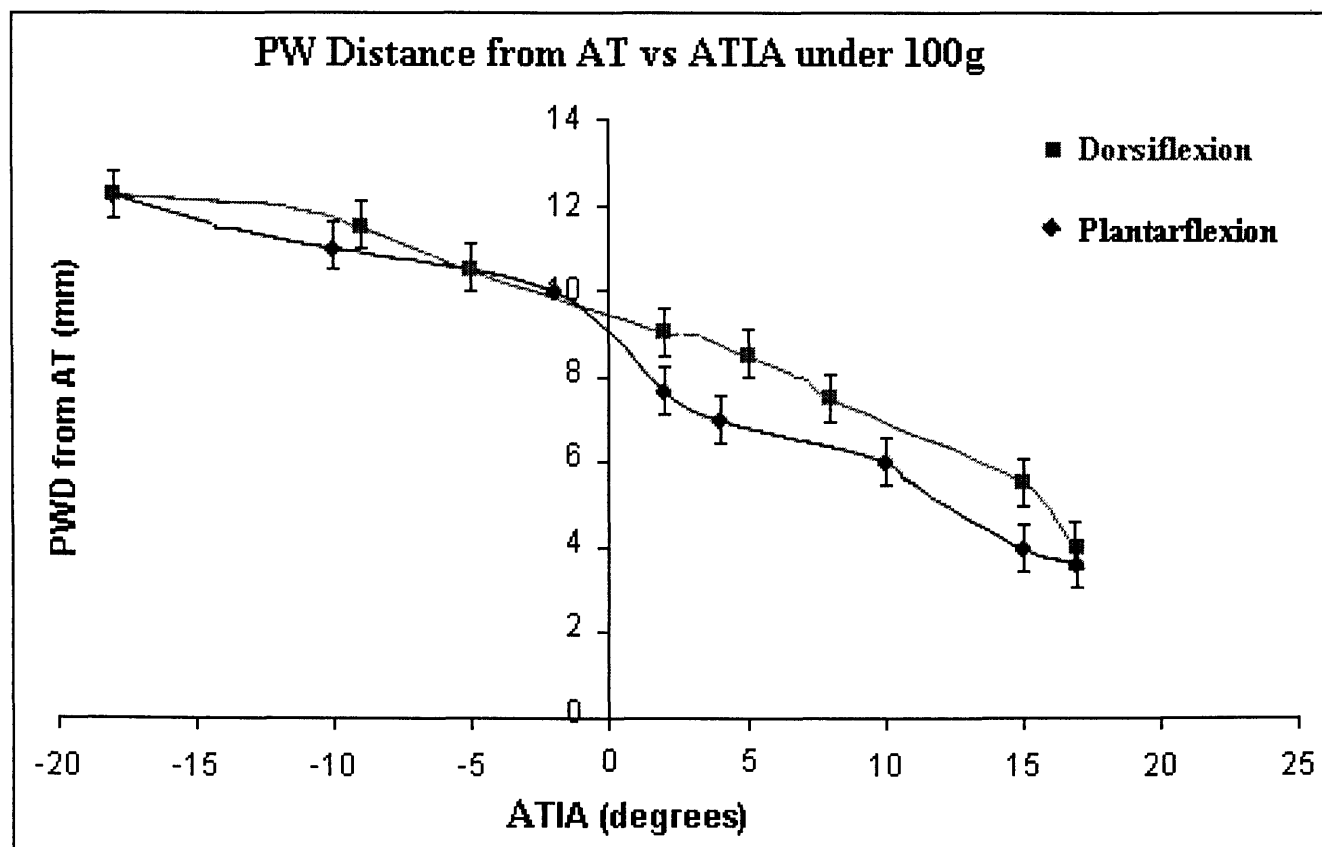


Figure 4.12: A graph comparing the relation between PWD and ATIA when the ankle flexes in the plantarflexion direction through its full flexion range, against dorsiflexion. At certain AT insertion angles (in this graph at angle $+15^\circ$ and 3°), PW can reach different distances when the ankle is flexed in the plantarflexion direction than the dorsiflexion direction. This change was not conclusive at this point to be valid as the US scanner was set to produce video images at a low refresh rate. This provided a limited number of images for hysteresis assessment.

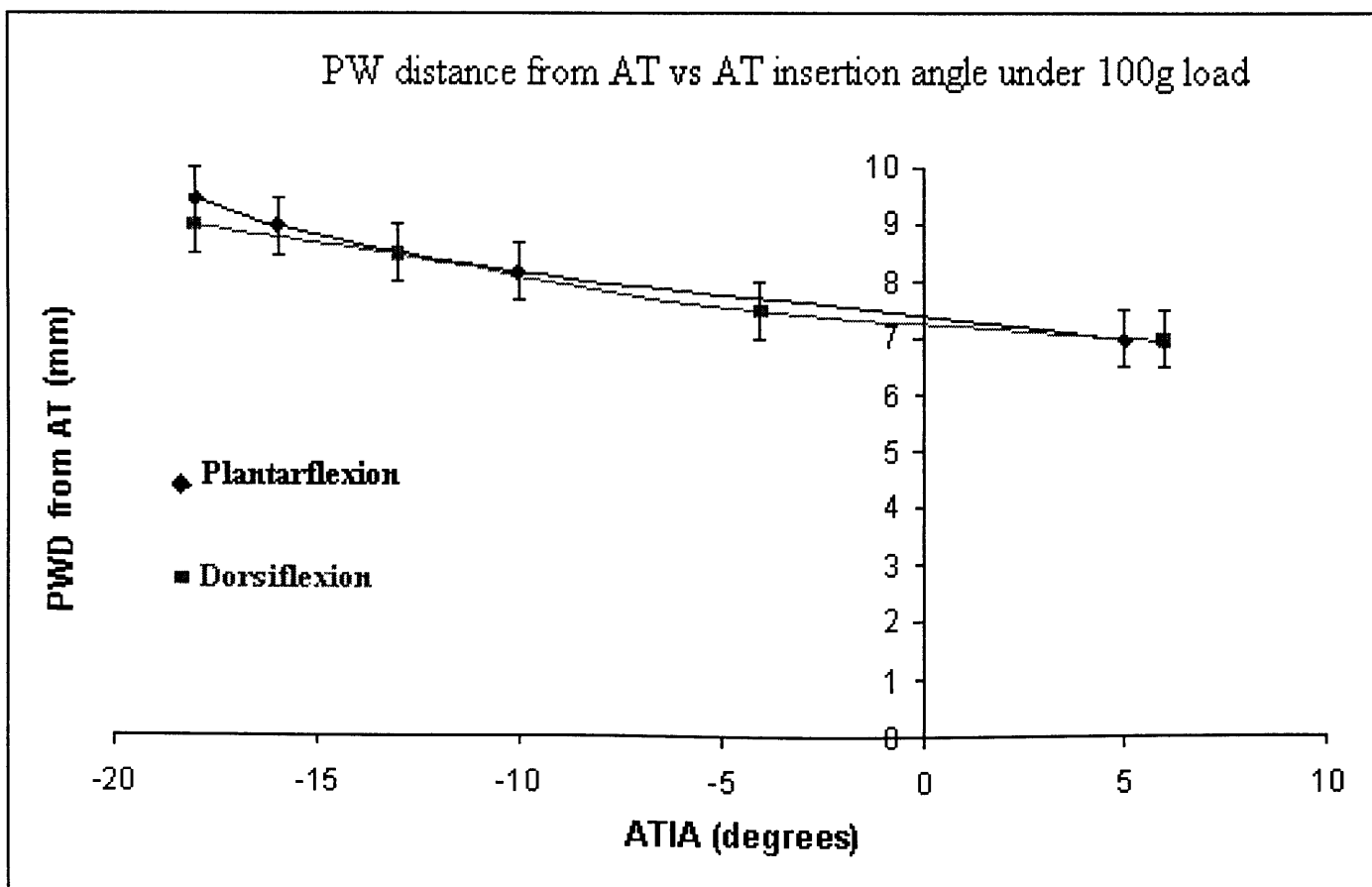


Figure 4.13: A graph showing no hysteresis in one volunteer. It was suggested that as this volunteer's retrocalcaneal wall has a straight shape. The maximum PW slid between 7 and 9.5 mm from AT insertion point. As PWSD is low, it was thought to be difficult to find an obvious PW hysteresis.

2.16 Discussion

Looking into the US images, the relationship between ATIA and AFA was ankle load dependant, suggesting a relationship between ATIA and ankle load. During the first study for this PhD (Chapter 3) it was shown that ATIA changed during passive ankle flexion (no load or tension on AT). Therefore, as load increases, the tension on AT increases, reducing its curvature (and bends) causing it to have a straight shape. This leads the relationship between ATIA and AFA to be linear at high loads (2 kg or greater).

It was also observed across all volunteers that PW only changes its location when ATIA changes. Figures 4.8 & 4.9 showed no obvious variance in PWD as ankle load increases. ATIA was observed to increase with increasing load. This suggests that the location of PW, and hence motion, is a function of ATIA rather than ankle load, since PWD changed as a result of increasing ATIA, which increased with load until it reaches the maximum ATIA range.

The increase in PWSD with load may be caused by the reduction of AT bends with increasing load, which can also help us understand the increase in ATIA with increasing ankle load. Further research is required to study the AT bending.

The shape of the relationship between PWSD and ankle flexion angle seems to be reflected by the shape of the individual's CST shape (Figures 4.10 & 4.11). In volunteers with a single dome shaped retrocalcaneal wall, PWD seemed to have a non-linear relationship with ATIA reflecting the dome shape or CST wall, suggesting PW slides at different speeds within AT enthesis organ depending on the shape of CST. In one volunteer with a straight shaped retrocalcaneal wall, PWD had an evidently linear relationship with ATIA. The fifth volunteer has a retrocalcaneal wall, the shape of which has two straight lines joined at a prominent point (Figure 4.13). PW for this volunteer slid at 2 constant speeds, which changed at the prominent point. This shows that PW's motion is also a function of the shape of CST, which changes the space provided for PW's tip to protrude into.

PW hysteresis was observed in 4 volunteers. The only one with no obvious hysteresis observed is the one with a straight shaped CST wall. In addition this volunteer's PWSD is 4mm and the ATIA range was 23° , which is not large enough to detect any hysteresis at the current settings of US scans. Since the refresh rate of the US scanner was set to a low rate (10 fps), not enough readings were produced to conclude whether the hysteresis is valid at this stage. Therefore, a further study was carried out with higher refresh rate settings to examine PW hysteresis, which is detailed in the next chapter.

2.17 Conclusions

- PWSD increases with increasing ankle load, until load reaches 2 kg
- PWD decreases with increasing ankle load until load reaches 2 kg
- PWD is influenced by AT insertion angle
- The relationship between PWD and ATIA may be influenced by the shape of the individual's retrocalcaneal walls
- Hysteresis was found between PWD and ATIA. However, further studies are required to evaluate the nature of this hysteresis. This can assist in examining PW's load bearing function as it can indicate an increase in the lever arm of AT during ankle dorsiflexion

2.18 Next Chapter

Chapter 5 details the final test of this research, looking into the load bearing property of KFP. As in-vitro testing indicated load bearing as a possible functions of KFP's, testing was carried out to assess the in-vivo load bearing. The next test focused on testing the area and volume change of KFP during ankle flexion, as well as examining PW's hysteresis found in this test (chapter 4).

Chapter 5

Kager's Fat Pad's In-Vivo Load Bearing

2.19 Introduction

One of the most important hypothesized biomechanical functions of KFP within the AT enthesis organ is the possibility of serving to assist in load bearing [4,20,36], by reducing the load between AT and CST, and protecting AT enthesis by reducing wear and tear [15,20,36]. In-vitro studies suggested KFP provides a reduction in loading [1,16]. This was supported by the existence of a fibrous ending of PW, as fibrous tissues are developed to resist external loading [1, 26-29]. Since this level of load bearing is similar to that of the knee meniscus (between 30 and 70% of the load on the knee joint) [16,45-51], PW hypothetically serves a critical biomechanical advantage to AT enthesis organ (Appendix I for literature review on knee menisci).

In-vivo load bearing functionality was previously refuted by comparing KFP's intrusion into the subtendinous region of AT between the three ankle flexions positions (Plantarflexion, Neutral & Dorsiflexion position) [16], as the synovial fluid surrounding PW appeared to cause PW to slide freely out of the bursal space during plantarflexion. However, such a study only compared PW distances against 3 ankle flexions positions using still images, which did not examine the possibility of real-time load bearing between the three flexion positions. Furthermore, the hysteresis found between PW and ATIA in the previous test (Chapter 4) suggests PW could dynamically reduce the impact between AT and CST during dorsiflexion. In addition, the fibrosis of PW's tip indicates friction between PW's tip and AT enthesis walls. This study is aimed to examine PW's load bearing properties by studying the hysteresis using ultrasound imaging as well as KFP's area and volume change using MR imaging, as was previously used for knee meniscus in-vivo load bearing evaluation [46,48,52,53]. In Addition, PW's thickness (PWT) was monitored

2.20PW Hysteresis

During the previous experiment (Chapter 4) a hysteresis was observed from US images between PWD and ATIA. As illustrated in Figure 5.1, PW can be at different distances from AT insertion point during dorsiflexion, compared to during plantarflexion within certain regions of ATIA. In the example illustrated, PWD is 8mm during plantarflexion, while during dorsiflexion PWD is 10mm, although both measurements were taken at $ATIA = 6^\circ$. It can be speculated that as literature review showed KFP has load bearing properties during in-vitro testing. PW's hysteresis can lead to speculations that it offers in-vivo load bearing during ankle flexion as PW's tip seemed to 'lag' during dorsiflexion. This may cause momentary dynamic load bearing. Previous tests were carried out using low refresh rate US video recording settings [1,16,36]. It was hence seen as essential to increase the refresh rate to examine the hysteresis to help determine KFP load bearing properties.

Prior to testing, a number of external factors were considered that may cause the hysteresis;

- **Doppler Effect:** was considered as a cause of the differences in readings between when PW travels with the direction of US waves, and against it. However, the US machine was always set to collect still images (video files are a collective of still images) as opposed to Doppler mode (comparing consecutive images). In addition, a pilot study (Section 4.2.4.3), focused on testing effect of ankle flexion speed on PW motion showed no change in PW hysteresis with changing flexion speed, proving that it is not a Doppler effect.
- **US Transducer Location & Pressure:** as CST has a non-uniform shape and curve [16,44] changing the transducer's location during scanning may change results depending on the shape of CST. A previous study (section 3.2.3.2) showed that using a skin marker to highlight the midline ensured consistency in results. The same pilot study also examined the influence of pressure applied on AT externally during scanning on PWD. PW tip's location is not affected by the pressure applied by the US transducer

against AT unless a physically noticeable amount of force is applied (the volunteer feels a noticeable discomfort before results change). In addition, the US transducer is placed with minimum force against AT, allowing the ankle to flex unrestricted during testing. Also, as repeatability tests showed consistent results (Section 3.2.3.1), human errors are not a likely cause of PW hysteresis.

- **AT Thickness:** previous studies showed that AT thickness changes in the sagittal plane, decreasing during eccentric calf exercise greater than during concentric calf exercise [54]. On the other hand, no real-time changes were reported in AT thickness between plantarflexion and dorsiflexion. A pilot study was carried, as reported later (section 5.2.1.2.1) that measured the thickness of AT in 3 different locations during ankle flexion. Results showed no obvious change in AT thickness between ankle plantarflexion and dorsiflexion.
- **Ankle Loading:** this research showed that load affects PWSD and PWD (Chapters 3 & 4). Results from Chapter 3 showed that hysteresis gap increased with load in 1 volunteer, decreased with load in 1 volunteer, stayed unchanged in 2 volunteers, and one volunteer that showed no hysteresis showed unchanged results with load. As previous US examinations lacked the high refresh rates, this study looks into the effects of plantarflexion loading on PW hysteresis.
- **AT bending:** described in section 5.3, AT bending was observed in a number of images during active ankle flexion. As no detailed studies were available about AT bending during ankle flexion AT bending was also examined in this study.

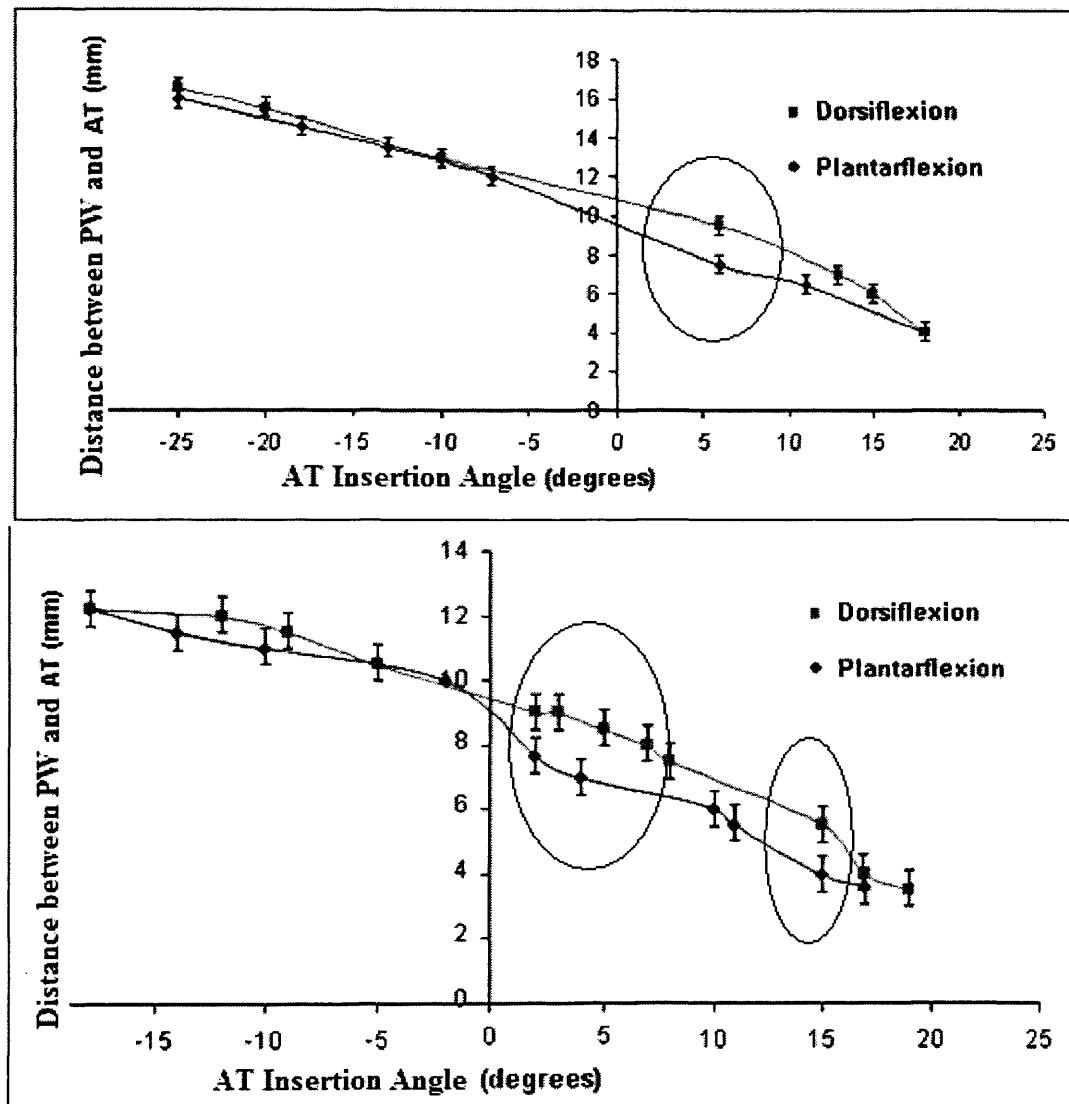


Figure 5.1: Typical hysteresis graphs drawing the distance between PW's tip and AT insertion point (PWD) against maximum range of AT insertions angle (ATIA). In certain flexion angle regions (circles), PW hysteresis was observed.

2.20.1 Materials and Methods

5.2.1.1 Ultrasound Examination of PW Hysteresis

The same dynamic US machine as used previously in this PhD (Toshiba Aplio - with a linear transducer operating at 12 MHz) was used to scan KFP during ankle flexion. In order to produce higher resolution graphs representing the 'hysteresis' the US scanner was set up to acquire video clips at 36 fps instead of 10 fps (frames per second) as previously acquired images were sufficient to produce a clear graph. Prominent landmarks were used to calculate PWD and ATIA. The most proximal point of AT insertion point and PW's tip were used as landmarks to measure the PWD. The AT fibre line and a line drawn on the most prominent parts of CST were located to calculate ATIA as used previously (Figures 4.1 & 4.2).

Pilot Study

As this method was used for the previous testing (Chapter 4), evaluating the method was not necessary.

2.20.1.1.1 AT Thickness Variation during Ankle Flexion

Previous studies showed that AT thickness changes under constant usage in the long run [54,55]. No studies were found examining the real-time changes in AT thickness during ankle flexion. As real-time changes in AT thickness may influence PW hysteresis, this pilot study measured AT thickness in 3 different locations (at the AT insertion point, 1cm superior to AT insertion point and 2 cm superior to AT insertion point) using US data from 5 volunteers. Results illustrated in Figure 5.2 showed a maximum AT thickness change of 0.5 mm in 2 volunteers. This result is within the error or 0.5mm which means that this study could not find any change in AT thickness during ankle flexion.

Even when considering the standard deviation for measuring results of ATIA, PWD and AT thickness, PW hysteresis was still valid from the previous test's results.

2.20.1.2 Ultrasound Examination Protocol

The hindfoot of the same 5 volunteers (same volunteers for MRI examination, section 5.4.1) were scanned in the sagittal plane using dynamic US imaging while flexing their ankles repeatedly in the loading rig used for the previous test (Section 4.2.2). The ankles were actively flexed between plantarflexion and dorsiflexion positions repeatedly against plantarflexion loads of 0, 100 g, 500 g, 1 kg, 2 kg and 5 kg. The video refresh rate was set to its maximum (36 fps). Still images were extracted from the video files acquired using VirtualDub software for offline processing to measure PWD and ATIA using obvious and prominent landmarks as used in section 4.2.1.

2.20.2 Volunteer Preparation & Selection

This study only accepted healthy volunteers who had no history of ankle surgeries or any serious injuries. MRI testing is not recommended for a number of groups including the pregnant, the tattooed using metal composite ink and anyone with and implanted devices, prostheses, or fixations (nails and screws) (a full check list for MRI scanning is attached in Appendix IV). Since this test acquired volunteer selection for both MRI and US scans, checks were carried out to eliminate volunteers who cannot be scanned using MRI.

2.20.3 Statistical Analysis

Statistical analysis of the data was performed using the t test (two-tailed) and Wilcoxon test. A significance level of 0.05 was adopted.

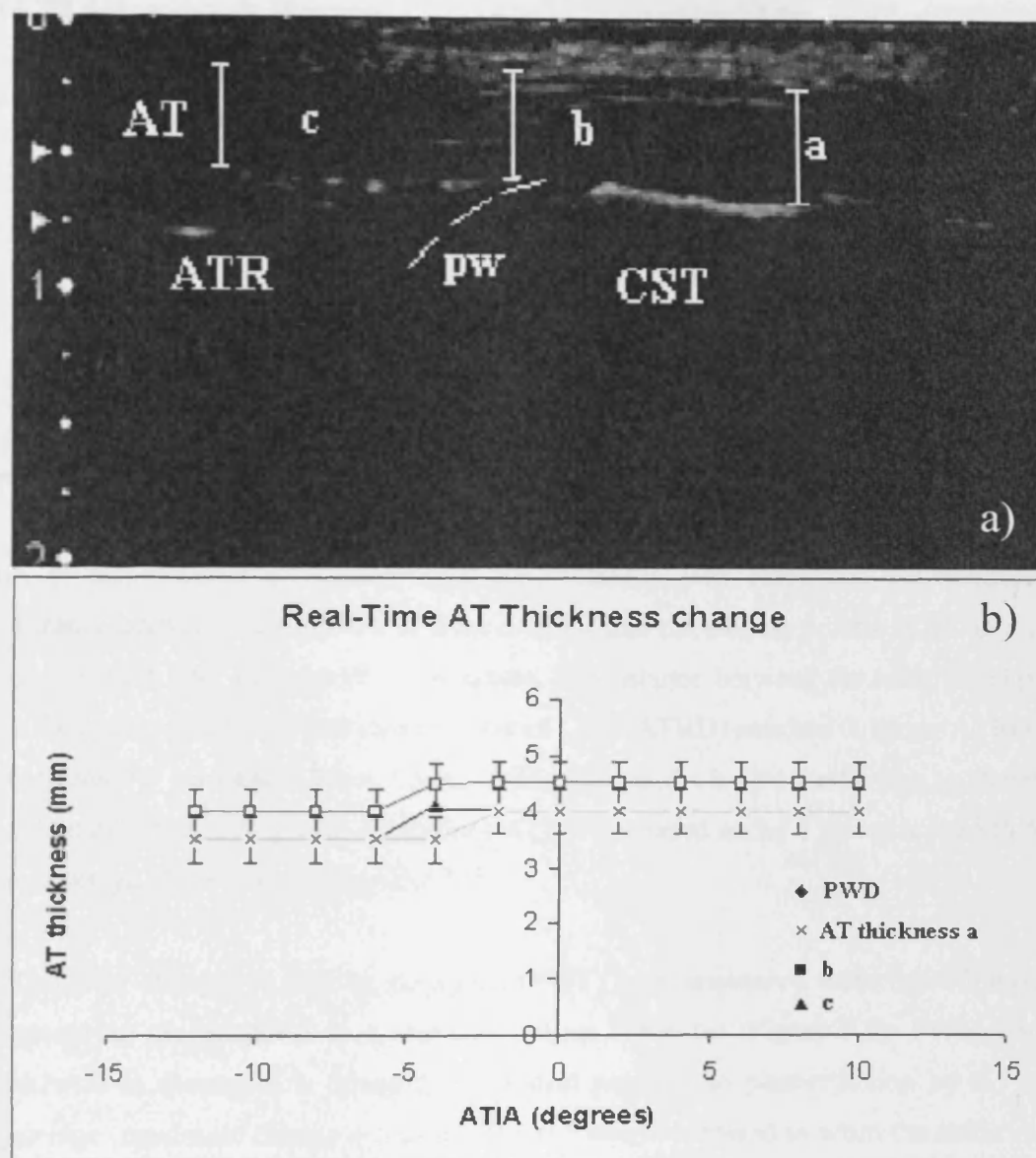


Figure 5.2: AT thickness was measured in 3 different sites (a) at the most proximal point of AT insertion (a), 1 cm away from a (b), and 2 cm away from a (c). (b) results showed AT thickness was uniform. A 0.5 mm maximum change was observed in 2 volunteers. 3 volunteers showed no obvious change in AT thickness. Dorsiflexion and plantarflexion results were identical. As results are within error limits, it can be said that no AT thickness changes were observed.

2.20.4 Hysteresis Results

Results showed that as ATIA reaches either of its limits (maximum plantarflexion & maximum dorsiflexion positions), PW slows down (Figure 5.3). In other words, PW's tip sliding pace changes during ankle flexion. As the ankle reaches its maximum plantarflexion or dorsiflexion positions, sliding speed of PW is significantly reduced. Results also showed hysteresis evident in 4 volunteers out of 5 (Figure 5.4). PW hysteresis was typically found during the plantarflexion region of ATIA. The volunteer with no PW hysteresis had a maximum PWSD of 4mm and ATIA range of 30° and a flat shaped CST, which made detecting any hysteresis difficult. It was also noted that the 4 volunteers with PW hysteresis had a fibrosis ending to the PW tip (Figure 5.5).

ATR displacement (ATRD) during ankle flexion was calculated by measuring the distance between the most distal point of ATR and the closest point of CST in a straight line (Figure 5.6). In 2 out of 5 volunteers, the distance between the most distal point of ATR attachment to AT and closest point of CST (ATRD) reached 0. Mean ATRD varied between 1.5 mm and 4.5mm during ankle flexion cycle (plantarflexion to dorsiflexion and back) under 100 g load. Maximum ATRD increased under 5 kg ankle load to 5.5 mm on average (SD = 1 mm) (Figure 5.7).

Real time changes in PW tip thickness (PWT) were measured from the US images by measuring the thickness at 4 mm away from PW's tip (Figure 5.8). PWT seemed to increase as the ankle is flexed from neutral position to plantarflexion by 0.5 mm on average (maximum change = 1 mm, SD = 0.5 mm) compared to when the ankle is flexed from plantarflexion to neutral position.

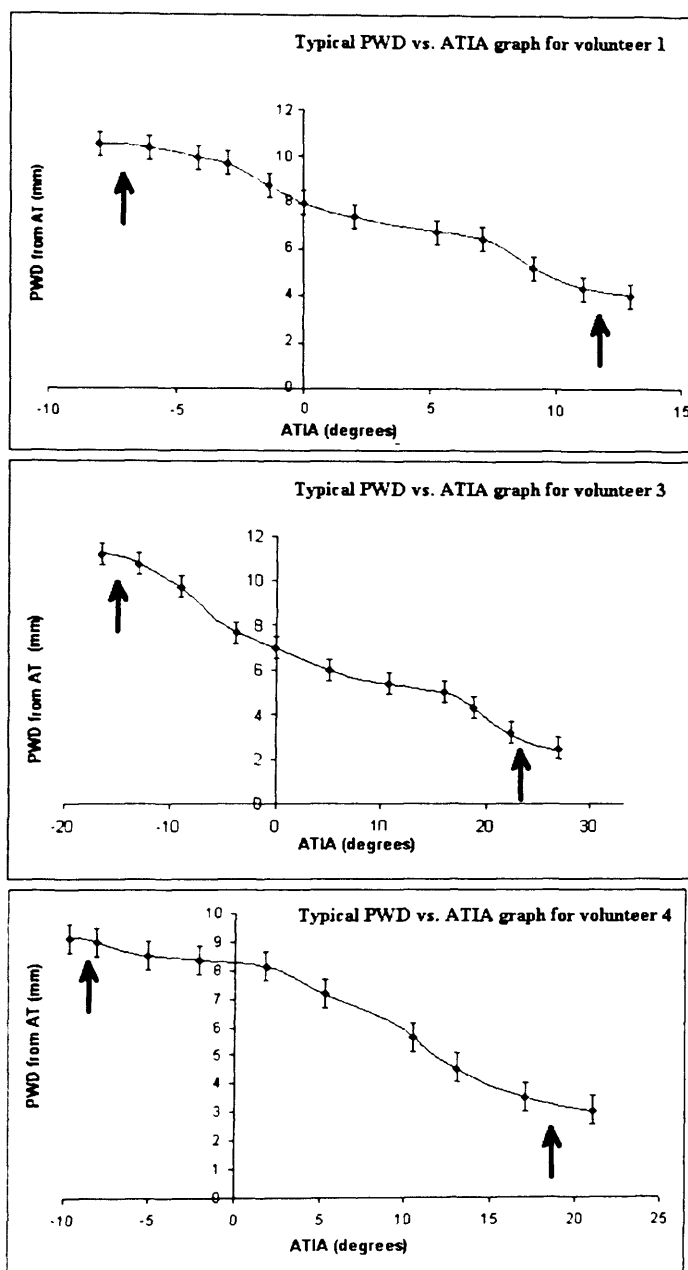


Figure 5.3: Graphs showing the relationship between ATIA and the distance between PW's tip and the most proximal point of AT in 3 different volunteers. As ATIA reaches either of its maximum angle limits in every individual (arrows), PWD value tends to reach its maximum limits in distances. PW's tip slides at different paces during ankle flexion.

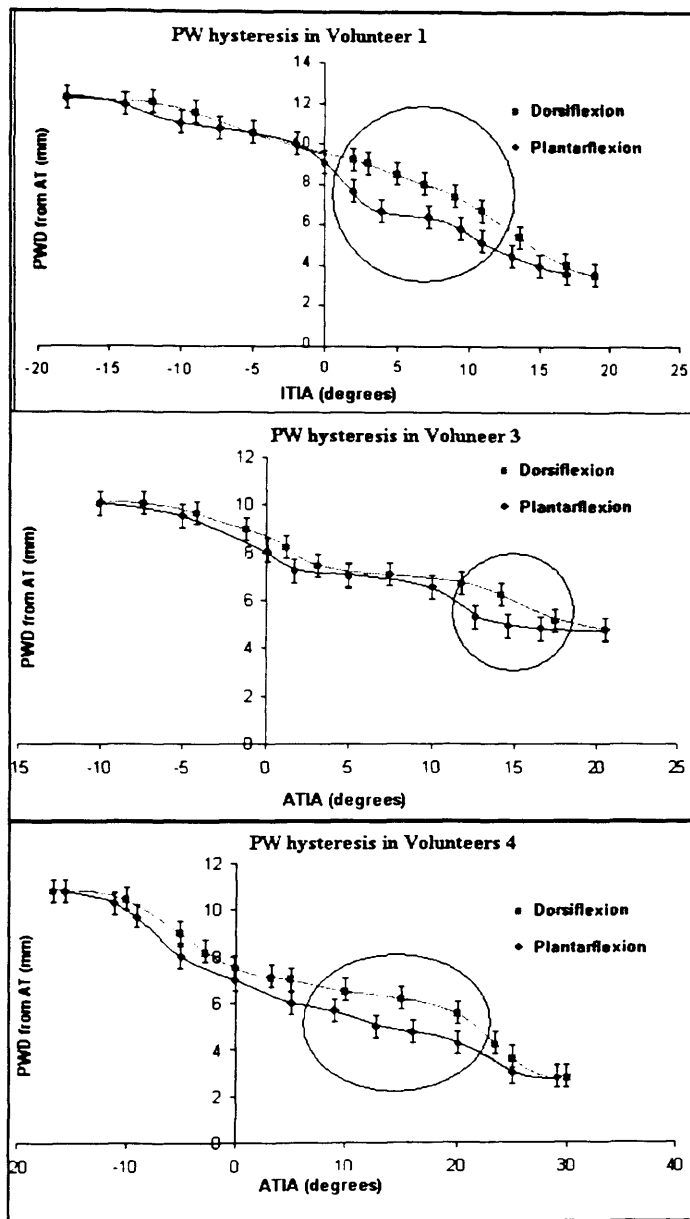


Figure 5.4: Results graphs of 3 volunteers illustrating PW hysteresis. Hysteresis greater than error bars is consistent mainly in the plantarflexion region when PW's tip is close to AT insertion

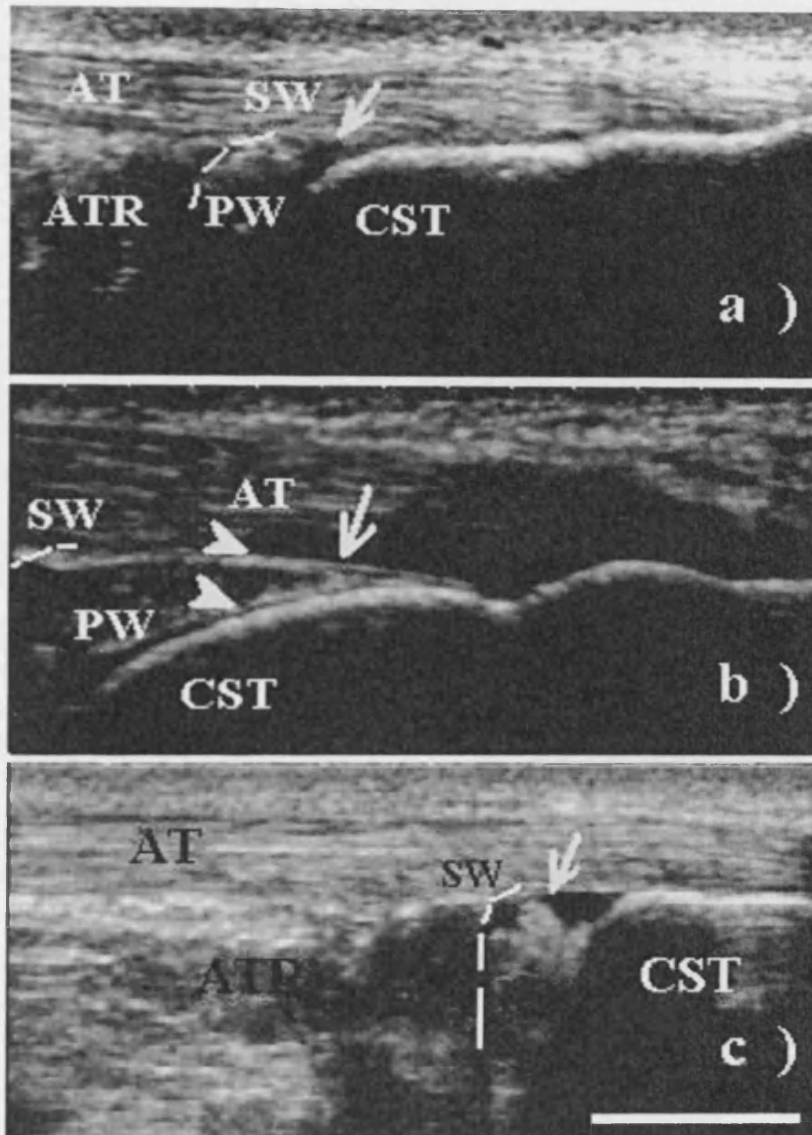


Figure 5.5: Saggital US images taken showing the fibrous tip of PW. Three volunteers shown for example purposes (a, b & c). In all cases a fibrosis can be observed (arrows) where PW wall thickening can be observed. In one volunteer, fibrous lining was observed along PW tip's walls (arrowheads). AT = Achilles tendon, ATR = Achilles tendon related fat pad, PW = protruding wedge of Kager's fat pad, SW = synovial wall separating ATR from PW, CST = Calcaneal Superior Tuberosity, Scale bar = 1 cm.

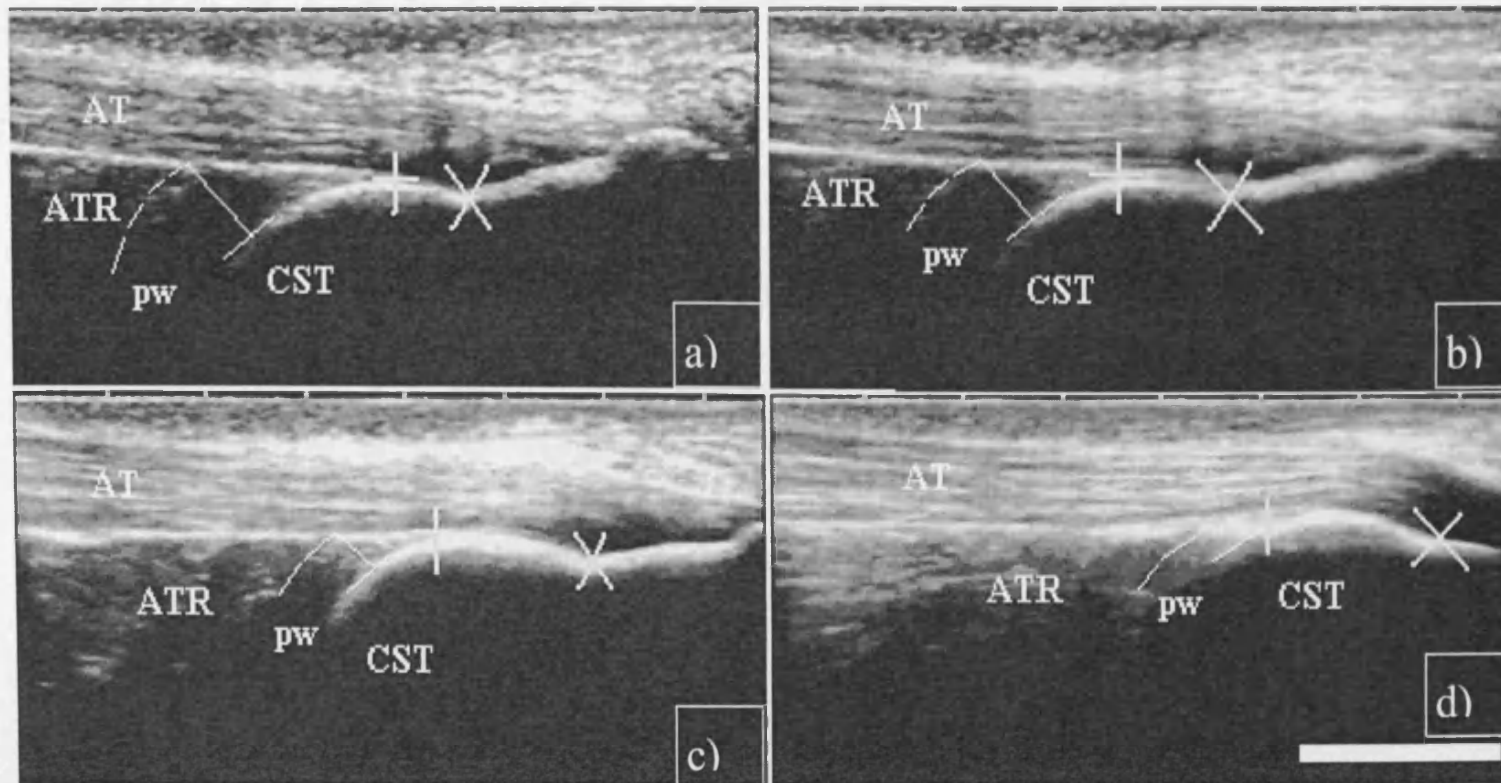


Figure 5.6: ATR displacement (ATRD) during ankle flexion was calculated by measuring the distance between the most distal point of ATR and the closest point of CST in a straight line. ATRD was observed to decrease as ankle flexes from plantarflexion to dorsiflexion (a-d). + = PW's tip. X = AT insertion's most proximal point, AT = Achilles tendon, pw = protruding wedge of KFP, Scale bar = 1 cm

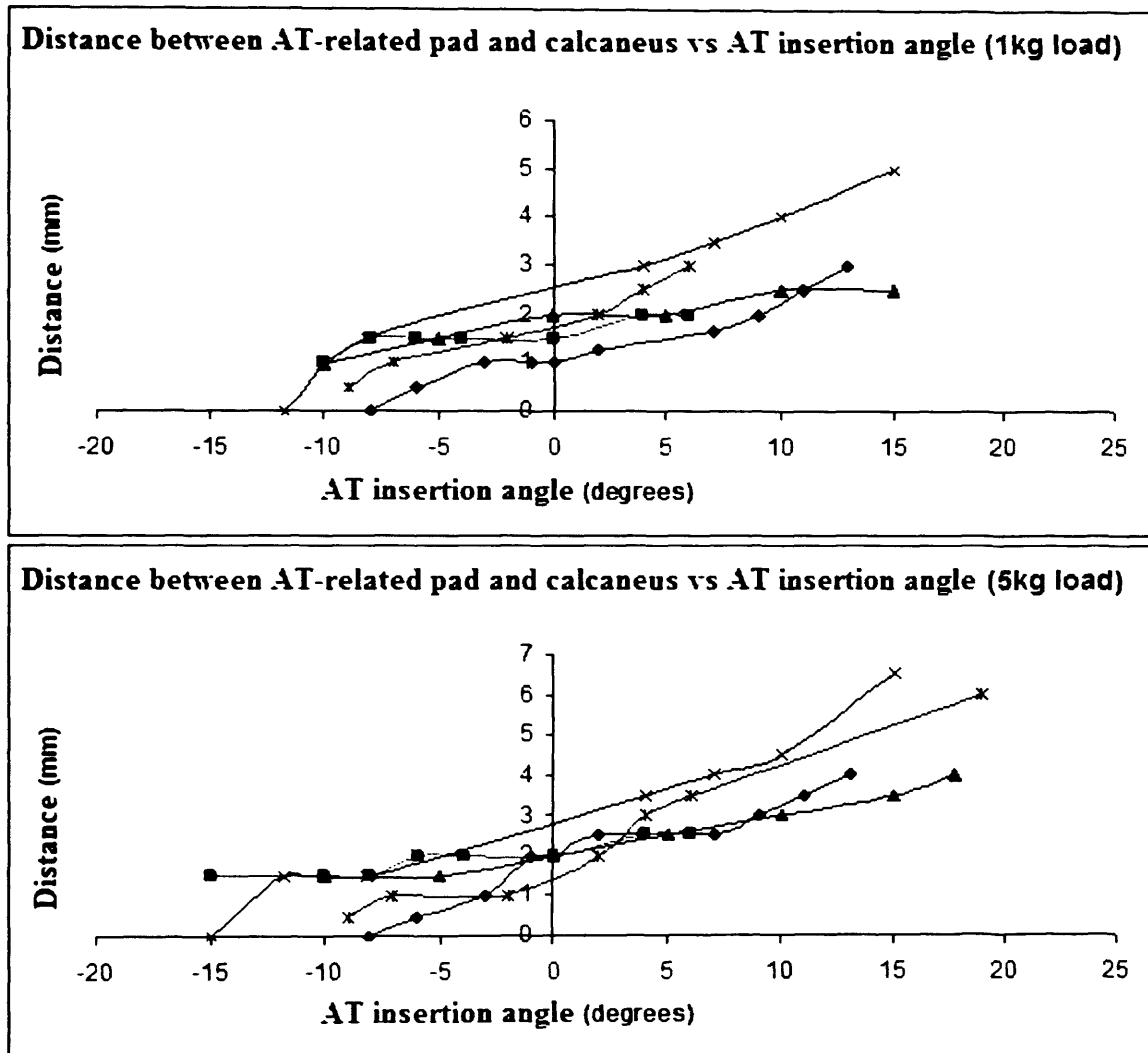


Figure 5.7: In 2 out of 5 volunteers, the distance between the most distal point of ATR attachment to AT and closest point of CST (ATRD) reached 0. Mean ATRD varied between 1.5 mm and 4.5 mm during ankle flexion cycle (plantarflexion to dorsiflexion and back) under 100 g load. Maximum ATRD increased under 5 kg ankle load to 5.5 mm on average (SD = 1 mm).

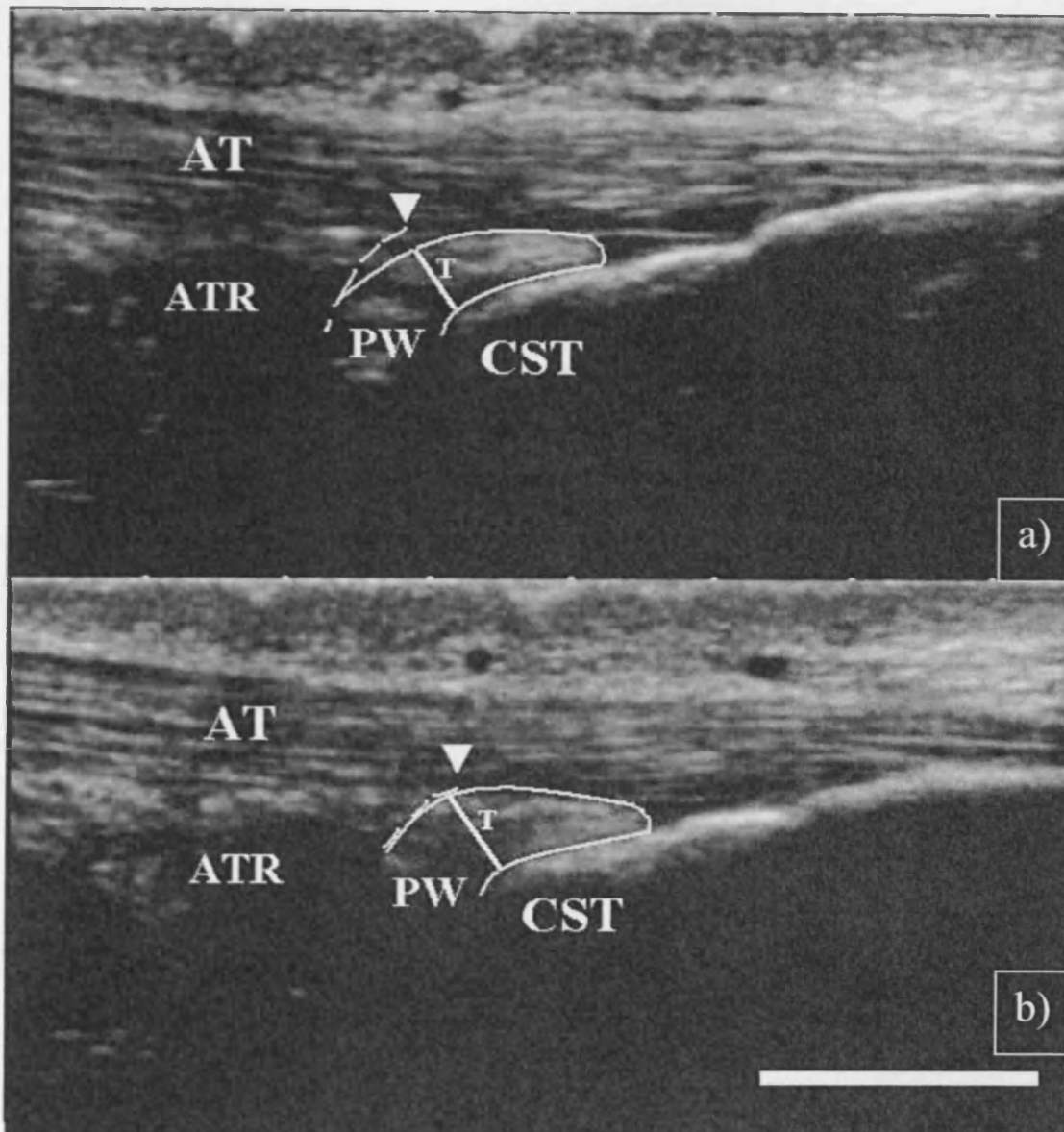


Figure 5.8: Sagittal US images measuring PW thickness. PW tip thickness (T) was measured at 4mm away from PW's tip. PWT is thicker during ankle plantarflexion (a) by 0.5 mm on average (maximum change = 1 mm, SD = 0.5 mm) compared to when the ankle is flexed from plantarflexion to neutral position (b). AT = Achilles tendon, ATR = Achilles tendon related fat pad, PW = the protruding wedge fat pad, CST = calcaneal superior tuberosity, cut up line = synovial wall separating ATR and PW, Scale bar = 1 cm

2.21 AT Bending

It is widely understood that gastrocnemius and soleus muscle group contractions apply tension on AT [56]. US images collected from the first study (Chapters 3) showed AT bends are present usually in the ankle plantarflexion position (Figure 5.9). AT bends were observed during passive ankle flexion (Chapter 3) in every volunteer, as well as during Active ankle flexion in 10 out of 25 volunteers. During every ankle flexion where AT bends were found, PW seemed to reach the most proximal point to the AT insertion. As previous studies suggested KFP may serve to reduce such bends, this study examined the effect AT bends on PW's motion [3,16].

Obvious AT bends were observed in 2 out of 5 volunteers during active ankle flexion against loads between 0 and 1 kg. No AT bends were observed in any volunteer against loads of 2 kg or higher. Obvious AT bends usually were observed below the fibrous anchor attaching KFP to AT (distal region of ATR-AT attachment) (Figure 5.10).

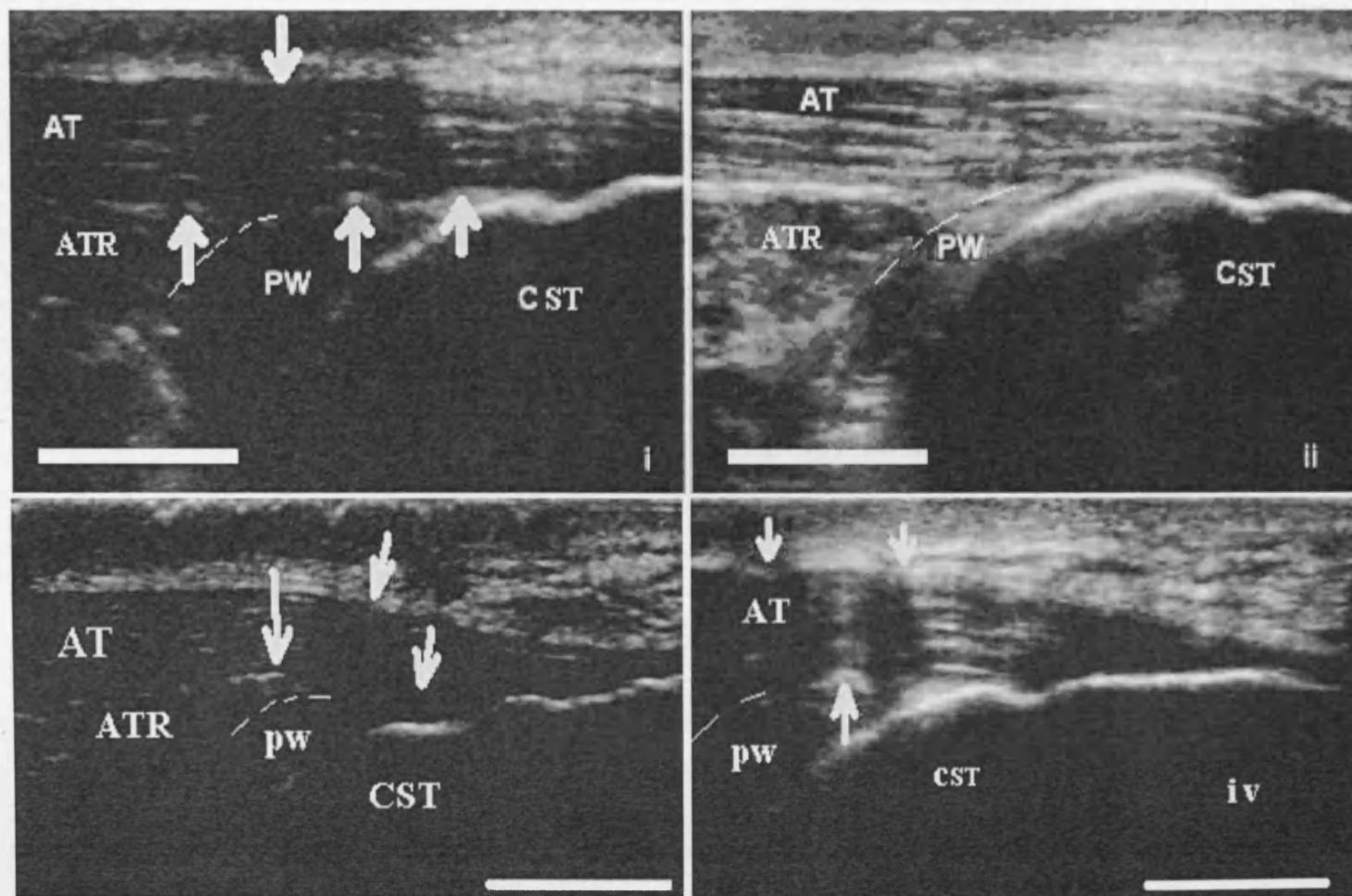


Figure 5.9: US images taken in the sagittal plane showing AT bends (arrows) present in the plantarflexion (i) compared to neutral flexion position (ii) in passive ankle flexion. AT bends were also evident in unloaded active ankle flexion (iii & iv). In some volunteers PW is observed to 'push' ATR superior-posteriorly away from CST as the ankle is passively flexed towards maximum plantarflexion. Cut up line is the separation film between AT related pad (ATR) and protruding wedge (PW). AT = Achilles tendon, PW = protruding wedge, C = calcaneus, scale bar = 1 cm.

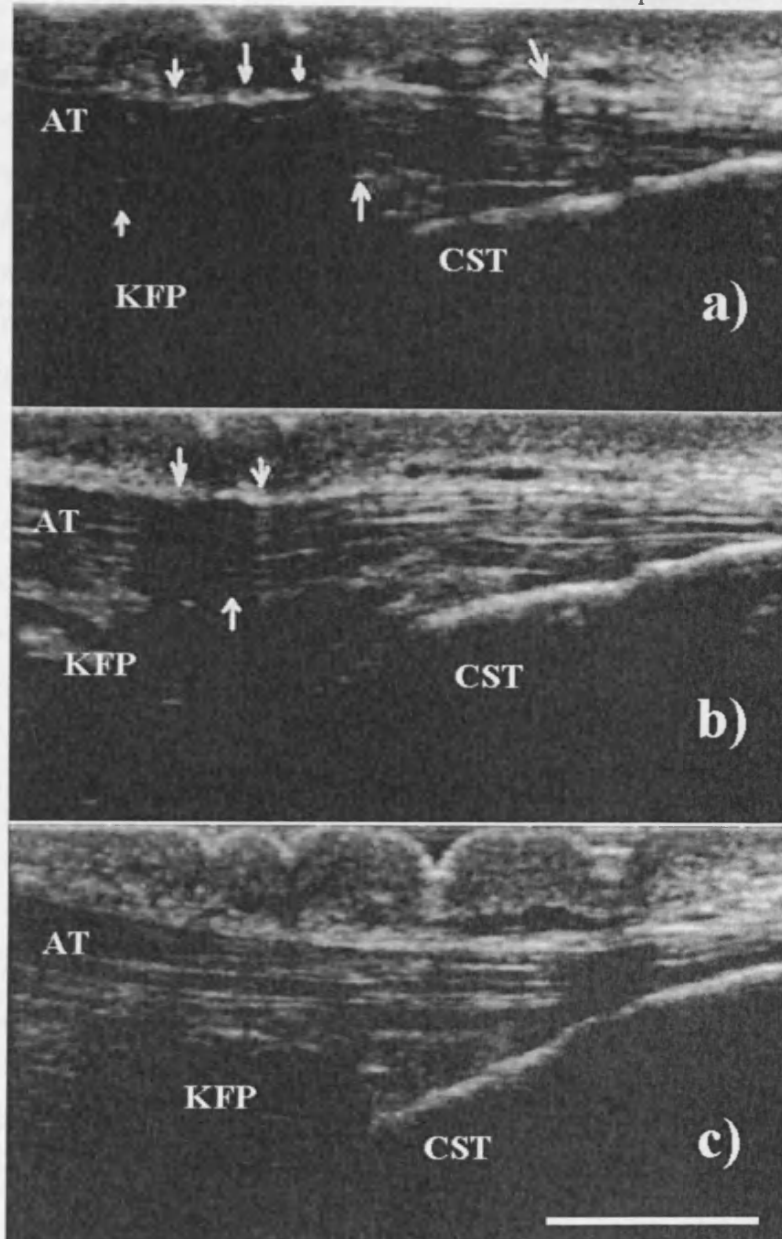


Figure 5.10: Saggital US images showing AT bends (arrows) present during maximum plantarflexion. Obvious AT bends were observed during passive plantarflexion (a). AT bends were observed in 2 out of 5 volunteers during active ankle flexion against loads between 0 and 1 kg (b). No AT bends were observed in any volunteer against loads of 2 kg. Obvious AT bends usually were observed below the fibrous anchor attaching KFP to AT (distal region of ATR-AT attachment). Scale bar = 1 cm.

2.22 Assessing KFP Area, Shape & Volume Variations

MRI scanners produce a number of 2 D images, or 'slices', that when placed adjacent to each other in the correct order, a 3 D image can be constructed (Figure 5.11). This study used the commonly used 'Dicom' software (DicomWorks© Version 1.3.4) to view and process the acquired MR images. Images were converted into a different format (bitmap) for area and volume analysis using a 3 D reconstruction software (Reconstruct©, version 1.1.0.0, 2005). From each MRI slice, KFP borders were outlined and the software's calculator provided the area within the outlined region.

The 3 D software also calculated the volume of the KFP by reconstructing a 3 D model of KFP using the MRI parameters acquired from the scanner (slice depth and gap). Reconstruct© uses these parameters to create a 'smooth' 3 D representation. A previous study calculating the volume of knee menisci showed that MRI volume calculation results showed on average 5% smaller (SD 4%) volume compared to the water displacement method. On the other hand, such underestimation was consistent in all images [52,53].

5.4.1 Materials & Methods

A number of methods were utilized for this study. As used to determine the knee meniscus cross sectional area and volume changes [52,53,57], MRI scanning was used to study KFP cross sectional area and volume during ankle flexion. Dynamic US imaging was used to study PW hysteresis and AT bending.

2.22.1.1 MRI Examination

Two MRI scanners were available for this study; a 0.2 T and a 3 T machines. The Cardiff University Brain Research and Imaging Centre (CUBRIC) scanner (3 T) incurred a cost, where the Cardiff University School of Engineering scanner (0.2 T) is free of charge to use⁵. The difference in specifications between the two scanners (Table 5.1) meant that the 3 T provides 3 times more slices per scan than the 0.2 T machine, offering greater precision in area and volume calculations, and consequently less errors. For both scanners, foam cushions were placed around

⁵ Both MRI scanners are regularly tested and calibrated by their manufacturers by scanning a phantom.

the ankle for stability to minimize movement artifacts and help place the ankle within the scanner's field of view (FOV).

Parameter	School of Engineering MRI	CUBRIC MRI
Magnetic Field Strength	0.2 T	3 T
Maximum Field of View	12 X 12 cm	48 X 48 cm
Minimum Slice Thickness	5 mm	2 mm
Minimum Slice Gap	1 mm	0 mm
Usage Cost	Free	Not free

Table 5.1: Specifications of both MRI scanners available for this study, where;

Field of view (FOV) = Dimensions of acquired image

Slice thickness = Depth of each 2 D image shown

Gap thickness = Gap skipped between consecutive slices

2.22.1.2 Pilot Study

2.22.1.2.1 MRI Study Repeatability & Protocol Evaluation

Using the 0.2 T scanner, 3 volunteers were scanned three times in the same ankle flexion position (maximum plantarflexion). Repeatability testing by scanning the same volunteer in three different occasions showed a coefficient of variance within volume of 5%. The average KFP dimensions from the 3 volunteers were 29 x 60 x 41 mm (x, y and z planes respectively in the sagittal plane). Table 5.2 shows the 0.2 T scanner have uncertainties of 10%, 20% and 14.5% in height, width and depth measurements respectively. The 3 T machine has maximum uncertainties of 3.3%, 6.8% and 4.5% in height, width and depth respectively. No repeatability was carried out on the 3 T scanner since the cost incurred, however, as the scans were conducted by the CUBRIC knee and ankle joints imaging specialist.

KFP volume was calculated by collecting the transverse slices in order to reduce uncertainty and increase 3 D model resolution. The 0.2 T scanner produces on average 11 slices containing KFP in the transverse plane, compared to the 32 slices acquired using the 3 T scanner. MR images were acquired in the transverse plane to construct KFP's 3 D

model to measure its volume; and in the sagittal plane to measure the area. Also, KFP boarders were outlined 5 times for each midline slice to measure the repeatability of reaching similar results from the same image. Results showed a maximum variation coefficient of 2%.

MRI Scanner	Slice Depth	Height	Width	Depth	3 D uncertainty
0.2 T	6 mm	10 mm	20.8 mm	14.6 mm	10 %
3 T	2 mm	3.3 mm	4.9 mm	6.8 mm	3.3 %

Table 5.2: Measurement uncertainty of both 0.2 T and 3 T MRI scanners used for this study. As the slice depths (slice thickness + slice gap) are 6 and 2 mm, maximum measurement uncertainties are 10% and 3.3% respectively. Since volume is calculated from transverse plane images, 3 D uncertainty is that of the transverse plane.

Prior to every MRI scan a safety precaution check was carried out in the form of a questionnaire to eliminate any risks of bringing metals to the vicinity of the MRI scanner (full check document is attached in Appendix IV). The number of volunteers acquired for this test is 5 as time and costs endured by using the 3 T scanner limited the number of volunteers. Using the 0.2 T scanner, the ankle of 5 healthy volunteers was scanned (2 females & 3 males, Age 20-28, BMI 21-26). Volunteers were prone on the MRI scanner bench and cushions were placed underneath the foot for comfort and stability. First, the cushions were arranged to place the ankle in the neutral position. Then, more cushions were placed underneath the foot, lifting the toes to support the ankle in its plantarflexion position. A pre-scan (quick low resolution scan) was carried out before every scan to position KFP in the centre of FOV. Furthermore, the cushions used were placed without moving the ankle, to minimize any ankle orientation changes between scans. Reconstruct® software package was used to outline the KFP area in each slice and calculate the overall volume of KFP.

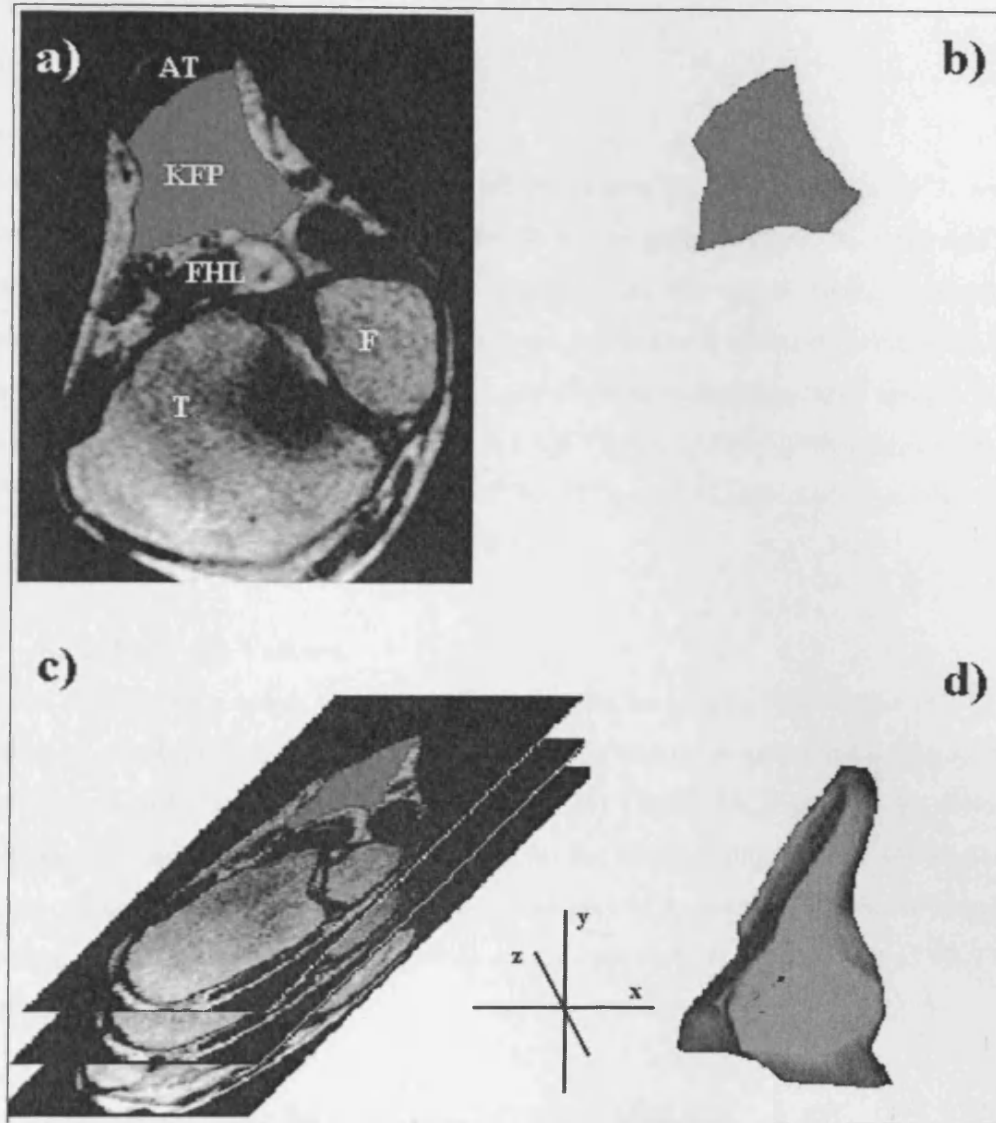


Figure 5.11: Calculating the volume of KFP is carried out by highlighting the borders of KFP (a) in every MRI transverse slice. To construct a 3 D model and calculate the volume, transverse MR images are stacked up in order (c). Reconstruct© places the highlighted area in order to construct the 3 D model (d). AT = Achilles tendon, KFP = Kager's Fat Pad, FHL = Flexor Hallucis Longus, T = Tibia, F = Fibula. Dimension bars indicating that KFP's dimension directions, height = y axis, width, x-axis, depth, z-axis.

2.23 Results

2.23.1 MRI Examination

- **KFP Shape**

Both 0.2 T and 3 T scanners show that in all volunteers, KFP seemed to have 'L' and 'J' shapes in neutral and plantarflexion positions in the sagittal plane, as described in a previous MRI study of KFP [1]. For example, as the ankle flexes towards the plantarflexion position ATIA seemed to increase, while the FHL-calcaneus and the FHL-AT angles decreased (Figures 5.12 & 5.13). On average, comparing ankle neutral flexion to plantarflexion positions at AT midline, AT-CST angle (ATIA) changed from 19.2° to 30.4°, FHL-CST angle changed from 79.2° to 55° and FHL-AT angle (or FHL-soleus angle) changed from 43.4° to 33.2° (Table 5.3).

- **KFP Area and Volume**

From the 0.2 T MRI scanner, the AT midline slice in the sagittal plane showed KFP area is greater at ankle plantarflexion position than ankle neutral position in all volunteers by an average of 10.12% (standard deviation = 2.42%) (Table 5.4, Figure 5.14). However, the number of sagittal slices containing KFP in the sagittal plane is 1-2 slices more in neutral position compared to plantarflexion position. As a result, KFP volume seemed to be greater during ankle plantarflexion than neutral position by a maximum of 9% (Table 5.5) (Figure 5.15).

The relatively thick slice depth (slice thickness + slice gap = 6 mm, 10% of KFP's height) of this scanner meant that the most distal slice of KFP in the transverse plane showed shadow artefact, increasing measurement uncertainty and error. In some cases, the tip of PW was visible in the sagittal plane but not in the transverse plane due to its thin nature (Figure 5.16). Therefore, volume results from this scanner were found inconclusive.

Since ATR's borders are clearly distinguishable in sagittal plane MR images, unlike the PW and DP that seem to be interconnected and continuous, the area of ATR was compared to that of PW and DP combined. Calculating the ATR and PW-DP areas from

AT-midline sagittal plane showed that ATR (Table 5.6) was greater during ankle plantarflexion than neutral ankle position, on average by 3%. Comparing area change results of KFP and ATR (Tables 5.4 & 5.5) suggests that ATR's area changes the least compared to the overall area change of KFP.

Results from 2 volunteers whose ankles were scanned using the 3T MRI scanner at CUBRIC also showed KFP's shape change in the same manner, with its angles changing as described above (Figure 5.12). Calculating the areas of KFP and ATR pads also showed ATR changed its area in the sagittal plane the least (Table 5.7). Comparing AT midline slices showed KFP area was (13.1% & 9.3 %) greater in ankle plantarflexion than neutral flexion positions, confirming results from the 0.2T scanner. Also, the number of transverse plane slices produced was greater in ankle neutral flexion position compared to plantarflexion. However, increased imaging resolution showed that KFP volume decreases by 1.3 & 3.9% from neutral to plantarflexion positions. Since both volunteers were the first 2 volunteers scanned using the 0.2T scanner, the second volunteer showed a reduced volume change in KFP when scanned using the 3T MRI machine. Similarly, results (Table 5.7) confirmed that ATR's area seemed to change the least in the sagittal plane compared to KFP in general, suggesting that PW and DP are prone to more area changes during ankle flexion than ATR.

Flexion	Ankle Neutral Flexion Position			Ankle Plantarflexion Position		
Volunteer	A (°)	B (°)	C (°)	A (°)	B (°)	C (°)
1	20	82	41	28	52	25
2	20	85	51	29	55	40
3	22	81	30	34	60	20
4	18	70	50	29	50	42
5	16	78	45	32	58	39

Table 5.3: Comparing the changes in angles (highlighted in section 5.5.1.A) between ankle neutral and plantarflexion positions. A = angle between FHL and AT (or Soleus in some cases), B = angle between FHL and CST, C = angle between AT and CST.

Volunteer	NFP Area (cm ²)	PFP Area (cm ²)	Change (%)	N Vol (cm ³)	P Vol (cm ³)	change (%)
1	5.88	6.82	13.6	20.58	20.46	0.50
2	5.63	6.08	7.4	19.71	18.24	7
3	9.43	10.29	8.3	33.51	30.47	9.1
4	9.52	10.41	10.5	30.3	31.23	3
5	7.71	8.65	10.8	26.98	26.55	1.50
Mean	7.63	8.45	10.12	26.11	25.47	4.2
SD	1.86	1.97	2.42	5.86	5.93	4.9

Table 5.4: Results of KFP area changes in the sagittal plane using 0.2T MRI scanner showing KFP area is greater at ankle plantarflexion position (PFP) than ankle neutral flexion position (NFP) in all volunteers. Mean KFP area change = 10.12%, standard deviation (SD) = 2.42%. KFP volume was larger at ankle neutral position than plantarflexion, mean volume change is 4.2%, SD = 4.2%.

Volunteer	NFP Area (cm ²)	PFP Area (cm ²)	Change (-%)
1	3.91	3.43	12
2	3.45	3.22	6.7
3	6.12	5.43	11.2
4	6.47	5.74	11.5
5	3.93	3.54	9.9
Mean	4.78	4.27	10.26
SD	1.4	1.2	2.14

Table 5.5: Results of KFP area changes in the transverse plane using 0.2 T MRI scanner showing KFP area is greater during ankle neutral position (NFP) than plantarflexion position (PFP). KFP's area decreases in the transverse place as the ankle is flexed in the plantarflexion direction, which supports results that KFP's volume is constant. The middle slices were used for this comparison.

	ATR Volume (cm ²)		
Volunteer	Neutral Position	Plantarflexion	Change %
1	2.47	2.56	3.5
2	2.02	1.99	1.5
3	3.36	3.42	1.74
4	4.12	4.28	3.73
5	2.81	2.93	4.1
Mean	2.95	3.03	3
SD	0.814	0.872	1.07

Table 5.6: Results from the 0.2 T MRI scanner showing ATR volume is larger at ankle neutral position compared to ankle plantarflexion.

Vlt	NFP Area (cm ²)	PFP Area (cm ²)	Change (%)	N Vol (cm ³)	P Vol (cm ³)	Change (%)
1	5.95	6.85	13.1	20.83	20.55	1.3
2	5.52	6.12	9.3	19.32	18.56	3.9

Table 5.7: Results from the 3 T MRI scanner showing KFP area changes are similar to those of the 0.2 T scanner. However, KFP volume changes at a lower rate when tested with the 3 T scanner compared to using the 0.2 T scanner. Vlt = volunteer, Vol = volume.

Volunteer	Neutral Position (mm ²)	Plantarflexion (mm ²)	Change %
1	2.51	2.6	3.4
2	2.07	2.04	1.4

Table 5.8: 3 T MRI scanner showing ATR area change between ankle plantarflexion and neutral position.

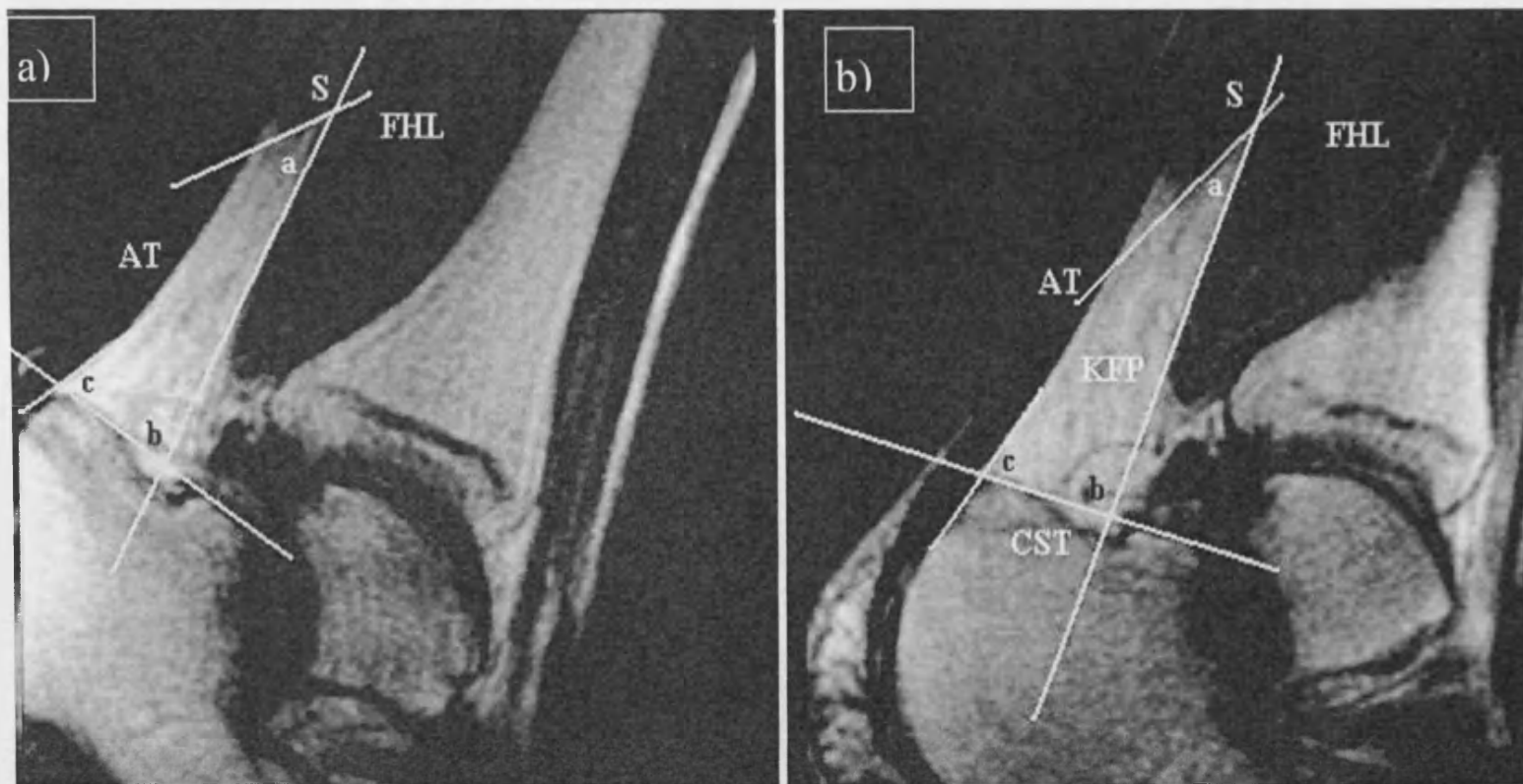


Figure 5.12: A sagittal MRI image of a volunteer comparing ankle neutral flexion (a) to plantarflexion (b) positions at AT midline, AT-CST angle (c) changed on average from 19.2° to 30.4° , FHL-CST angle (b) changed from 79.2° to 55° and FHL-AT angle (or FHL-soleus angle) (a) changed from 43.4° to 33.2° (Table 5.3).

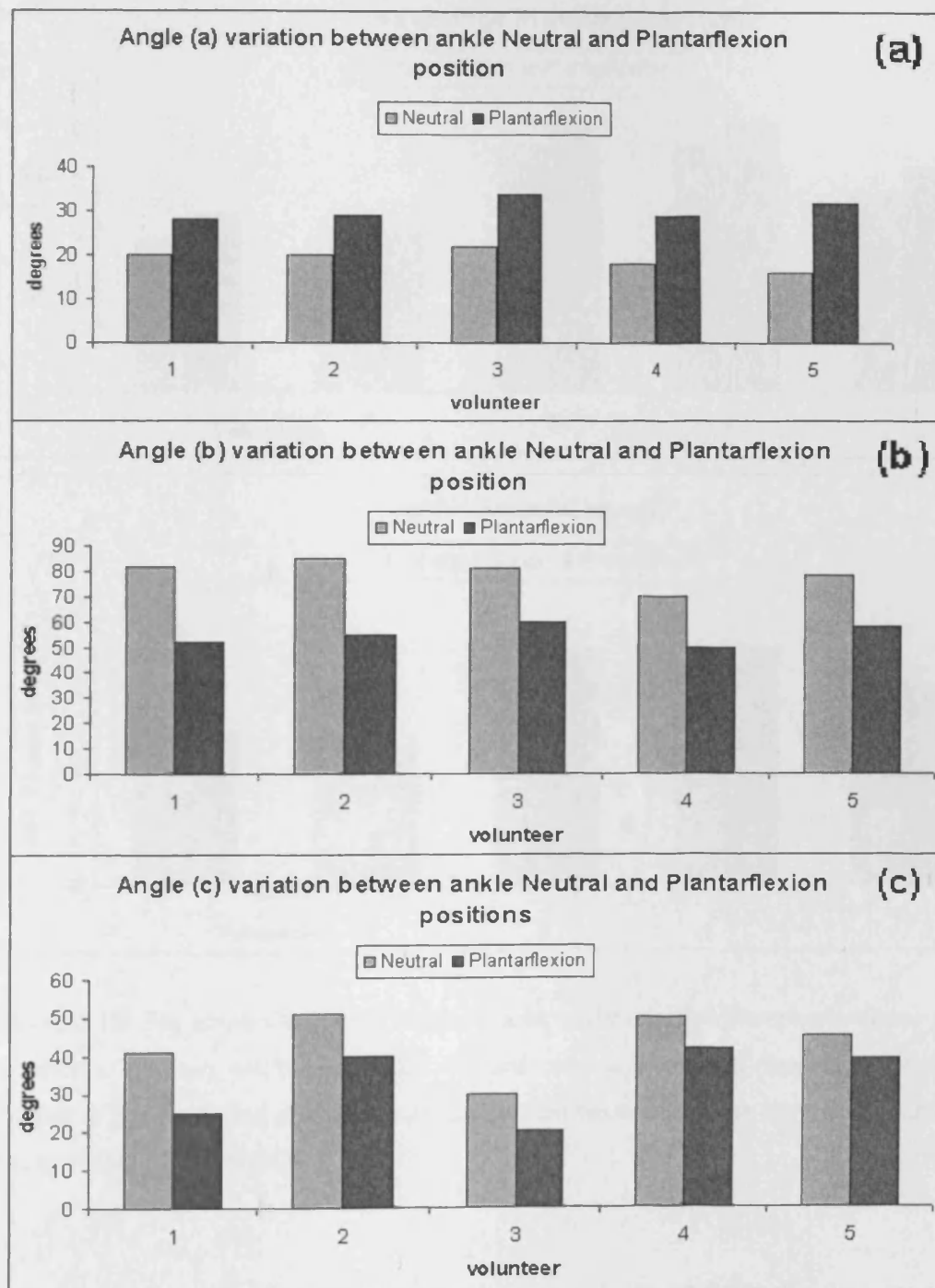


Figure 5.13: A bar graph illustrating the changes in Kager's triangle's angles, FHL-AT angle (a), FHL-CST angle (b) and AT-CST angle (c) (Table 5.3).

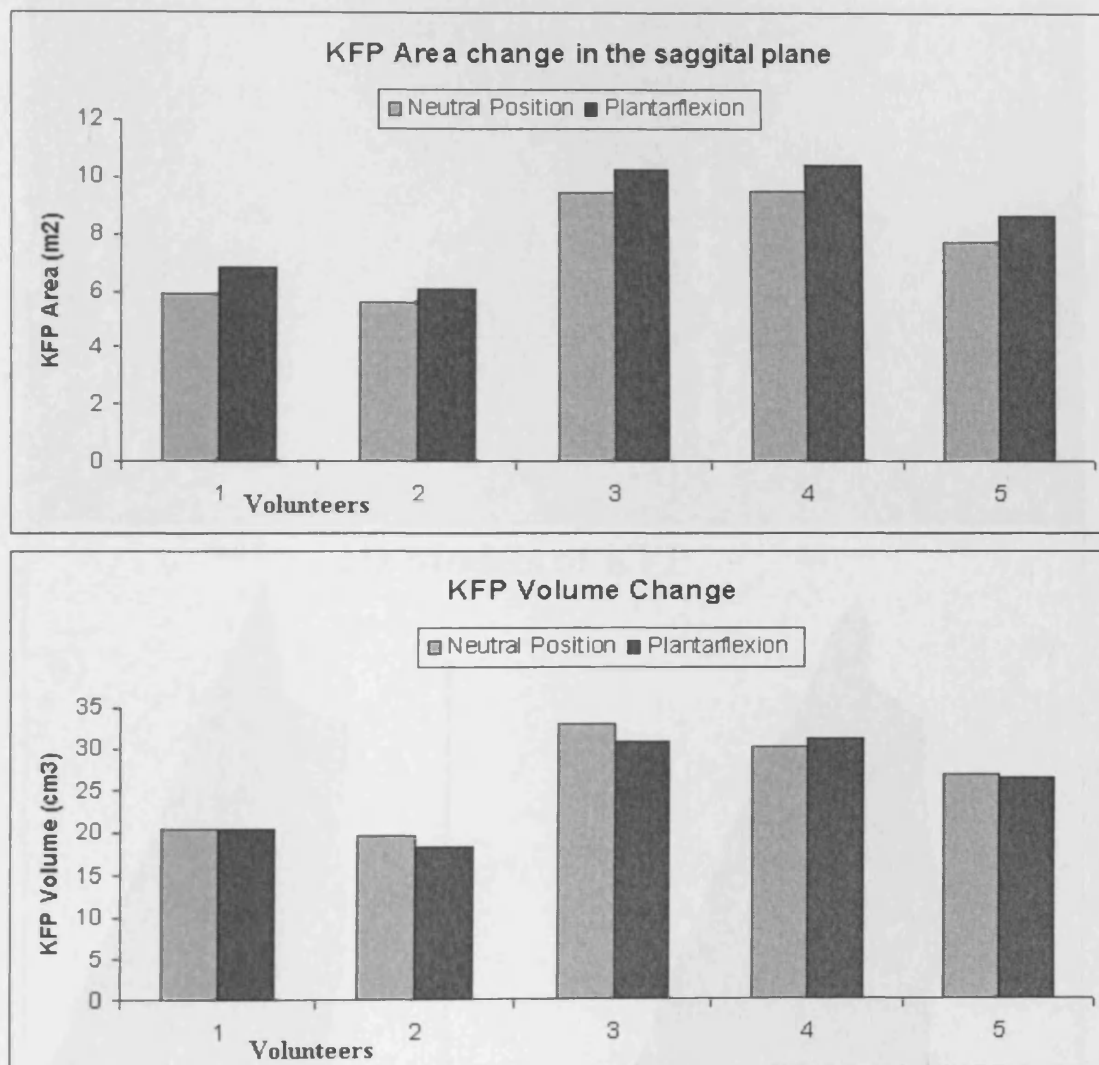


Figure 5.15: Bar graph illustrating the KFP area in the saggital plane and volume in all 5 volunteers between ankle plantarflexion and neutral positions. Results showed KFP volume is greater during ankle plantarflexion than neutral position by a maximum of 9% (Mean = 3%, SD = 1.04%).

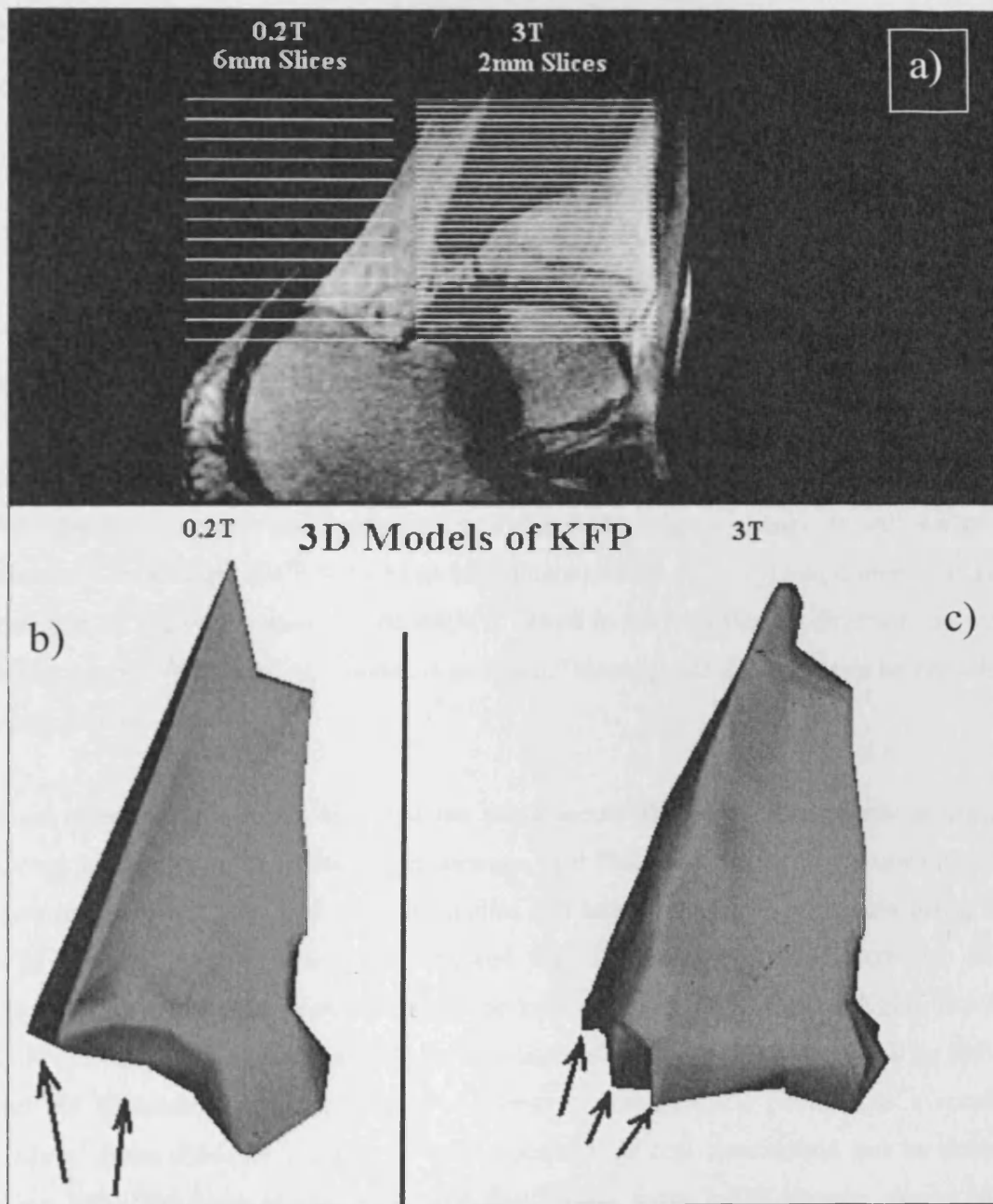


Figure 5.16: (a) A sagittal MRI image showing the number of transverse slices needed to show KFP. The 0.2 T scanner has 10% uncertainty. In some cases, the tip of PW and other thin sections (arrows) were not visible in the transverse plane due to uncertainty in 0.2 T scanner (b), but were clear in the 3 T transverse images (c). 3 T scanner helped produce more precise 3D models than the 0.2 T scanner.

2.24 Discussion

KFP's area in the sagittal plane decreased as ankle flexes from plantarflexion to neutral by 10.12%. Although the 0.2 T scanner suggested a maximum increase in KFP volume of 9.1% from ankle plantarflexion and neutral positions, the mean value of KFP volume change was 4.9%, which is within the measurements' uncertainty of the 0.2T scanner of 10%. After scanning 2 out of the 5 volunteers using the 3 T machine at CUBRIC, data also showed similar changes in KFP area as shown from the 0.2 T (13.1 & 9.3%, compared to 13.6 & 7.4% using the 3T and 0.2 T scanners respectively). However, KFP volume increase declined to 3.9%. Since the resolution of the 3 T scanner is 3 times higher than the resolution of the 0.2 T scanner, results from the 3 T scanner were considered more accurate. Furthermore, since KFP volume change is still within the scanner's uncertainty, KFP showed no significant change in its volume. Since KFP's area increases in transverse plane as the ankle is flexed in the dorsiflexion direction, decreases in the sagittal plane and its volume is constant, this suggests that KFP can be considered a non compressible tissue.

Knee meniscus studies showed that the cross sectional area of knee meniscus changes during loading or knee flexion by an average of 9.8%, and the overall volume change of knee meniscus of 3.5% and 5.9% in medial and lateral menisci respectively using a 3T MRI scanner [58,59]. This study showed that KFP's overall area decreases during dorsiflexion by a similar range to that of the knee meniscus (10%). MR imaging lacks the ability to test loading effects mainly for the discomfort that the volunteers will go through and the likeliness of the volunteers to move or change ankle position as a result of loading. Also, dynamic changes of PW's position in real time would not be detected using MRI. Previous studies measured PWD only from 3 US images, during ankle plantarflexion, neutral and dorsiflexion positions [1]. Therefore, real-time changes of PWD, PWT and other parameters were measured across the entire range of ATIA using dynamic US imaging. This study showed PW hysteresis is evident in individuals with a non-straight shaped retrocalcaneal wall.

High refresh rate US imaging showed plateau regions of PW against ATIA showing that PW travels slower as the ankle is flexed towards its maximum plantarflexion and dorsiflexion positions compared to during the neutral position region. During the plantarflexion plateau region, PWT was observed to increase in all volunteers. PWT was also observed to decrease as the ankle is flexed in the dorsiflexion direction, compared to ankle plantarflexion. As PW is contained in a synovial membrane, this supports the theory that the change in PWT during dorsiflexion assists in releasing synovial fluid into the bursal space during dorsiflexion as a result of PWT decrease, supporting and explaining hypotheses that KFP provides dynamic lubrication to AT enthesis organ [1,16]. Since (i) previous studies showed fibrosis is developed as a result of resisting external loading [26-29] and can be found on PW's tip, (ii) US images showed a decrease in PWT during dorsiflexion, (iii) MRI results showed that KFP is a non-compressible tissue and (iv) PW hysteresis, supporting the hypotheses that PW assists in load bearing at its fibrous tip. The fifth volunteer had a short PWSD range (4mm) and a straight shaped retrocalcaneal wall. In addition, no fibrous tip was evident in the ultrasound images for this volunteer. The volunteer stated no interest in sports and minimal history of sports activities.

During passive- or low-load-active ankle flexion AT bends are evident. However, bends were only observed within the distal part of AT. ATR seemed to increase in the distal area, inferior to ATR attachment to AT. In addition, at maximum plantarflexion (when AT bending was present) PW was evident to increase the separation between ATR and CST. This suggests that KFP assists in reducing AT bending during unloaded active ankle flexion. Furthermore, AT bends were not found in MR images, suggesting AT bends are momentary. The sensory neural network within KFP may act to encourage reaction to eliminate AT bending. AT curves were observed through using MRI during resting ankle plantarflexion.

2.25Conclusions

- The area of KFP in the sagittal plane increases as the ankle flexes in the plantarflexion direction by an average of around 10.1%, similar to the knee meniscus cross sectional area change
- The area of KFP in the transverse plane decreases as the ankle is flexed in the plantarflexion direction by an average of 10.25%
- The volume of KFP is found constant between ankle plantarflexion and neutral position
- The depth of KFP (z-axis) in the sagittal plane increases as the ankle flexes from plantarflexion to neutral position
- PW hysteresis was shown evident, which can explain PW exerting synovial fluid during ankle dorsiflexion to lubricate the subtendinous region. This can also support that PW's fibrous tip is developed as a result of resisting external loads, as shown in the literature review
- PWT decreases as the ankle flexes from plantarflexion to dorsiflexion, and increases in the other direction. This also supports the dynamic lubrication and load bearing functions of PW
- PW's tip is therefore suggested to assist in load bearing within the AT enthesis during ankle dorsiflexion

2.26Next Chapter

Chapter 6 discusses the general findings of this PhD research. Chapter 7 states the main conclusions and possible future work for this research.

Chapter 6

Discussions

Although recent studies debated the biomechanical advantages of Kager's fat pad, they hypothesized a number of functions that KFP provides to the AT enthesis organ that mirror those of the knee meniscus. Both KFP and the meniscus were considered to serve as a variable space fillers [11,12,21] and are hypothesized to provide a number of biomechanical advantages including load bearing, pressure and stress distribution, as well as subtendinous lubrication promoting low wear. Anatomically, they both were found to include vascular and neural supplies [1,16,20,60-62], and while the knee meniscus consists predominantly fibrous tissue, fibrosis was found evident at the tip of PW, which is shown to be developed as a result of resisting external loading [26,27,62-64]. PW has also been suggested to have an immuno-protective role within RB - removing dead cell debris produced by wear and tear of its lining tissues [21]. Examinations were carried out on KFP and PW to help support or refute their hypothesized biomechanical importance within AT enthesis organ.

The tip of PW travels against the displacement of the calcaneus bone during ankle flexion. Although it was suggested that this displacement encourages the motion of PW's tip, the anchorage between CST and PW suggests that PW's motion would travel in the same direction as the calcaneus, which is not the case. Hence, PW's motion is not caused by the displacement of the calcaneus directly, however this anchorage may assist in restricting or guiding KFP's motion.

The motion of PW was also hypothesized to be caused (or influenced) by the activities of FHL muscle. Results showed that PW's tip can travel with the absence of FHL's activities during passive ankle flexion. In addition, PW's tip was still in its location while FHL was repeatedly being flexed and extended during the 'FHL only' test (Chapter 3). This shows FHL activities are not a direct cause of PW's motion. On the other hand, PWSD was found to increase by 60% between ankle passive flexion and active-unloaded flexion. Similarly, PWSD is 60% greater during active-loaded flexion compared to active-unloaded flexion. Although this relationship can support suggestions that AT loading and change in retrocalcaneal pressure influence the motion of PW, a strong relationship was also found between PW's sliding distance and the angle of AT insertion

(angle between AT and retrocalcaneal wall of the calcaneus bone). Since the relationship between AT insertion angle and AT load was found linear, depending on the shape of CST's wall (Chapter 5), PW's motion is dependent on AT insertion angle, and therefore the change in pressure. Since this PhD is focused on in-vivo testing of KFP's functions, and no non invasive methods can accurately detect in-vivo pressure variations, investigating the retrocalcaneal pressure was therefore limited to speculations.

While it was previously shown that, in-vitro, KFP potentially can reduce load applied between two surfaces by 39%, similar to that of the knee meniscus (30% - 70%), this study found a PW hysteresis when measuring PW's position against all possible angles of AT insertion during ankle flexion. As fibrosis was found in the PW tip, which is believed to be a result of resisting external loads, it can be speculated that PW serves as a load bearer in-vivo by being subjected to enough loads and external forces to cause fibrosis within its tip. In addition, the reduction in PW thickness during dorsiflexion can explain the mechanism of synovial fluid exertion into the AT enthesis. This change in PW's thickness can explain the presence of fibrosis on PW's tip, as well as supporting that PW assists in load bearing during ankle dorsiflexion. This means that during dorsiflexion, PW thickness reduces, excreting synovial fluid from its synovial folds, and assisting in load bearing at PW's tip as it retracts from the retrocalcaneal space.

MRI investigations showed that KFP area in the sagittal plane (at AT midline) reduces by around 10% when ankle flexes from plantarflexion to neutral positions, similar to the cross area reduction of the knee meniscus when the knee is flexed, or loads are applied [52,53,57,65]. The transverse plane area of KFP (middle slice), however, increases at the same rate of 10%, which is confirmed by KFP's volume changed at a maximum rate of 3.9% between ankle plantarflexion and neutral position, also similar to the knee meniscus when under loading, or knee flexion [52,53,57,65]. However, since the scanner's uncertainty was 3.3%, KFP's volume was considered constant. Although KFP has a longer sliding range than the knee meniscus (10.5mm compared to 3.5mm) under loading, the similar area and volume change rates, in addition to KFP being non-

compressible, support the theory that the hysteresis (or lagging) assists in AT enthesis load bearing and/or shock absorbing.

The ATR changes the least in area between ankle plantarflexion and neutral positions, being surrounded by the deep fascia and paratenon. As blood flow through KFP was only demonstrated within ATR through literature review, these findings support the speculated function of ATR to protect the neural and vascular supplies to AT.

PW's motion graph changes depending on the shape of retrocalcaneal wall. In volunteers with a non-straight shaped retrocalcaneal wall, PWD seemed to have a non-straight shaped graph with ATIA, suggesting PW slides at different speeds inside the bursal space depending on the shape of CST. In one volunteer with a straight shaped retrocalcaneal wall, PWD had an evidently straight line relationship with ATIA. The fifth volunteer has a retrocalcaneal wall that is shaped as two straight lines joined at a prominent point. It was evident in all volunteers that PW's speed reduces as the ankle reaches its maximum plantarflexion or dorsiflexion positions with PW's speed being highest at the ankle neutral position.

During passive- or low-load-active ankle flexion AT bends are evident. However, bends were only observed within the distal part of AT. In addition, at maximum plantarflexion (when AT bending was present) PW was observed to increase the separation between ATR and CST. This suggests that KFP assists in reducing AT bending during low loaded active ankle flexion. Furthermore, AT bends were not found in MR images, suggesting AT bends are momentary. The sensory neural network within KFP may act to encourage a reaction to reduce the bends.

The consequences of KFP removal in humans is not established, however, animal studies showed that fat pad removal can alter the growth of the related tendon by up to 25% in rabbits [37]. It is also suggested that fat pads are considered as growth plates for the joints, which speculates KFP serves to repair and regenerate cells within AT enthesis [21]. Although removing KFP may symptomatically relieve pain, animal testing showed

it encourages growth of scar tissue causing pains and limiting the dorsiflexion range [38]. From the results of this PhD it can be speculated that KFP removal can lead to reduction in dynamic lubrication, less encouragement of motion between AT and CST, increasing AT bends, and AT wear and tear. Similarly, knee meniscus removal was found to encourage cartilage wear, increasing pain in the knee joint, reduction in load bearing, and reduction in cartilage lubrication [11,12].

Chapter 7

Conclusions and Future Work

2.27 Conclusions

This PhD investigated a number of the hypothesized biomechanics of Kager's fat pad and its importance within the AT enthesis organ. The conclusions for this research are;

- The displacement of the calcaneus was suggested to encourage the motion of PW. The anchorage found between PW and CST suggests PW travels in the direction of the displacement of the calcaneus. However, the tip of PW was observed to travel against the direction of the displacement of the calcaneus bone in all volunteers. Such anchorage can be speculated to restrict the motion of PW
- The activities of FHL were also speculated to encourage the motion of PW's tip. This PhD found no influence of FHL's activities on PW's position or its sliding distances. PWSD did not appear to be influenced by age, BMI, weight, height, or ankle orientation. Furthermore, no contralateral differences were observed in PWSD
- PWSD increases with load, until it reaches the most proximal point of the AT insertion. PWSD increases exponentially with increasing AT load, until load reaches 2 kg, while the position of PW's tip decreases exponentially with increasing AT load until load reaches 2 kg
- The location of PW's tip is influenced by ATIA. The ranges of both PWSD and ATIA increased exponentially with increasing AT load in a similar pattern. Furthermore, the relationship between PWD and ATIA appears to be controlled by the shape of the individual's CST lining
- The area of KFP in the sagittal plane decreases as the ankle flexes from plantarflexion to neutral position (10.12%), while the volume did not change above the error bar (3.3%), suggesting that KFP is non compressible in nature to speculate KFP serves as a load bearer within Kager's triangle and AT enthesis. PW hysteresis is found in volunteers with an evidently fibrous PW tip. This hysteresis was found

typically in the plantarflexion region of the ankle flexion cycle. This supports speculations that PW serves as a load bearer as it retracts from AT enthesis

- The thickness of PW's tip decreases as it retracts away from AT insertion, and increases in the other direction. This supports the hypotheses that PW provides dynamic lubrication to AT enthesis as synovial fluid. Similar to the knee meniscus, synovial fluid is exerted when the tissue is under loading. This also supports speculated load bearing functions of PW as the ankle flexes from plantarflexion to dorsiflexion
- The area of ATR changes the least compared to DP and PW, during ankle flexion, supporting the hypotheses that ATR protects AT vascular supply. PW also appears to separate AT from CST when AT bends are found, encouraging the motion between AT and CST, and hence reducing AT bends

Features	Kager's Fat Pad
Shape	<p>Triangular in the sagittal plane</p> <p>Shape changes between 'L' and 'J' during flexion</p> <p>Area changes by around 10% in the sagittal plane,</p> <p>No volume change detected.</p>
Location	Occupying Kager's triangle between AT, FHL and CST
Anchorage	<p>Fibrous connections linking the KFP to AT and superior calcaneal tuberosity.</p> <p>Fascial sheath and peroneal retinaculum surround the KFP causing an air tight seal</p>
Fibrosis	<p>PW usually has a fibrous tip</p> <p>Fibrous Tip of PW is visible in most volunteers in US</p>
Vascularity	Small blood vessels pass through AT adjacent section of KFP branching from the posterior tibial and peroneal arteries
Movement	<p>Protrudes into the retrocalcaneal bursa during plantarflexion and retracts during dorsiflexion</p> <p>PW's motion is influenced by ATIA and loading</p>
Load bearing	<p>In-vitro testing suggested KFP minimizes load upon AT entheses by 40%</p> <p>Hysteresis and fibrous tip of PW suggest PW bears loads in-vivo</p>
Healing	<p>Fat pads in general were suggested to heal after a number of injuries.</p> <p>No regeneration after partial removal</p>
Consequences of removal	Shortening of AT during growth phase. Speculated to cause lack of protection of AT blood supply, lubrication and load or stress distribution, increasing wear and tear

Table 7.1: List showing the main findings of this PhD (bold font)

2.28 Future Work

The proposed work listed below is identified to be beneficial for further establishing KFP's functions and quantifying them.

2.28.1 Investigating Outside the 'Control' Group

Although this research focused on healthy volunteers in order to find the normal ranges of fat pad motion and functions, active vascularity is only evident when AT is injured, such as during AT tendonitis. This research had a volunteer whose lifestyle was not of the sports playing nature, this volunteer showed no apparent fibrous tip for PW. The PW for this volunteer seemed to slide the least (4 mm maximum sliding range). No conclusions can be drawn as the sample size is too small. Also, knowing that synovial fluid is produced at a higher rate during pregnancy [79], studying PW's parameters including PWSD and its hysteresis would be beneficial to confirm this research's findings. An ideal examination would be a time study on volunteers who went through KFP partial or complete removal to evaluate consequences of KFP's removal.

Also, as it was proven that KFP's vascular network is only active during injuries, it is essential to study the differences in KFP's characteristics including motion limits, hysteresis and area/volume between an injured and a control group. With the collaboration of a hospital, it may be easy to find a number of patients with specific injuries or disorders to volunteer for this study. Investigating the changes of fat pad's characteristics pre- and post- surgeries can provide further understanding of how the biomechanics are altered during such cases.

2.28.2 Investigating the Effects of Lifestyle on PW's Motion

During this PhD it was noted that lifestyle can affect the results. For instance, two of the volunteers had the same age, BMI, foot size and gender, however one of them had a sporty lifestyle since childhood as opposed to the no history of sports activities of the second volunteer. PW was observed to slide further in the former volunteer (9mm) compared to the latter (5mm). Further investigation can find the extent of lifestyle effects on PWSD and provide further understanding to serve the rehabilitation of AT entheses. This study can also extend to study the effect of CST shape on PW's motion since the relationship between the position of PW's tip and AT's insertion angle is linear.

Chapter 8

References

1 Theobald P, Bydder G, Dent C, Nokes L, Pugh N, Benjamin M. 2006. The functional anatomy of Kager's fat pad in relation to retrocalcaneal problems and other hindfoot disorders. *J Anat*; 208:91-7

2.29

2.30 2 Canoso JJ, Liu N, Traill MR, Runge VM. 1988. Physiology of the retrocalcaneal bursa. *Ann Rheum Dis*;43, 308-12

2.31

2.32 3. Bottger BA, Schweitzer ME, El-Noueam KI, Desai M. 1998. MR imaging of the normal and abnormal retrocalcaneal bursae. *AJR*;170(5): 1239-41

2.33

4. Ly JQ, Bui-Mansfield LT. 2004. Anatomy of and abnormalities associated with Kager's fat Pad. *AJR Am J Roentgenol*;182(1):147-54

2.34 5. Benjamin M, Redman S, Milz S, Büttner A, Amin A, Moriggl B, Brenner E, Emery P, McGonagle D, Bydder G. 2004. Adipose tissue at entheses: the rheumatological implications of its distribution. A potential site of pain and stress dissipation?. *Ann Rheum Dis*;63(12):1549-55

2.35 6. Goodman LR, Shanser JD. 1977. The pre-Achilles fat pad: An aid to early diagnosis of local or systemic disease. *Skeletal Radiol*;2, 81-86

7. Harris CA, Petudo AJ. 2006. Achilles tendon imaging. *Australas Radiol*;50(6):513-25

2.35.1

8. Snow SW, Bohne WH. 2006. Observations on the fibrous retinacula of the heel pad. *Foot Ankle Int*;27(8):632-5

2.36 9. N Numkarunarunrote, A Malik, R O Aguiar, D J Trudell, D Resnick. 2007. Retinacula of the Foot and Ankle: MRI with Anatomic Correlation in Cadavers. *AJR* 188:W348-W354

- 3 10. Benjamin M, Toumi H, Ralphs JR, Bydder G, Best TM, Milz S. 2006. Where tendons and ligaments meet bone: attachment sites ('enthese') in relation to exercise and/or mechanical load. *J Anat.* 208(4):471-90.
11. Cox JS, Nye CE, Schaefer WW, Woodstein IJ. 1975 The degenerative effects of partial and total resection of the medial meniscus in dogs' knees. *Clin Orthop Relat Res.*;(109):178-83.
12. Oretorp N, Alm A, Ekström H, Gillquist J. 1978. Immediate effects of meniscectomy on the knee joint. The effects of tensile load on knee joint ligaments in dogs. *Acta Orthop Scand.* Aug;49(4):407-14.
- 4
- 5 13. Ding C, Martel-Pelletier J, Pelletier JP, Abram F, Raynauld JP, Cicuttini F, Jones G. 2007. Knee meniscal extrusion in a largely non-osteoarthritic cohort: association with greater loss of cartilage volume. *Arthritis Res Ther*;9(2):R21.
14. Shaw HM, Benjamin M (2007). Structure-function relationships of entheses in relation to mechanical load and exercise. *Scand J Med Sci Sports*;17(4):303-15
15. Theobald P, Byrne C, Oldfield SF, Dowson D, Benjamin M, Dent C, Pugh N, Nokes LD. 2007. Lubrication regime of the contact between fat and bone in bovine tissue. *Proc Inst Mech Eng [H]* 221(4): 351-6.
16. Theobald P, 2006. "Biomechanical Analysis of the Achilles Tendon Entesis Organ". PhD thesis. Institute of Medical Engineering and Medical Physics, Cardiff University.
17. Theobald P, Benjamin M, Nokes L, Pugh N. 2005. Review of the vascularisation of the human Achilles tendon. *Injury*;36(11):1267-72.

18. Morel M, Boutry N, Demondion X, Legroux-Gerot I, Cotten H, Cotten A. 2005. Normal anatomy of the heel entheses: anatomical and ultrasonographic study of their blood supply. *Surg Radiol Anat*;27(3):176-83

19. Harish S, O'Donnell P, Briggs TW, Saifuddin A, Flanagan AM. 2007. Myopericytoma in Kager's fat pad. *Skeletal Radiol*;36(2):165-9

5.1 20. Kachlik D, Baca V, Cepelik M, Hajek P, Mandys V, Musil V, Skala P, Stingl J. 2008. Clinical anatomy of the retrocalcaneal bursa. *Surg Radiol Anat*;30(4):347-53

5.2

21. Shaw HM, Santer RM, Watson AH, Benjamin M. 2007. Adipose tissue at entheses: the innervation and cell composition of the retromalleolar fat pad associated with the rat Achilles tendon. *J Anat*;211(4):436-43

22. T. S. Atkinson, P. J. Atkinson, H. V. Mendenhall, and R. C. Haut. 1998. Patellar Tendon and Infrapatellar Fat Pad Healing after Harvest of an ACL Graft. *J Sur Res*;79, 25-30

5.2.1 23. Krips R, Brandsson S, Swensson C, MD, van Dijk CN, Karlsson J. 2002. "Anatomical reconstruction and Evans tenodesis of the lateral ligaments of the ankle: Clinical & radiological findings after follow-up for 15-30 years. *J Bone Joint Surg Br*. 84(2):232-6

5.3

24. HM Shaw, OT Vázquez, D McGonagle, G Bydder, RM Santer, M Benjamin. 2008. Development of the human Achilles tendon enthesis organ. *J Anat*;213(6):718-24.

5.4

25. L Terslev, S Torp-Pedersen, E Qvistgaard, P von der Recke, H Bliddal. 2004. Doppler ultrasound findings in healthy wrists and finger joints. *Ann Rheum Dis*;63:644-648

26. JE Miller-Young, NA Duncan, G Baroud. 2002. Material Properties of the human calcaneal fat pad in compression: experiment and theory. *J Biomech*;35(12),1523-31
27. TC Hsu, CL Wang, YW Shau. 2000. Altered heel-pad mechanical properties in patients with Type-2 diabetes mellitus. *Diabet Med*;17(12)854-9
28. RF Ker, MB Bennett, RM Alexander. 1989. Foot strike and the properties of the human heel pad. *Proc Inst Mech Eng [H]*;203(4)191-6
29. RP Cavanagh, GA Valiant, KW Misevich. 1984. Biological aspects of modeling shoe/foot interaction during running: Ed. E. C. Fredrick, Illinois: Human Kinetics Publishers 24-46
30. Henry Gray. Gray's Anatomy. Running Pr Book Pub. 1974
31. N Numkarunarunrote, A Malik, RO Aguiar, DJ Trudell, D Resnick. 2007. Retinacula of the Foot and Ankle: MRI with Anatomic Correlation in Cadavers. *AJR*;188,348-54
32. M Aström, N Westlin. 1994. Blood flow in the human Achilles tendon assessed by laser Doppler flowmetry. *J Orthop Res*;12(2):246-52.
33. H Langberg, J Bülow, M Kjaer. 1998. Blood flow in the peritendinous space of the human Achilles tendon during exercise. *Acta Physiol Scand*;163(2):149-53
34. Ann Baggailey. Anatomy & physiology and human body Dorling Kindersley publishers, London, 2005.
35. WS Khan, SR Tew, AB Adesida, TE Hardingham. 2008. Human infrapatellar fat pad-derived stem cells express the pericyte marker 3G5 and show enhanced chondrogenesis after expansion in fibroblast growth factor-2 *Arthritis Research & Therapy* Vol 10 No 4

36. A Ghazzawi, P Theobald, N Pugh, C Byrne, L Nokes. 2009. Quantifying the motion of Kager's fat pad. *J Ortho Res* 27(11):1457-60
37. K. Takatoku, H. Sekiya, M. Hayashi, Y. Hoshino, Y. Kariya. 2005. Influence of fat pad removal on patellar tendon length during growth. *knee Surg Sports Traumatol Arthrosc*,13: 706–713
38. M Bohnsack, A Wilharm, C Hurschler, O Rühmann, C Stukenborg-Colsman, CJ Wirth. 2004. Biomechanical and Kinematic Influences of a Total Infrapatellar Fat Pad Resection on the Knee. *Am J Sports Med*; 32(8),1873-80
39. S Harish, P O'Donnell, TWR Briggs, A Saifuddin, AM Flanagan. 2006. Myopericytoma in Kager's fat pad. *Skeletal Radiol*
40. Khan Z, Faruqi Z, Ogyunbiyi O, Rosset G, Iqbal J. 2006. Ultrasound assessment of internal derangement of the knee. *Acta Orthop Belg*. 2006 Jan;72(1):72-6
41. Dilley A, Odeyinde S, Greening J, Lynn B. 2008 Longitudinal sliding of the median nerve in patients with non-specific arm pain. *Man Ther*. 13(6):536-43.
42. <http://www.raosoft.com/samplesize.html>
43. A. Rufai, J. R. Ralphs, M. Benjamin. 1996. Ultrastructure of fibrocartilages at the insertion of the rat Achilles tendon. *J. Anat*. 189,185-91
44. Kachlik D, Baca V, Cepelik M, Hajek P, Vaclav Mandys V, Musil V, 2008. Clinical anatomy of the calcaneal tuberosity. *Annals of Anatomy*, 190(3): 284-291
- 5.5 45. Meneghini et al. 2007. The effect of retropatellar fat pad excision on patellar tendon contracture and functional outcomes after total knee arthroplasty. *The Journal of Arthroplasty*, 22(6);47-50

46. Fithian DC, Kelly MA, Mow VC. Material properties and structure–function relationships in the menisci. *Clin Orthop Relat Res*. 1990; (252):19-31.
47. Thompson WO, Thaete FL, Fu FH, Dye SF. Tibial meniscal dynamics using three-dimensional reconstruction of magnetic resonance images. *Am J Sports Med*. 1991;
48. Bylski-Austrow DI, Ciarelli MJ, Kayner DC, Matthews LS, Goldstein SA. Displacements of the menisci under joint load: an in vitro study in human knees. *J Biomech*. 1994; 27(4):421-431.
49. BB Seedholm, T Takeda, M Tsubuku. 1979. Mechanical factors and patellofemoral osteoarthritis. *Ann Rheum Dis*, 38(4)307-16
50. WR Krause, MH Pope, RJ Johnson. 1976. Mechanical changes in the knee after meniscectomy. *J Bone Joint Surg Am*, 58(5)599-604
51. NG Shrive, JJ O’Conner, JW Goodfellow. 1978. Load bearing in the knee join. *Clin Ortho Relat Res* (131)279-87
- 5.6 52. RK Stone, DW Stoller, SG Irving, C Elmquist, G Gildengorin. 1994. 3D MRI volume sizing of knee meniscus cartilage. *J Arthr Rel Surg*. 10(6): 641-44
- 5.7
53. ME Bowers, GA Tung, BC Fleming, JJ Crisco, J Rey. Quantification of meniscal volume by segmentation of 3 T magnetic resonance images. *Journal of Biomechanics* Volume 40, Issue 12, 2007, Pages 2811-2815
- 6 54. N L Grigg, SC Wearing, JE Smeathers. 2009. Eccentric calf muscle exercise produces a greater acute reduction in Achilles tendon thickness than concentric exercise. *Br J Sports Med*;43:280-3

55. OC De Mello Malheiro, CT Giacomini, LA Jr Justulin, FK Delella, M Dal-Pai-Silva, SL Felisbino. 2009. Calcaneal tendon regions exhibit different MMP-2 activation after vertical jumping and treadmill running. *Anat Rec (Hoboken)*.292(10):1656-62
56. RL Silver, J De La Garza, M Rang. 1985. The myth of muscle balance. *J Bone Joint Surg* 67B(3):432-7
57. DS Mastrokalos, PJ Papagelopoulos, AF Mavrogenis, ME Hantes, HH Paessler. Changes of the Posterior Meniscal Horn Height During Loading: An In Vivo Magnetic Resonance Imaging Study. *Ortho*; 31:68
58. DI Bylski-Austrow, MJ Ciarelli, DC Kayner, LS Matthews, SA Goldstein. Displacements of the menisci under joint load: an in vitro study in human knees. *J Biomech*. 1994; 27(4):421-31
- 7 59. MA Kessler, C Glaser, S Tittel, M Reiser, AB Imhoff. 2008. Recovery of the Menisci and Articular Cartilage of Runners After Cessation of Exercise: Additional Aspects of In Vivo Investigation Based on 3-Dimensional Magnetic Resonance Imaging. *Am J Sports Med* 36(5) 966-70
60. B Day, WG Mackenzie, S Shik Shim, G Leung. 1985. The vascular and nerve supply of the human meniscus. *The Journal of Arthroscopic and Related Surgery* 1(1):58-62
61. JC Gray . 1999. Neural and vascular anatomy of the menisci of the human knee. *J Orthop Sports Phys Ther*.29(1):23-30
62. P Renstro, RJ Johnson. 1990. Anatomy and biomechanics of the menisci. *Clin Sports Med*; 9(3):523-538.
63. DC Fithian, MA Kelly, VC Mow. 1990. Material properties and structure–function relationships in the menisci. *Clin Orthop Relat Res*. (252):19-31

64. D Kohn, T Mussack, W Plitz. 1993. Material properties of meniscus tissue and the effect of the menisci on the compression behavior of the knee joint [in German]. *Z Orthop Ihre Grenzgeb*; 131(5):397-403.

65. M Lengsfeld, L Rudig, WD Von Issendorff, J Koebke. 1991. Significance of shape differences between medial and lateral knee joint menisci for functional change of position. *Unfallchirurgie*; 17(6):309-315.

66. J Bland-Sutton. 1887. *Ligaments: Their Nature and Morphology*. 2nd ed. London, UK: HK Lewis.

67. TJ Fairbanks. 1948. Knee joint changes after meniscectomy. *J Bone Joint Surg Br*.30:664-70

7.1 68. P Fehrmann, J Mockenhaupt. 1991. Theoretical and experimental analysis of the significance of the intact and damaged meniscus for static stress on the knee joint [in German]. *Unfallchirurgie*; 17(4):187-193.

7.2

7.3 69. A Vaziri, H Nayeb-Hashemi, A Singh, BA Tafti. 2008. Influence of meniscectomy and meniscus replacement on the stress distribution in human knee joint. *Ann Biomed Eng*.

7.4

70. Vedi, Hunt 1999. *Meniscal Motion*. British Editorial Society of bone and Joint Surgery, vol 81-B (1)

7.5

8 71. Y Kawahara, M Uetani, K Fuchi, H Eguchi, K Hayashi. 1999. MR Assessment of movement and morphologic change in the menisci during knee flexion. *Acta Radiologica*, 40(6) 610-4

72. H Erbagci, E Gumusburun, M Bayram, G Karakurum, A Sirikci. 2004. The normal menisci: in vivo MRI measurements. *Surg Radiol Anat.* 2004; 26(1):28-32.
73. Ko Yasura, I Yasuyuki Mizuno, I Yasuaki Nakagawa, et al. 2007. Estimation of the mechanical property of meniscus using ultrasound: Examinations of native meniscus and effects of enzymatic digestion. *J Ortho Res.* 884-93
74. L Weiss, J Silver, J Weiss. 2004. *Easy EMG.* Butterworth-Heinemann Publishers; 1st edition
75. A Ghazzawi. 2006. A 32-channel systems for monitoring and pacing high risk patients of cardiac sudden death. MPhil research. Engineering Department, Cambridge University
76. JP Hornack. 1996. *The Basics of MRI.* Online access (<http://www.cis.rit.edu/htbooks/mri/inside.htm>)
77. CN Chen, DI Hoult. 1989. *Biomedical magnetic resonance technology.* Adam Hilger, IOP publishing LTD
78. BR Friedman, JR Jones, G Chaves-Munoz, AP Salmon, CRB Merritt. 1989. *Principles of MRI.* McGraw –Hill Inc
79. C Belcher, M Doherty, S P M Crouch. 2002. Synovial fluid neutrophil function in RA: the effect of pregnancy associated proteins. *Ann Rheum Dis* (61)379–380

Appendix I:

Literature Review of the Knee Meniscus

I.1 Introduction

The menisci are essential anatomical structures serving important biomechanical roles within the knee joint. The knee meniscus was previously described as "the functionless remains of a leg muscle" [66], as it was susceptible to partial or complete removal during knee surgeries [66,67]. However, initial post-menisectomy studies suggested otherwise and showed that meniscectomy carries damaging long term consequences [50,68,69]. Further biomechanical studies proved a number of biomechanical functions including bearing 30% to 70% of the load applied across the knee joint, shock absorption, joint lubrication, secondary stabilization, and limiting extremes in flexion and extension [62-65,70]. The critical importance of the knee menisci within the knee joint is now understood. The similarities between the functions of KFP and the knee meniscus can speculate they serve similar biomechanical functions. This appendix describes the latest findings in the anatomy and functionality of the knee meniscus.

I.2 Anatomy of Knee Meniscus

I.2.1 Location & Shape

The knee meniscus is a half moon shaped tissue and located between the load bearing joint surfaces of the femur and tibia bones. There are two menisci in the knee joint, the lateral and medial menisci (Figure I.2.1). Both are cartilaginous tissues that provide structural integrity to the knee when it undergoes tension and torsion. They are concavely shaped proximally and flat distally, articulating with the tibia, and triangular shaped in cross section. Towards their centers they are unattached and their shape narrows to a thin shelf [30,60].

I.2.2 Anchorage & Fibrosis

There are a number of ligaments and connective fibers surrounding the knee joint to provide stability, limiting the knee movement and protecting the articular capsule. The ligaments can be described as intracapsular and extracapsular.

- **Intracapsular.** The **Anterior Crutiate Ligament (ACL)** attaches the lateral condyle of femur to the anterior intercondylar area. ACL limits the tibia's anterior motion, relative to the

femur. The **Posterior Cruciate Ligament (PCL)** connects the medial condyle of the femur to the posterior intercondylar area, limiting the posterior motion of the tibia. The **transverse ligament** attaches both menisci to each other anteriorly. The **posterior meniscomfemoral ligaments** (also known as ligament of Wrisberg) anchor the posterior horn of lateral meniscus to the medial femoral condyle. The meniscotibial ligaments stretch from the inferior edges of the menisci to the periphery of the tibial plateaus.

- **Extracapsular.** The **Medial Collateral Ligaments (MCL)** connects the medial epicondyle of the femur to the medial tibia condyle. It consists of three groups of fibers, one stretching between the two bones, and two blend with the medial meniscus [58,62].

I.2.3 Sheaths & Retinaculae

Laterally and medially to the patellar ligament, the lateral and medial patellar retinaculae connect fibers from the vasti lateralis and medialis muscles to the tibia. Some fibers from the iliotibial tract stretch into the lateral retinaculum, while the medial retinaculum is attached to fibers on the medial femoral epicondyle [60,62]. This is suggested to provide a tight seal of the knee joint capsule.

I.2.4 Vascularity & Neural Supply

The blood supply to the menisci of the knee reaches the outer 10% to 33% of the body of the menisci, also known as 'the red zone'. This portion of the menisci is capable of inflammation, regeneration, and remodeling. Neural innervation with nociceptors and type I, II and III mechanoreceptors are found in the outer 66% of the body of the menisci. The anterior and posterior horns of the menisci have a rich supply of both blood vessels and nerves [17,60,61]. Menisci of the human knee are an important source of proprioceptive information regarding the position, direction, velocity and acceleration and deceleration of the knee. Rehabilitation following injury or surgery to the menisci of the knee should, therefore, incorporate a proprioceptive retraining program that respects both the abilities and inabilities of different portions of the menisci to follow through with repair and remodeling.

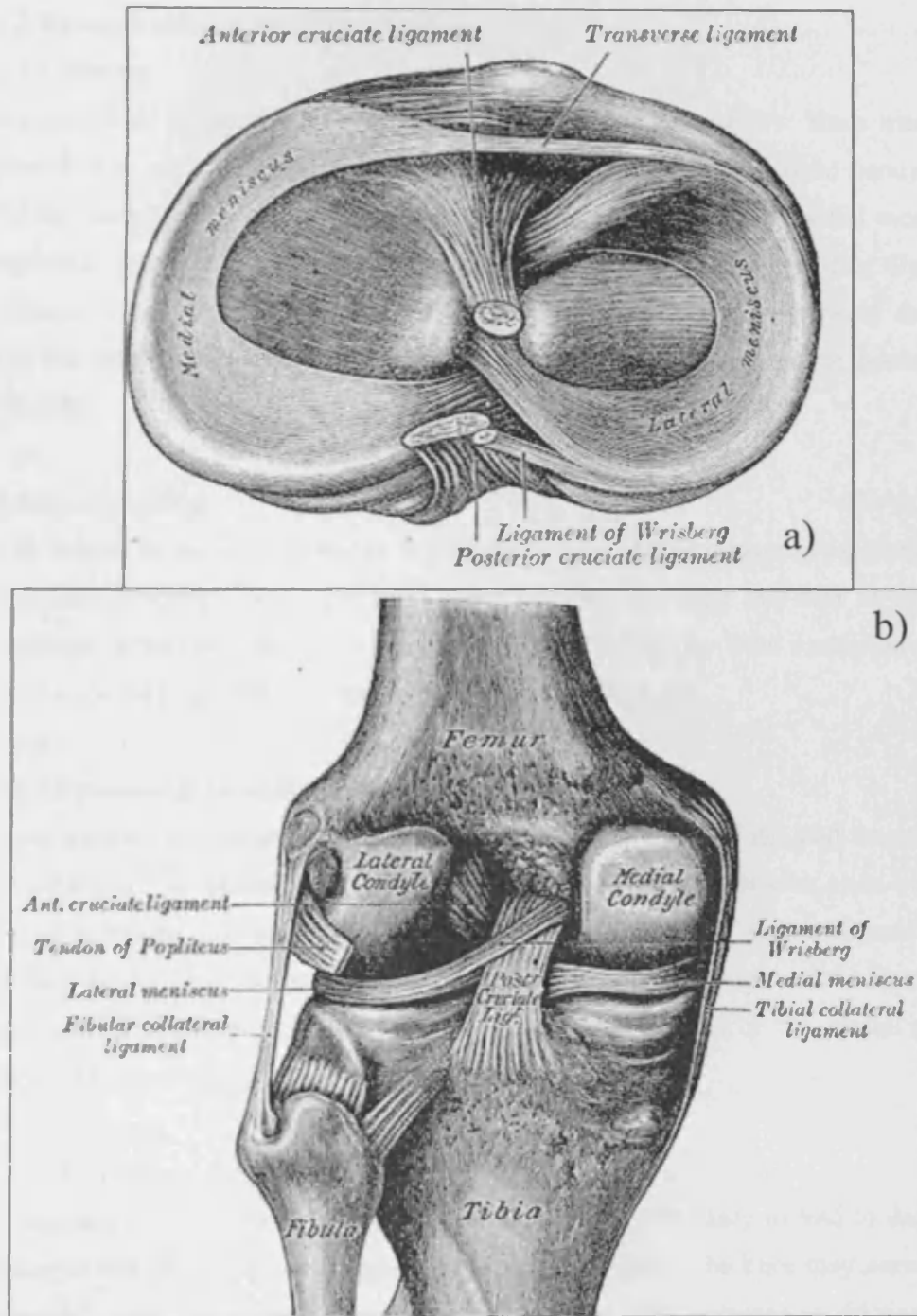


Figure I.2.1: An illustration of the shape and location of the knee meniscus in the transverse plane (a) and Coronal plane (b). Both menisci are anchored to their locations by a number of ligaments. [30]

1.3 Biomechanics of the Knee Meniscus

1.3.1 Motion

Despite their anchorage attachments, both menisci have mobility. Knee menisci were observed to slide anteriorly and posteriorly easily on the lateral tibial condyle surface during knee flexion and extension [57]. The centre region of the medial meniscus was reported to slide approximately 5 mm, while the lateral meniscus's sliding distance may exceed 10 mm [71]. MR images showed both menisci move posteriorly during knee flexion. Sliding distances of the anterior horns is greater than in the posterior horns [71,73].

1.3.2 Lubrication

The motion of the knee meniscus in a synovial fluid soaked capsule is suggested to assist in dynamic lubrication of the knee joint, reducing the wear and tear of the articular cartilage. Meniscal lubrication was shown to be caused by fluid exudation across the surface of the knee meniscus during knee flexion [62,71,72].

1.3.3 Pressure & Load Reduction

Knee menisci are suggested to carry between 40% and 70% of the load across the knee, absorbing a third of the impact on cartilage surface [16]. MRI studies on in-vivo motion of the meniscus showed that the anterior-posterior diameter of each meniscus decreased at knee flexion or under load [73]. The change in shape and volume of the knee meniscus showed 9.8% change in area, and 3.5% and 5.9% in volume on the medial and lateral menisci respectively [59].

1.3.5. Consequences of Removal

It was demonstrated that the loss of a meniscus is highly likely to lead to degenerative changes and can lead to progressive arthritis in the joint. The knee may seem to thrust outwards with each step, 'lateral thrust', causing 20% increase in friction [67,68]. Complete removal of the medial meniscus reduces the tibiofemoral contact area by 50% to 70% and increases the stress across the knee joint by approximately 250 to 300%

[13,69]. Normal knees have 20% better shock-absorbing capacity than meniscectomized knees [63,64].

Appendix II:

Principles of the Electromyogram (sEMG)

II.1 Introduction:

EMG systems are nowadays commonly used in a number of applications to assess the functionality of skeletal muscles. The system simply reads the amplitude and frequency of the muscle electrical activity, applies signal processing techniques to view the signals in a real time or offline viewing. In principle, EMG is identical to ECG and EEG. However, since EMG systems deal with different signal sources, and therefore, different frequencies, amplitudes, and noise sources. EMG systems are widely used during muscle strength diagnoses, surgeries, rehabilitation procedures, and fitness training. EMG signals can be acquired invasively or noninvasively depending on the application in question. For this study, a single channel surface EMG (sEMG) was used and hence this appendix is focused on sEMG implementation, calibration, and testing.

II.2 Physics of EMG

The complete EMG process begins with muscle activities (Figure II.1). The activation of an alpha-motor anterior horn cell (induced by the central nervous system or reflex) results in the conduction along the motor nerve to deliver firing signals, or what's known as Action Potentials, which modifies the potential difference within the muscle fiber membrane from around -90 to +30 mV (Depolarization process). The change in ion flow within the cells causes their potential to repolarize to the resting potential. As illustrated, electrodes pick up the sum of the activities within the fibers of the muscle in question, or what is known as the potential difference between two points along the muscle fibers.

Surface Electromyogram (sEMG) systems are used to measure the activity of the muscle using skin-electrodes in contrast to needle-electrodes used for in-vivo EMG testing. As mentioned above, sEMG measures the neural activity between both electrodes. Previous studies [56] showed that during plantarflexion, the main plantarflexor muscles are active (Gastocnemius, Soleus, FHL, etc) and dorsiflexors were inactive. However, since the FHL is a major neighbour to KFP, a single channel high-gain sEMG device was used to assess FHL's influence on KFP's motion.

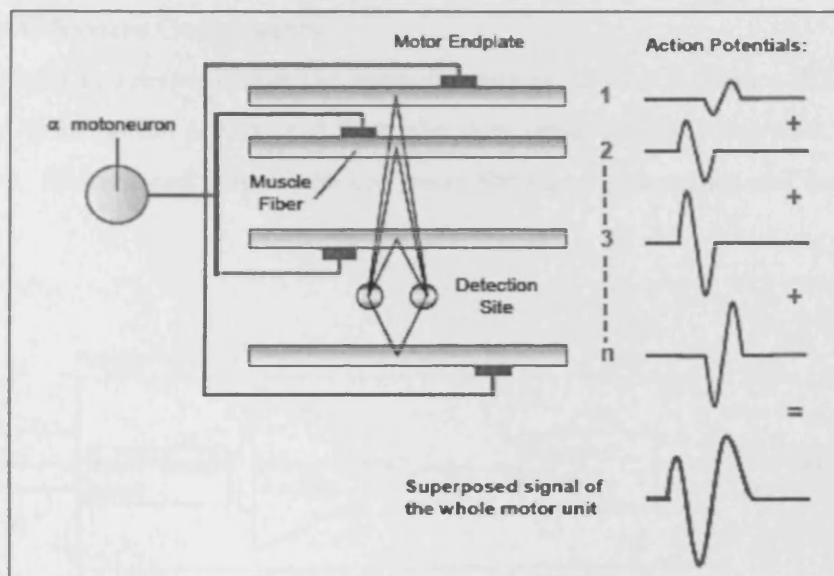


Figure II.1: EMG electrodes pick up signals from the muscle as a whole motor unit, which are generated by motor neuron [74]

II.3 sEMG System Components

Every sEMG system will have the main diagram as shown in (Figure II.2). The muscle electrical information is detected from the skin using bipolar electrodes, this signal is amplified, filtered, and sent to the computer for signal processing and data storing and viewing.

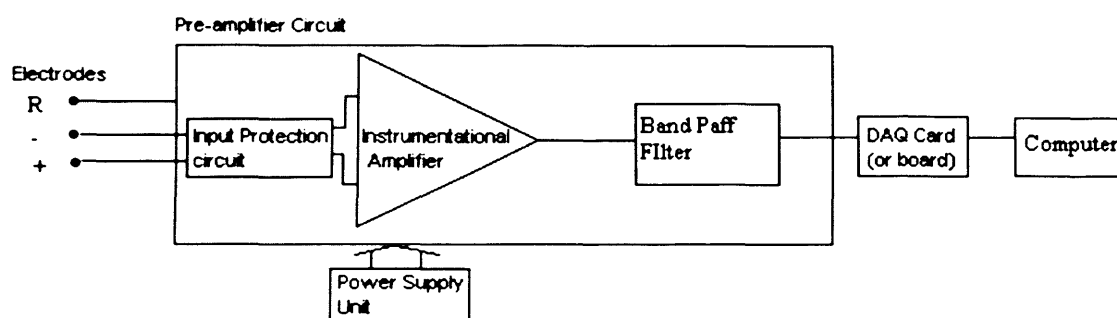


Figure II.2: The EMG signals are measured by bipolar electrodes (+ & -), which are then amplified at high gains, filtered against unwanted noises, and received by the LabVIEW coded computer via a data acquisition card. A reference electrode (R) was used to stabilize the EMG signals around the baseline.

II.3.1 Electrodes

The choice of the electrode generally depends on the application. A number of electrodes were considered for this study. Initially, ECG type electrodes were used, however low conductance was experienced as the electrode was designed for the higher voltages produced by the heart. The presence of sponge-like material to soak great amount of conductive gel produced a large separation gap between the skin and electrode. A selection of sEMG specialised electrodes were tested later and found to conduct better and produced consistent output values. The impedance of sEMG electrodes was tested by connecting to an ohmmeter. EMG type electrodes showed impedances of within 100 and 300 Ω where the ECG electrodes used has impedances higher than 1 k Ω .

From the acquired data using different electrodes, this application made most use of sEMG electrodes named EM2300 that have a metal core and pre-gelled, from (Physio-Med Ltd.) (Figure II.3.A).

II.3.2 Input Protection

Input Protection circuits' sole function is to protect both the volunteer and the circuit from electric shocks caused by static. For the volunteer safety, no signals are allowed to be sent to the volunteer unless being controlled as part of the test [BN 60601, ISO 13485]. For the electronic circuits, static charges and signals that are beyond the components' limits can damage the performance of the circuit and therefore invalidating the system. Ideally, an input protection circuit limits the signal with high amplitudes from being transferred from input to output or vice versa without attenuating valid signals. Initially, the input protection circuit designed consisted of zener diodes limiting any signals above 4.8 V to be transferred between skin and preamplifier unit. However, in addition to the zener diodes' off set signal reduction that is expected, this was acting as a low pass filter with a high cut off frequency (2.4 kHz) which led to important data loss. Modifications to the circuit were necessary. Hence, the chosen preamplifier chip included an integrated input protection circuit that does not act as a filter, with zero signal reduction (data sheets attached at the end of appendix II), which eliminated such problems.

II.3.3 Pre-Amplifier

The INA114AP instrumentation amplifier chip was chosen since it is designed for medical applications (data sheet attached), and has the following specifications:

- Bipolar input to read low level signals (1 mV max, typically in μV especially as FHL-skin contact area is limited) in a noisy environment.
- Very high input impedance ($> 10 \text{ G}\Omega$) to minimise the differential pickup due to mismatches in skin contact impedance.
- Common-mode rejection ratio of 115 dB
- Gains of up to 10,000, which is controlled by the value of one resistor component
- Integrated input protection circuit that does not attenuate the input signals

- Low operating power supply (+/-2.25-15 V)
- Maximum input is 6 mV, six times higher than the maximum expected amplitude

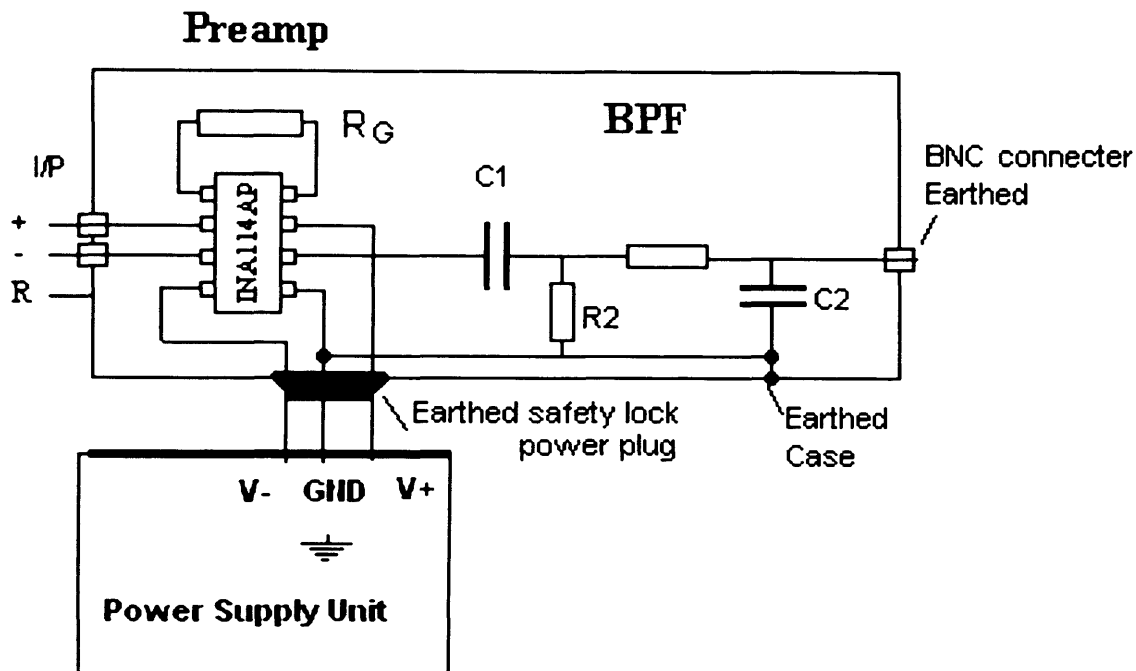


Figure II.4: Circuit Diagram of the sEMG preamplifier unit. INA114P has an integrated input protection circuit as well as the instrumentation amplifier. Changing only one resistor (R_G) is required to control the gain to up to 10,000. An analogue band pass filter (BPF) was used to reduce power consumption. The preamplifier unit is contained in an aluminium case for noise reduction. The power supply (Farnell, 30 Vp-p) was provided from the School of Engineering, Cardiff University

When the pre-amplifier prototype was first tested, the output signals were showing instability in amplitude, and had the tendency to threshold and baseline offset, leaving the output consistently inaccurate. To correct the error, a reference electrode was added and connected to the common ground rather than using one of the active electrodes (Figure II.1.B).

To calculate the price of the sEMG preamp unit, shown below, the parts used are:

- INA114AP integrated chip, instrumentation amplifier **£6**
- Nylon Screws for isolation ..
- Capacitors 0.1 uF and 10 uF ..
- Resistors 2x20 k and 5.6 , in addition to above 2 **£1**
- BNC connectors x3 **£6**
- Aluminium casing **£10**
- Power Supply Unit (already available for the research)
- Earthed Power supply plug & socket **£6**
- Machinery (case drilling) **£5**
- Cabling (3 m coaxial and inter circuit cabling) **£3**
- **The overall cost of the pre-amp is: Approximately £38**

More costs were encountered during the steps of redesigning and other components orders. Also some parts were already available (power supply, which would cost highly unless a battery is used instead with a voltage regulator, adding around £10) or acquired as promotional samples (electrode clip cables, which would cost £30 alone). The overall cost can reach £80.

II.3.4 Band-Pass Filter

One of the main steps to improve signal to noise ratio is by eliminating any signals that do not fall within the same frequency band as the EMG signals, which vary between 100 Hz and 1 kHz. High-pass filters remove signals with frequencies below a cut off frequency (100 Hz). Low-pass filters remove signals with frequencies above a cut off frequency (500 Hz). Both filters are found necessary to remove interference with nearby computers and other high frequency operating devices. This sEMG system has an analogue band pass filter (Figure II.5), chosen against the digital alternative for its low power demand and producing efficient results when evaluated (Table II.1). Although analogue component are likely to attenuate the signals, such attenuation is constant across all frequencies. Therefore, using low power components (0.125 & 0.25 W) and high voltage power supply minimizes this reduction.

II.3.5 Data Acquisition

To transfer the measured signals from the preamplifier circuit to the computer for signal processing (online or offline processing) a data acquisition card is required. The card used (Data Translation USB 9800 series) allowed connection to the preamplifier circuit via BNC connectors, and to the computer via USB 2.0 port (Figure II.6). As the signal processing codes were programmed using LabVIEW, an add-on file was installed into the LabVIEW software to allow the card acquired compatibility with LabVIEW package.

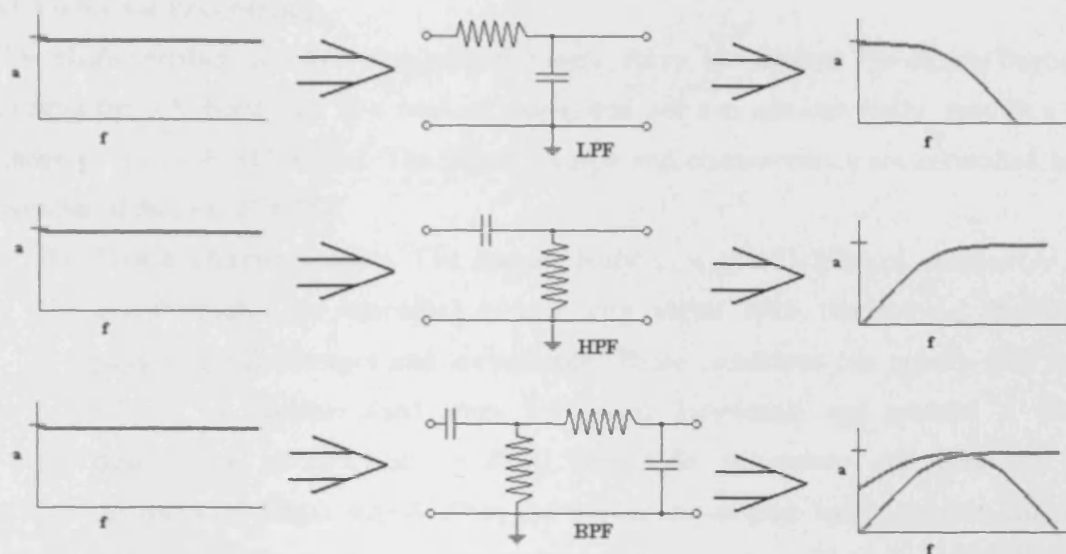


Figure II.5: Low pass filters (LPF) attenuates the amplitude of signals (a) exponentially with frequency (f). The high pass filter (HPF) reduces amplitude of signals below a certain cut off frequency. Band pass filters (BPF) is a combination of LPF & HPF, which leads to reducing signals that are outside the cut off limits. The cut off frequencies for these filters are controlled by the component values used.

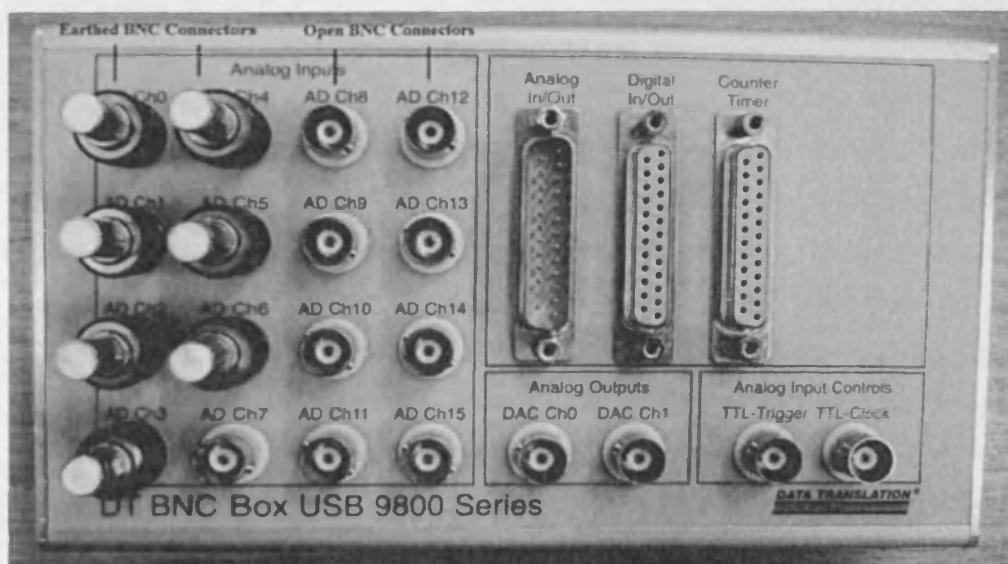


Figure II.6: The DAQ card used is a Data Translation USB box (9800 series). To reduce possible crosstalk between used and open ports, possible noise open ports were earthed

II.3.6 Signal Processing

The characteristics of EMG data indicate timing, force, and fatigue. The signals fluctuate around the 0 V base-line in a random shape, and one can not identically reproduce the shape of a raw EMG signal. The signal's shape and characteristics are controlled by a number of factors: [74,75]

- 1) **Tissue characteristics** The human body is a good electrical conductor, but unfortunately the electrical conductivity varies with tissue type, thickness, physiological changes and temperature. These conditions can greatly vary from subject to another (and even within an individual) and prohibit a direct quantitative comparison of EMG amplitude parameters calculated on the unprocessed EMG signal. Also, the thicker the adipose tissue between the skin and muscle, the higher the signal attenuation.
- 2) **Physiological cross talk** Neighbouring muscles may produce a significant amount of EMG that is detected by the local electrode site. Typically this does not exceed 10%-15% of the overall signal contents or is not available at all. However, care must be taken for narrow arrangements within muscle groups.
- 3) **Changes in the architecture between muscle belly and electrode site** Any change of distance between signal origin and detection site will alter the EMG reading. It is an inherent problem of all dynamic movement studies. For this study, no literature found suggested this problem exists for the FHL or any ankle plantarflexion muscles. This can cause the signals to fluctuate away from the baseline. This can be corrected by correct positioning of the electrodes and an automatic baseline detector code in the software for signal processing.
- 4) **External noise** The most demanding is the background power noise, typically produced by surrounding power cables (even inside walls). This can be avoided by correct grounding and using a reference electrode. Since EMG signals are carried at higher frequencies than 50Hz, any parts between the skin and the band pass filter circuit were found unnecessary to earth as the filter will eliminate this noise. Also the signal processing software included a noise reduction code that eliminates the 50-60 Hz noise.

Most of these factors can be minimized or controlled by accurate preparation and checking the given room/laboratory conditions. Once a raw EMG waveform is obtained, a number of signal processes are applied. Full wave rectification is the first, followed by averaging, then finally calculating the mean and smoothing of the signal, as illustrated below, to view results in a single line style graph.

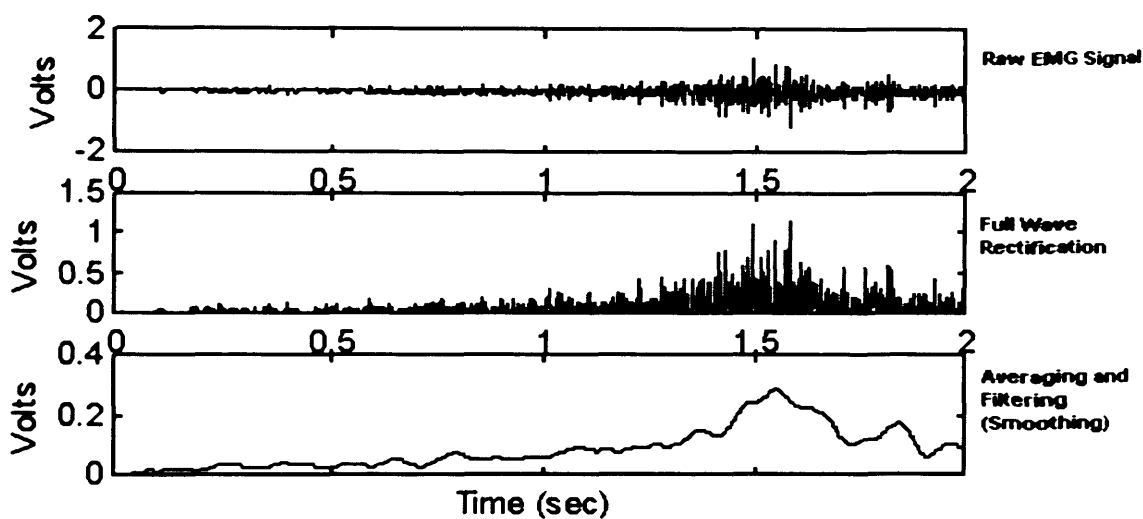


Figure II.7: Raw EMG signal seems to fluctuate randomly around the baseline. Full wave rectification replaces the negative signal values with positive values, this typically doubles the amplitude if fluctuation is identical around the baseline. Finally, smoothing is carrying out to give the wave a single line appearance for easier information subtraction.

A LabVIEW software was implemented for real-time signal processing, data storing, and the graphical user interface (GUI). LabVIEW is known for its visual-based icon-coding as opposed to the usual line coding. The implemented software (Figure II.8) carried out the following processes;

- Reads data continuously at of 1000 per second to minimized data loss
- For each sample, the absolute value is obtained, as well as average
- Signal rectification, and waveform smoothing is then produced
- A waveform chart is then produced
- Data is stored in a text file format along with the volunteer's details

The software code's main function is to read the data at 1kHz. This was achieved by modifying an existing LabVIEW code offered by National Instruments, namely "Analogue Input, Continuous". The correct channel was specified. The output is then passed through full wave rectification and averaging techniques, already available within LabVIEW package. The output is then saved in real-time to a text file for offline processing and viewing. Prior to every test, the user will be prompted to enter the test and volunteer details. The software produces a time stamp within the data file reflecting the exact start time. This was calibrated to match the US imaging time stamp, to time connect images with the relevant EMG data.

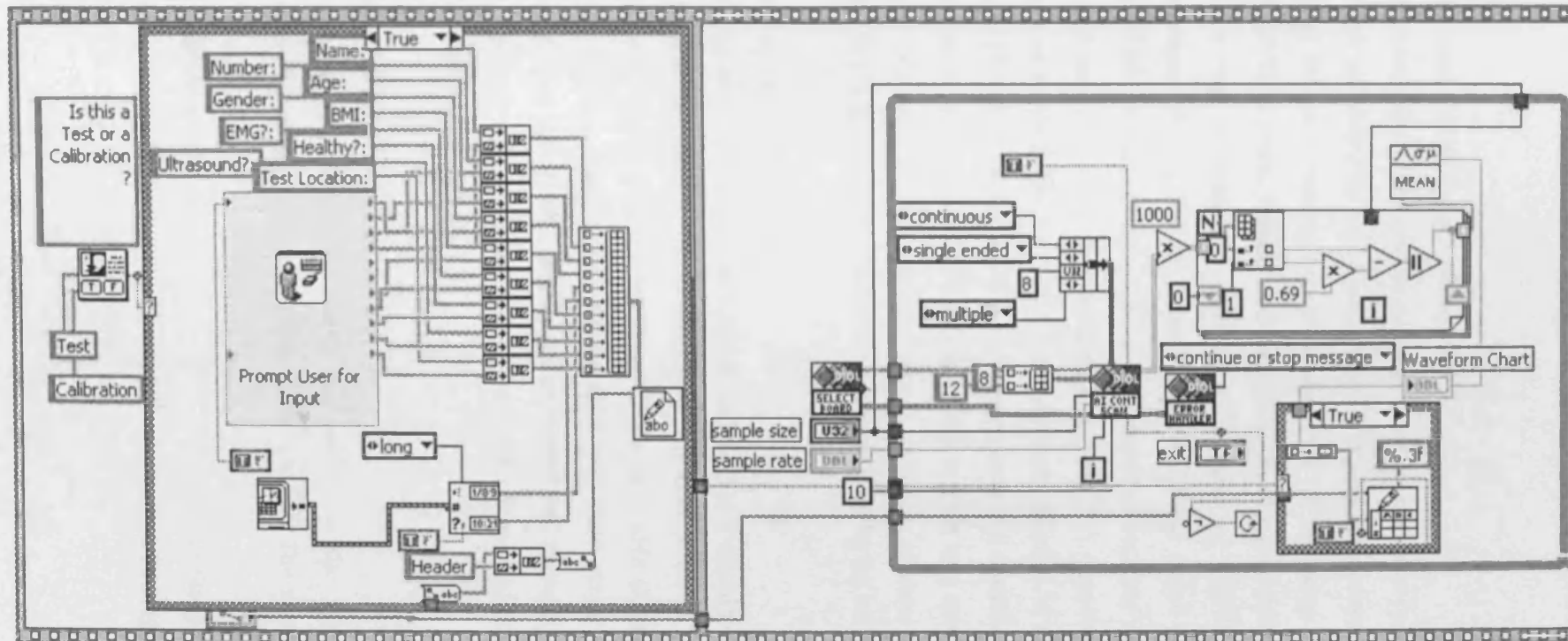


Figure II.8: LabVIEW code used for the sEMG system. Initially, volunteer's details are entered to save on a file. Data is acquired at 1 kHz, rectified, averaged, smoothed, and saved into disk using established LabVIEW codes offered from National Instruments.

II.4 Testing

II.4.1 Accuracy and Calibration

The Preamplifier unit was connected to a digital wave generator to produce 1 mV square wave. Tested and calibrated by the manufacturer (Farnell), the generator was also tested by connecting it to the computer and measuring the output using a LabVIEW code provided by LabVIEW team. Results showed the generator produced 1.00 mV signals. The preamplifier was calibrated to produce a full gain of 10,000 for signals with frequencies between 100 and 500 Hz. Since the accuracy and nature of EMG waves are not the focus of this study, and this system demonstrated accuracy and consistency in detecting muscle activities made this system sufficient. It is known that EMG data is typically travels at around 300 Hz [74]. The system produced 9 V signals from 1 mV input at 300 Hz (Table II.1). Figure II.9 shows measurement consistency is better than 95% when the test was repeated 5 times. The sEMG system was synchronised with the US scanner and calibrated prior to testing for each volunteer to ensure consistent power supply voltage. The output voltage scale is set automatically by the software.

II.4.2 System Consistency Testing

The same accuracy test was carried out 5 times, and the 1 mV signal was identical in all 5 repeats. For output testing, the wave generator was connected to the sEMG system producing sine waves with frequencies from 20 Hz to 1 kHz (Figure II.9). The gain calculated from the data sheet equation (attached) was 9930 (Gain resistor = 5.6 Ω). Since the Preamplifier chip (INA114PA) was calibrated and tested by the manufacturer (data sheet attached) it was found necessary to test the effect of adding the other sEMG components on the IC performance.

II.4.3 Health and Safety

The sEMG system was tested for health and safety at the Medical Engineering Department, Cardiff and Vale Hospital NHS Trust, Cardiff. The system passed the test with the following results.

- Earth Bonding = 0.19 Ω
- Earth Leakage < 168 μA
- Insulation > 100 M Ω
- Patient Leakage = 4 μA

Wave generator Input (mV)	Input frequency (Hz)	IC output (V)	System output (V)
1	20	9.8	1.2
1	50	9.9	1.8
1	70	9.9	3
1	90	9.9	6
1	100	10	7.5
1	150	10	7.9
1	200	10	8.5
1	250	10	8.9
1	300	10	9
1	350	9.9	9
1	400	9.9	8.8
1	500	9.9	8
1	1k	9.8	1.8

Table II.1: IC and system outputs were measured using an oscilloscope when input was 1mV at different frequencies. Preamplifier integrated chip (IC) output is stable throughout the test at 9.9-10V. Filtered signals (system output) were within 3db of the highest amplitude between 100 and 500 Hz Illustrated in Figure II.9

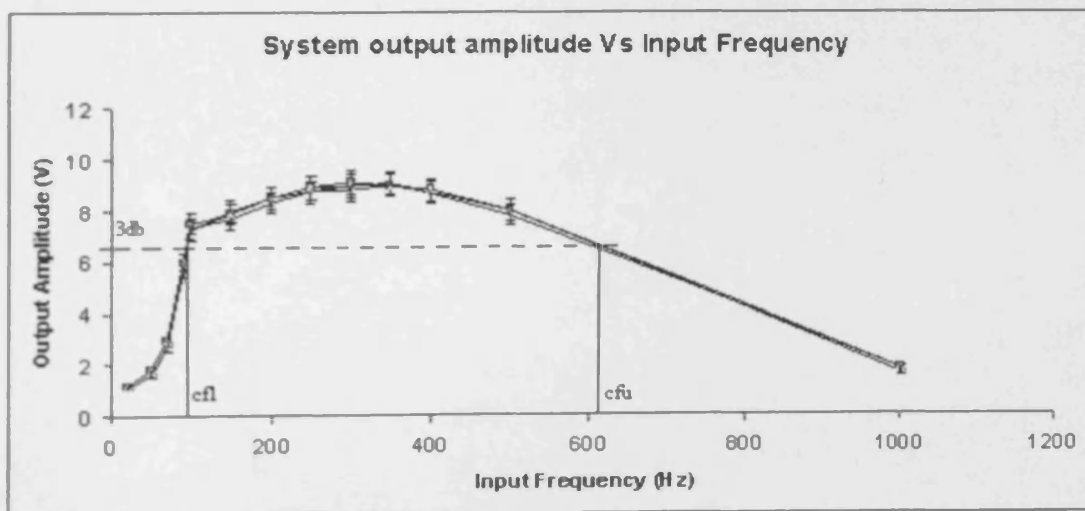


Figure II.9: Preamplifier's consistency test showed maximum variation of 3.5% (maximum variation of 0.2 V was recorded at 100 Hz. 3 db line drawn (6.4 V) shows band pass filter's cut off frequencies are 100 Hz (cfl) and 610 Hz (average) as the upper cut off frequency (cfu)

Appendix III:

Principles of Ultrasound Imaging

III.1 Introduction

Ultrasound (US) imaging is a form of non-invasive and radiation-free imaging. The concept behind US imaging is based on echolocation scanning techniques already used in Radar and sonar systems. Using a probe to transmit and receive (transducer), US imaging systems transmit a series of radio frequency (RF) sound waves and receive the echoes of such waves to analyse information about the surrounding tissues.

Sound waves at RF level have different properties than at audible levels. RF sound waves travel in straight lines, unlike audible sound that can travel around corners (sound diffraction). Because of the shorter wavelengths, RF sound waves are reflected by smaller objects, allowing sounds to give accurate spatial information about the surrounding structures.

III.2 Components of US systems

A typical US system will consist of the following parts;

- **Transducer Probe** – A probe that transmits and receives the sound waves
- **Central Processing Unit (CPU)** – A computer to carry out the calculations, contains the electrical power supplies for the system, displays the images recorded, and stored data for offline processing.
- **Transducer Pulse & Processing Controls** – A control panel is essential to change the amplitude, frequency, and duration of the pulses emitted from the transducer probe, in addition to controlling the image depth, resolution, brightness, and other parameters that the user can modify depending on the application.

III.3 Physics of US Imaging

Ultrasound systems utilize piezoelectric crystals to generate the US pulses. They are compressed and decompressed by changing the current applied through the crystal. The same crystals can receive reflected RF sound waves. The wavelength λ is inversely related to the frequency f by the sound velocity c :

$$c = \lambda f$$

Or;

$$\lambda = \frac{c}{f}$$

In concept, transmitted RF waves are partly reflected from a boundary between any two tissue structures, and partially proceeding through the boundary (Figure III.2). The magnitude of reflected wave depends on the impedance difference between the two tissues. The reflecting boundaries do not reflect waves directly back to the transmitter, but scatters the ultrasound in more directions.

The acoustic impedance of a medium is calculated by the speed of sound (c) in the material and the material's density (ρ):

$$Z = c \times \rho$$

The time lag, τ , between emitting and receiving a pulse is the time it takes for sound to travel the distance to each boundary and back (twice the distance), r , to the boundary at the speed of sound, c , in the tissue. Thus:

$$r = \frac{c \tau}{2}$$

A 2-D image is constructed by first firing a beam vertically, collecting information from returning echoes, and then firing the next vertical beam along the transducer. In a linear array of ultrasound crystals, the beams are fired in a parallel manner. The linear array gives a large probe surface (footprint) and near field, and a narrow sector. The shape of the transducer determines the field of view and the acquired image. Hence, this is important for the user to choose the correct transducer and setting including depth, resolution, brightness, and other factors to enhance the acquired image. Increasing the signals frequency increases the overall resolution but reduces the effective depth (as tissue acoustic impedance increases). CPU applies signals processing techniques to analyze the received US data and construct a 2D image (Figure III.3) that can be shown on real-time display and stored for offline processing.

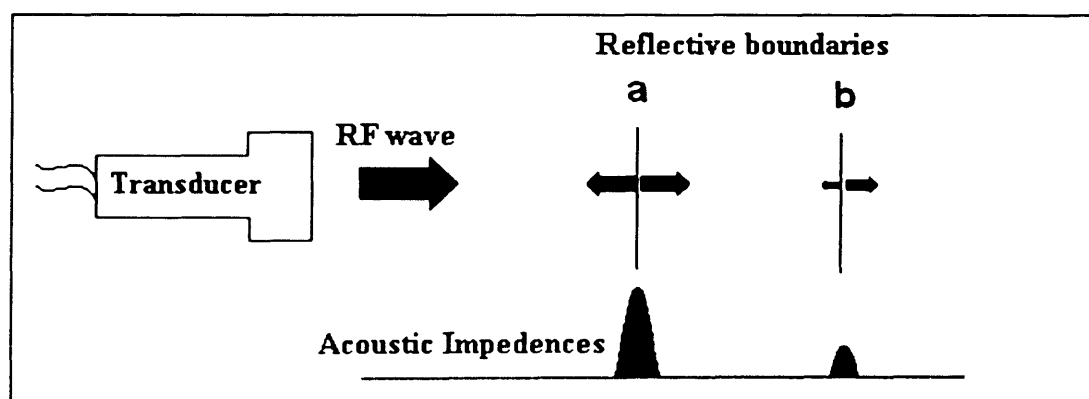


Figure III.2 A schematic illustration of US wave's reflection. A certain amount of the RF wave emitted by US transducer is reflected at tissues boundaries (a) & (b). Part of the pulse energy is transmitted from (a), the rest is transmitted through to the next boundary, (b). When the pulse returns to the transducer, the reflected pulse gives a series of information about the amplitude of the reflected signal, and the travel time. The amplitudes of received data reflect the acoustic impedance of the boundary and the locations of such boundaries.

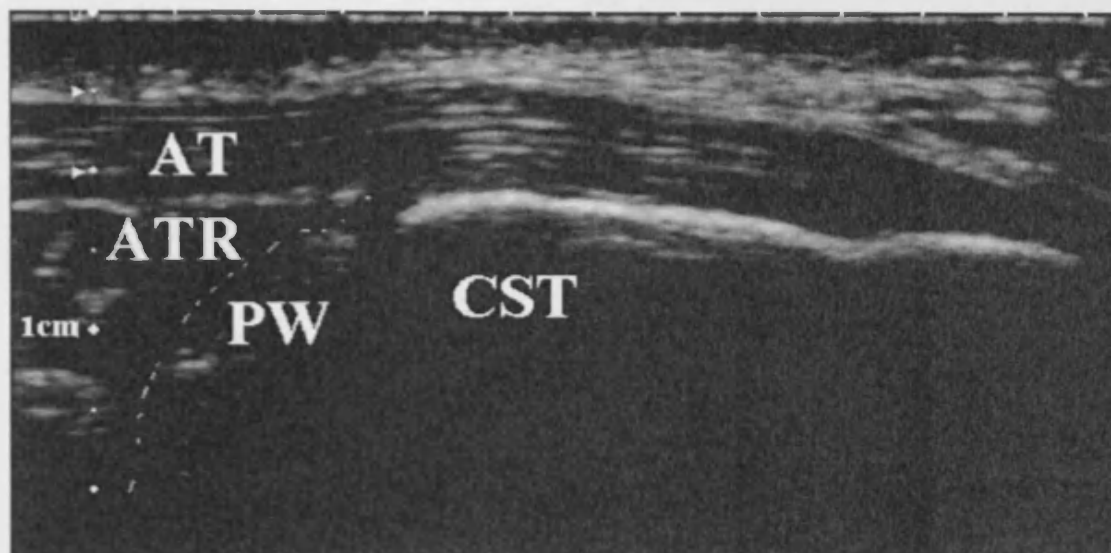


Figure III.3 An US images scanned in the sagittal plane of Kager's fat pad. US imaging can show obvious boundaries between tissues allowing tissue recognition. AT = Achilles tendon, ATR = Achilles tendon related fat pad, PW = the protruding wedge, CST = Calcaneal superior tuberosity.

Appendix IV:

Principles of Magnetic Resonance Imaging (MRI)

IV.1 Introduction

Magnetic resonance imaging (MRI) is a form of scanning that uses strong magnetic fields and radio frequency waves (RF) to produce detailed images. MRI is used in a range of applications including diagnostics of the human body, material content and properties testing, and excavations. MRI is considered safe for its radiation free concept compared to computer tomography (CT) scanning. Using strong magnetic fields increased the safety requirements to remove all metal objects including any medical implants. Therefore, in A&E conditions where information about metallic components is scarce, MRI is not used. This PhD utilized a 0.2 T scanner at Cardiff and Vale Hospital NHS Trust, Cardiff in efforts to reconstruct a 3 D model of KFP in-vivo during ankle flexion. As results were inconclusive, a 3 T scanner at CUBRIC, School of Psychology, Cardiff University, was later used on 2 volunteers to confirm the findings.

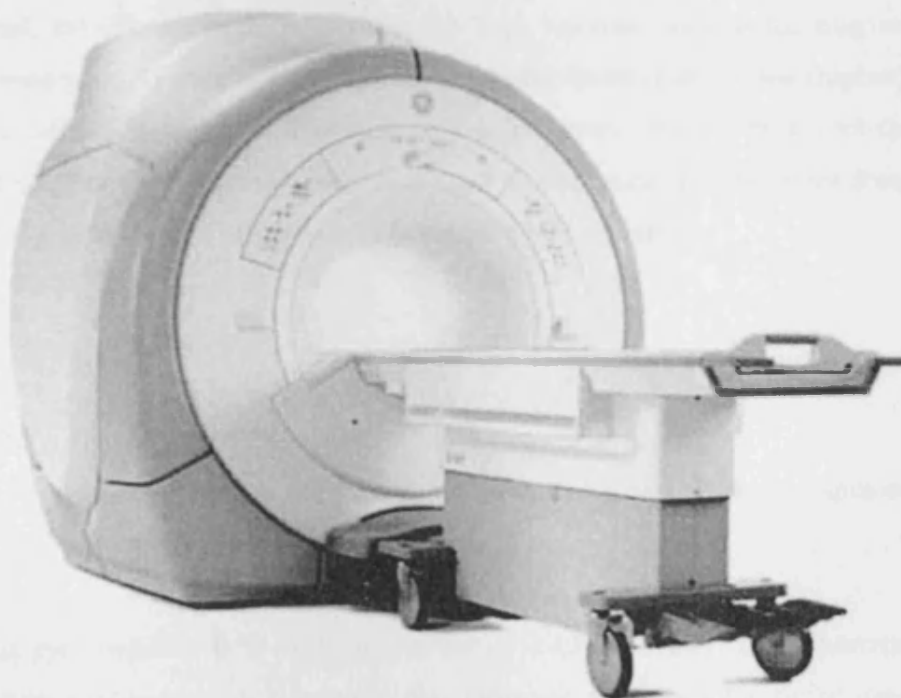


Figure IV.1: The 3T General Electric MRI scanner used at the Cardiff University Brain Research Imaging Center (CUBRIC), at the School of Psychology, Cardiff University.

IV.2 Physics of MRI

MRI produces images from magnetising the hydrogen atoms (protons), and measuring the magnetic properties of the different tissues. Different reactions to the magnetic field and RF signals allow the production of highly detailed images. MR signals are produced from the interaction of RF waves with the atomic nuclei themselves [76]

IV.2.1 Spin Physics and Net Magnetization

MRI is focused on the hydrogen atoms (H), to produce the images. Spin is a quantum physical property, which makes protons behave like small magnets with north and south poles of equal magnetic field strength (Figure IV.2.1.A) [77]. Considering an arbitrary volume of tissue containing spinning protons, the macroscopic behaviour of the tissue is the net of all the microscopic events within it. All protons behave like magnets each having a spin vector of equal magnitude. In the case where all protons are aligned randomly, the net of these spin vectors is expected to be zero (Figure IV.2.1.B). However, when a large magnetic field is applied, protons start to align with the magnetic field, B_0 (Figure IV.2.1.C), where the 'top' wobbles towards the magnetic field. In the presence of B_0 , nuclei either occupy the stable (lower) or excited (higher) energy levels. Out of a million nuclei, there are only a few more low-energy nuclei than high-energy nuclei. Larmor's equation, below, is used to determine the resonance frequency between nuclei spin and the MRI receiver to read the MR signals.

$$f = \gamma B_0$$

Where f = resonance frequency,

γ = the nuclear gyromagnetic ratio that characterizes nuclear species

B_0 = Magnetic field of the scanner

The gyromagnetic ratio for hydrogen nuclei is 42.58 MHz/T. Using Larmor's equation, in the case of using a 1 T scanner; the resonance frequency for signal detection is 42.58 MHz. For the 0.2 T scanner, $f = 213$ MHz. For the 3 T scanner, $f = 14.2$ MHz.

Since each tissue contains a different amount of hydrogen atoms, each has a different relaxation time (explained below in IV.2.2). This enables the MR receiver to visualize the different types of tissues.

IV.2.2 Relaxation

Relaxation is the process in which protons release the energy absorbed and return to their equilibrium magnetization (M_0), when B_0 is applied before firing RF waves. By measuring the relaxation times, images can be obtained since each type of tissue has a different relaxation time. Two methods for measuring the relaxation times are widely used, T_1 and T_2 , which are related to the longitudinal and the transverse components of M_0 (Figure IV.2.1.C).

IV.2.2.1 T_1 Relaxation

Spin lattice (or longitudinal relaxation) is the time required for M_z component (the value of M_0 along the z-axis) to return to 63% of its original value following an RF pulse (Figure IV.2.2.1). T_1 measures the time by which the protons give up their energy to return to the M_0 state. This return happens at an exponential rate, with T_1 being the time constant for this rate. The behaviour as a function of time, t , is governed by the following equation:

$$M_z = M_0 (1 - e^{-t/T_1})$$

In the Microscopic picture, protons in the upper energy level absorb the RF energy, and then stimulating them to emit their energy. As the energy is continuously transmitted, the proton populations of the two levels will equalize. No net energy absorption is then possible (saturation). In the macroscopic picture, M_0 will gradually decrease in magnitude until it disappears. In MRI, time delay is used between repeated RF pulses allowing the excited protons to give up energy (M_0 to return to its equilibrium value)

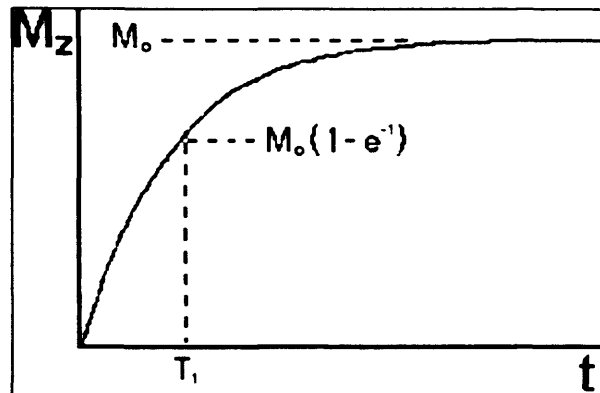


Fig IV.2: T_1 is the time to reduce the difference between the longitudinal magnetization (M_z) and its equilibrium value by a factor of e .

IV2.2.2 T2 Relaxation

Spin-spin (or transverse) relaxation is the time required for M_{xy} (transverse component of M_0) to decay to 37% of its starting value via irreversible process immediately after the 90° pulse. In addition to the rotation, the net magnetization starts to de-phase because each of the spin blocks making it experience a slightly different magnetic field and rotates at its own Larmor frequency [78]. The longer the elapsed time, the greater the phase difference. T_2 describes the return to equilibrium of M_{xy} and can be measured by,

$$M_{xy} = M_{xy0} e^{-t/T_2}$$

The value of T_2 is usually less than or equal to T_1 . The net magnetization in the XY plane goes to zero and then the longitudinal magnetization grows until M_0 aligns with the z-axis.

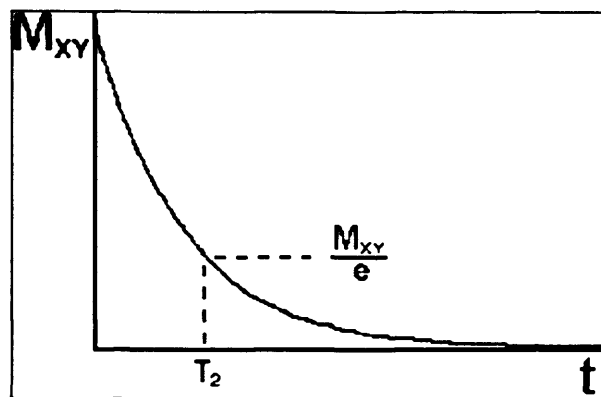


Figure IV.3: T_2 is the time which describes the return to equilibrium of the transverse magnetization by a factor of e .

IV.2.3 Spatial Encoding

To create an image from an arbitrary volume of tissue, MR signals from the nuclei contain information about the nuclei's positions within the tissue. Signal processing is used to decode the measured data. Magnetic field gradients are used to limit the spatial region being excited. In other words when applying an RF pulse with the presence of a field gradient, the magnetic field and resonance frequency change with position (slice selection). When a gradient is applied, a range of frequencies can be obtained as the resonance frequency varies in position with the strength of the signal depending on the number of spins which resonate at that frequency. To obtain the full image, back projection process is applied to change the direction in which the gradient is applied. A pulse sequence is a configuration of the RF pulses, which can be changed by the user depending on the application

IV.3 Basic MRI Instrumentation

This section briefly explains the basic elements that make the MRI scanner.

IV.3.1 Magnets

The operating magnetic field strength reflects the size of the MRI scanner. There are three widely common types of magnets used in MRI.

Permanent Magnets consist of permanently magnetized iron alloy and require neither cooling nor electrical power to operate. However, temperature effects are likely and care is required to achieve sufficient field stability. Permanent magnets are normally made of low field magnets (0.2-0.5 T).

Resistive or 'electro-' Magnets require water cooling to remove excess heat generated in the coils. The field can be removed by switching off the electrical power. The stability of resistive magnets depends upon the winding achieving thermal stability.

Superconductive Coils are cooled close to absolute zero temperature (-273°C). At this temperature, the coils lose their electrical resistance and can support current indefinitely and, once established, without a power supply. Provided the coils are kept sufficiently cool, the magnetic field persists continuously. Liquid Helium is typically used to cool the coils.

IV.3.2 Magnetic Field Gradient

Gradients localize MR signals in the body by generating short term spatial variations in magnetic field strength. The unit of which the gradient field is measured is milli-Tesla per meter (mT/m) and Tesla per meter per second (T/ms) is the rate of change of gradient strength. Gradient fields are produced by the flow of current from an amplifier through the gradient coil. The response of a gradient coil to an input current is not instantaneous. A finite time (0.5-1.0 ms) is required for the gradient to achieve its final value. Stronger gradient strengths and shorter rise times allow smaller anatomical details to be viewed, which means thinner slices and thus smaller voxels and pixels.

IV.3.3 RF System

RS systems consist of RF transmitters and receivers. The transmitter coils generate the RF pulses for excitation, the MR signals used to produce images are stimulated from within the subject's tissue using RF pulses. Receiver coil detects the MR signals. The frequency of RF waves should be calibrated regularly to detect the most amount of MR signals.

IV.4 Safety checks

A typical safety check is carried out prior to every MRI scan to ensure no volunteer safety jeopardy or MRI signal contaminating components are present during testing. (A typical MRI safety check document used for this study is attached at the end of this appendix).

IV.5 Scanners used for this research

This PhD research used 2 MRI scanners. Both are owned by the different institutes of the Cardiff University. They both are regularly calibrated by their suppliers in addition to the regular phantom scanning carried out by the researchers of such institutes.

Institute of Medical Engineering and Medical Physics, Cardiff and Vale Hospital;

- 0.2 T magnetic field strength
- Maximum field of view = 12 X 12 cm
- Minimum slice thickness = 5 mm
- Minimum slice gap (gap between 2 consecutive slices) = 1 mm

Cardiff University Brain Research and Imaging Centre (CUBRIC);

- 3 T magnetic field strength
- Maximum field of view = 48 X 48 cm
- Minimum slice thickness = 1.5 mm
- Minimum slice gap = 0 mm

Quantifying the Motion of Kager's Fat Pad

Ahmad Ghazzawi, Peter Theobald, Neil Pugh, Carl Byrne, Len Nokes

Institute of Medical Engineering and Medical Physics, School of Engineering, Cardiff University, The Parade, Cardiff, South Glamorgan CF24 3AA, United Kingdom

Received 12 September 2008; accepted 16 March 2009

Published online 24 April 2009 in Wiley InterScience (www.interscience.wiley.com). DOI 10.1002/jor.20900

ABSTRACT: Kager's fat pad is located in Kager's triangle between the Achilles tendon, the superior cortex of the calcaneus, and flexor hallucis longus (FHL) muscle and tendon. Its biomechanical functions are not yet established, but recent studies suggest it performs important biomechanical roles as it is lined by a synovial membrane and its retrocalcaneal protruding wedge can be observed moving into the bursal space during ankle plantarflexion. Such features have prompted hypotheses that the protruding wedge assists in the lubrication of the Achilles tendon subtendinous area, distributes stress at the Achilles enthesis, and removes debris from within the retrocalcaneal bursa. This study examined the influence of FHL activity and Achilles tendon load on the protruding wedge sliding distance, using both dynamic ultrasound imaging and surface electromyogram. Intervolunteer results showed sliding distance was independent of FHL activity. This study has shown the protruding wedge to slide on average 60% further into the retrocalcaneal bursa when comparing the Achilles tendon loaded versus unloaded, consistently reaching the distal extremity. Sliding distance was dependant on a change in the Achilles tendon insertion angle. Our results support a number of hypothesized biomechanical functions of the protruding wedge including: lubrication of the subtendinous region; reduction of pressure change within the Achilles tendon enthesis organ; and removal of debris from within the retrocalcaneal bursa. © 2009 Orthopaedic Research Society. Published by Wiley Periodicals, Inc. *J Orthop Res* 27:1457–1460, 2009

Keywords: retrocalcaneal bursa; Achilles tendon; enthesis organ; Kager's triangle

Kager's fat pad is a mass of adipose tissue located within Kager's triangle. Recognizable as a radiological landmark, the fat pad was subsequently useful in early diagnosis of local disorders.^{1–4} Kager's fat pad is surrounded by the Achilles tendon posteriorly, flexor hallucis longus (FHL) anteriorly, and the superior tuberosity of the calcaneal bone inferiorly. In some cases, the fat pad was observed extending to the soleus muscle.⁵ This position means that part of Kager's fat pad may need to be excised during arthroscopic surgery to provide a clear view of the ankle joint,⁶ despite the consequence of such excision currently being unclear. Recent studies have highlighted the potential biomechanical importance of the fat pad within the Achilles tendon enthesis organ. Histologically, Kager's fat pad has three distinctive parts.⁷ The Achilles tendon-related is anchored to the tendon and is encapsulated by the paratenon; the deep pad is located between the Achilles tendon-related pad and the FHL muscle; the bursal protruding wedge extends from the deep pad over the calcaneal superior tuberosity and forms the anterosuperior wall (synovial folds) of the retrocalcaneal bursa (Fig. 1).^{1,8,9}

Kager's fat pad is still widely considered to serve predominantly as a variable space filler,^{4,6} with hypothesized secondary functions providing a mechanical advantage to the Achilles tendon by moving into and out of the retrocalcaneal bursa during ankle flexion. This motion is thought to increase the lever arm of the tendon.⁴ The pad is contained within a synovial membrane and consists of adipose cells,^{7–9} which allows the protruding wedge high mobility within the Achilles tendon enthesis.^{7,8} It is still not fully explained how Kager's fat pad behaves *in vivo*; however, literature investigating bovine fat pad showed that when removed,

it behaves in motion as a fat tissue.⁷ Kager's fat pad has both neural and vascular supplies, suggesting it provides sensory functions and protection to the tendon's vascular supply.^{7–12} The motion of the protruding wedge is also suggested to minimize pressure changes within the retrocalcaneal bursal space during ankle flexion⁷ and to provide subtendinous lubrication, promoting low wear, suggesting that the pad may provide protection to the tendon.¹³ The motion has also been suggested to have an immunoprotective role within the retrocalcaneal bursa—removing debris produced by tear and wear of its lining tissues.⁸

Movement of the protruding wedge appears to be the main factor in providing a mechanical advantage to the Achilles tendon, although its characteristics are unclear. Three possible movement mechanisms have been hypothesized⁷: (1) as a consequence of the superior displacement of the calcaneus; (2) the wedge is pulled into the bursa caused by pressure change within the retrocalcaneal bursa; and (3) FHL muscle contractions act to move the fat pad.

We investigated the motion of the protruding wedge by measuring its sliding distance during ankle flexion in healthy volunteers with the aim of establishing obvious influences of the FHL and Achilles tendon load over the protruding wedge sliding distance and examining its hypothesized biomechanical functions within the tendon's enthesis.

MATERIALS AND METHODS

Dynamic ultrasound (US) (with a linear transducer operating at 12 MHz; Toshiba Aplio) was used to measure the protruding wedge sliding distance during ankle flexion in the sagittal plane. Dynamic US imaging was previously used to measure abnormalities and motion distances on Kager's fat pad^{1,6,7,9} and other soft tissue.^{14,15} Still images were extracted from video scans to measure sliding distance offline. Prominent features within the calcaneal superior tuberosity and the Achilles tendon insertion point were used as anatomical

Correspondence to: Ahmad Ghazzawi (T: +44-0-7979853835; F: +44-0-2920874939; E-mail: ghazzawiaa@cardiff.ac.uk)

© 2009 Orthopaedic Research Society. Published by Wiley Periodicals, Inc.

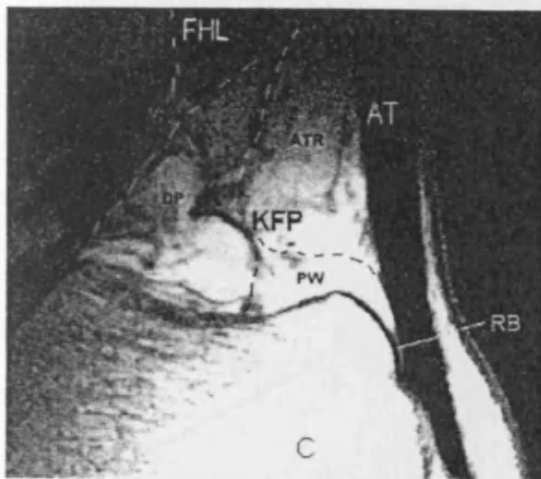


Figure 1. Sagittal MRI of Kager's fat pad at the Achilles tendon (AT) midline. Lines identify the pad's three parts: AT-related (ATR) pad is connected to Achilles tendon; the deep pad (DP) is a continuation of ATR and is inferior to FHL muscle; and the retrocalcaneal protruding wedge (PW) extends from the superior cortex of the calcaneus (C) to the superior wall of the retrocalcaneal bursa (RB).

landmarks to measure sliding distance consistently (Fig. 2). A pilot study was performed on five subjects by repeating the study five times to determine the protocol's consistency and accuracy. Sliding distance had a variance coefficient of less than 0.125. Also, the pilot test was extended to examine the location and the angle of the US probe against the Achilles tendon using a manual goniometer. If the US probe was located near the tendon midline ($\pm 25\%$ of the tendon's width) and was aligned with the long axis of the foot ($\pm 40^\circ$), the sliding distance variation coefficient was less than 0.125. As the calcaneal superior tuberosity can differ in shape,¹⁶ a skin marker was used to locate tendon midline for consistent US scans. US images were scanned by the same researcher to minimize human error.

The hindfeet of 25 healthy volunteers (eight females and 17 males, age 20–57, BMI 19–29) were scanned. FHL activity was monitored using a surface electromyogram (sEMG). US and sEMG data were time-stamped to ensure synchronized offline processing. The test was devised into four parts to establish the influence of FHL and loading of the Achilles tendon on sliding distance:

1. FHL only (without ankle flexion). Subjects stood with a double foot stance on a step with the big toe suspended



Figure 2. Sagittal dynamic US of the protruding wedge during plantarflexion (left) and dorsiflexion (right). The protruding wedge sliding distance was measured from the Achilles tendon insertion point using surrounding prominent anatomical landmarks. +, The wedge's tip; x, Achilles tendon superior insertion point; *, calcaneal superior tuberosity; AT, Achilles tendon; C, calcaneus. Scale is 1 cm.

over the step. Subjects flexed their big toe through the full range of flexion.

2. Passive ankle flexion. Subjects lay prone on the examination bed allowing unrestricted ankle flexion. An assistant placed an open palm on the subject's dorsum to fully flex and extend the subject's ankle repeatedly, through the full range.
3. Active ankle flexion. Subjects lay prone, with their knees fully extended. Subjects actively flexed and extended their ankle through its full range.
4. Loaded ankle flexion. Subjects stood in a single foot stance on a step. Subjects fully flexed and extended their ankle, overcoming the resistance of body weight. A grip was available for balance support.

The first 10 volunteers underwent the same protocol on both ankles to identify any contralateral variations; this was also performed with the knee flexed at 90° and 180° to identify the potential influence of gravity.

RESULTS

During ankle plantarflexion, some observations were common across all individuals: (1) the Achilles tendon-related pad shifted upwards; (2) the deep pad moved downwards; and (3) the protruding wedge slid over the calcaneus into the bursal space. These movements were reversed during dorsiflexion. After testing the first 10 volunteers, contralateral results showed no significant difference ($p = 1.0$). Additionally, protruding wedge movements were independent of knee flexion angle and subsequent Kager's fat pad orientation.

During FHL only, sEMG data showed FHL activities during toe flexion; however, no protruding wedge motion was observed. The wedge only seemed to move when the Achilles tendon insertion angle changed. The deep fat pad was observed to move as the FHL contracted. Throughout passive ankle flexion, the wedge slid a distance of 1.5 to 9 mm (mean = 4.8 mm, SD = 1.6 mm). sEMG data showed no consistent FHL activities. During active ankle flexion, the range of sliding distances reached distances between 2.5 and 11 mm (mean = 7.4 mm, SD = 0.8 mm). The protruding wedge moved to within 2.5 to 5.5 mm of the most proximal point of the Achilles tendon insertion. FHL activities were observed during ankle flexion. Through loaded ankle flexion, the sliding distance reached 3.5 to 17.5 mm (mean = 11.2 mm, SD = 3.33 mm). The distance between the tip of the protruding wedge and the most proximal point of the Achilles tendon insertion reduced to 0.5 to 2 mm. FHL sEMG activities were on average 20% greater than during active ankle flexion.

Calculating the correlation coefficients of result groups and comparing readings using Wilcoxon matched pairs test showed no significant difference between protruding wedge sliding distance and BMI, weight, height, age, or gender (in passive ankle flexion, active ankle flexion, and loaded ankle flexion) (Fig. 3A–F). The wedge slid further when the Achilles tendon was loaded as opposed to unloaded ($r^2 = 0.84$), with the distances in the two groups being significantly different ($p < 0.01$).

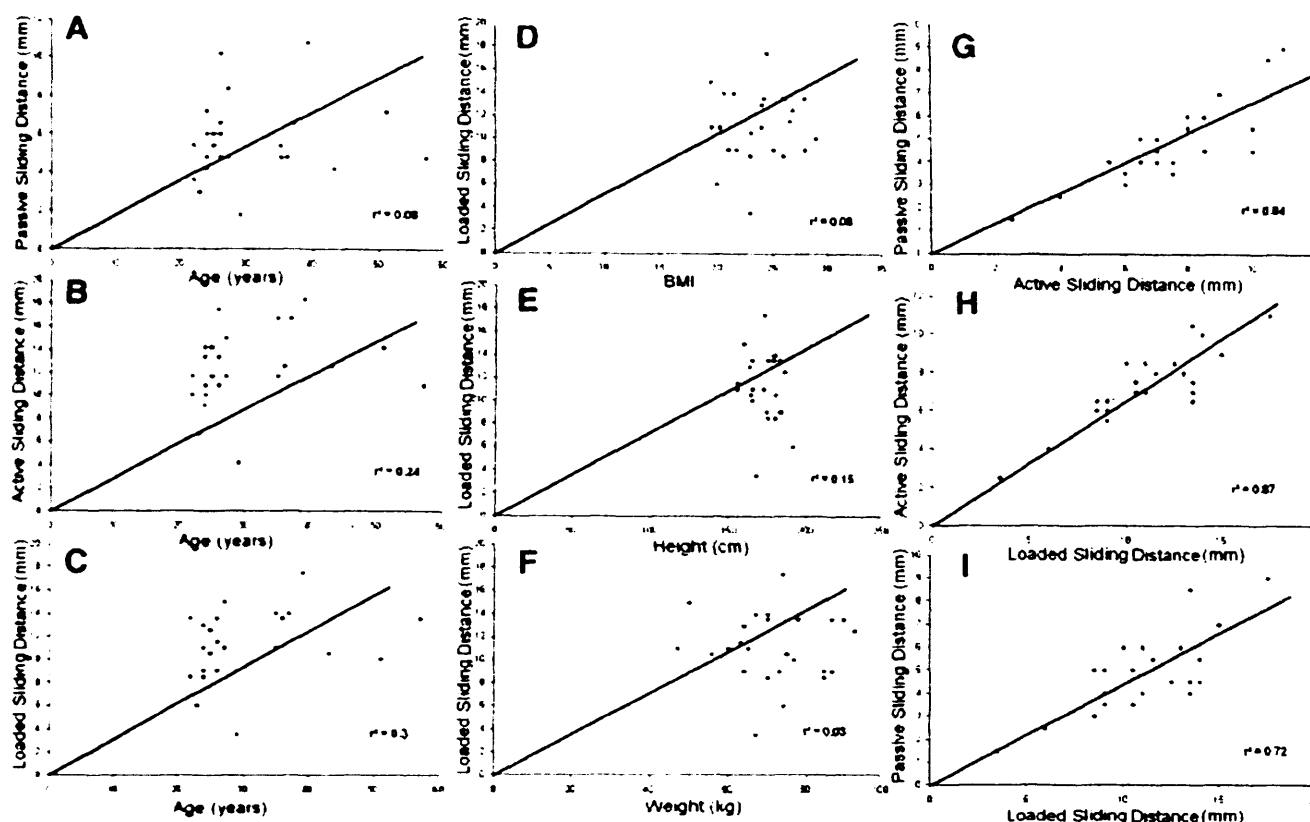


Figure 3. No significant relationship existed between age and (A) passive, (B) active, or (C) loaded ankle flexion. The same was found for (D) BMI, (E) height, and (F) weight. Only loaded flexion sliding distance comparisons are presented for illustration. (G) A strong linear relationship was found between passive flexion and active flexion. (H) Sliding distance increased linearly between active flexion and loaded flexion. (I) Between passive flexion and loaded flexion, sliding distance increased linearly.

Similarly, sliding distance during active ankle flexion was greater than during passive ankle flexion ($p < 0.01$), highlighting a strong linear relationship between Protruding Wedge Sliding Distance (PWSD) and Achilles Tendon (AT) load ($r^2 = 0.87$) (Fig. 3G–I).

DISCUSSION

The literature has suggested that FHL contraction controls movement of the protruding wedge.^{7,10} During the loaded ankle flexion and FHL only, sEMG data showed FHL activities in all volunteers; no wedge motion was recorded during the FHL only. In addition, during passive ankle flexion, protruding wedge motion was present in all volunteers, with no observed FHL contractions. This shows that FHL has no control over wedge motion. Intervolunteer results also showed that wedge sliding distance was not influenced by age, gender, weight, or BMI. Sliding distance increased between passive, active, and loaded ankle flexion indicating that it is influenced by Achilles tendon load. This supports the hypothesis that the protruding wedge serves to assist in subtendinous lubrication, promoting lower levels of wear at high loads.^{7,13} The wedge was observed sliding to the distal extremity of the retrocalcaneal bursa under load, supporting suggestions that it assists in removing dead cells from within the bursal space.⁸

The anchorage of the deep part of the protruding wedge to the calcaneus was also considered to control this motion.⁷ Because wedge motion was recorded against the direction of calcaneal rotation during ankle flexion, motion of the wedge tip is independent of this anatomical connection to the calcaneus. As the tip forms the superior synovial folds of the retrocalcaneal bursa,^{9,12} and the retrocalcaneal region is surrounded by retinaculae and fascia to support the Achilles tendon from excessive kinking,^{7,17} the protruding wedge is still thought to serve to protect the bursa from sudden pressure change during ankle flexion. Wedge motion was observed only when the Achilles tendon insertion angle changed, supporting speculations that its motion is influenced by the bursal pressure change. Further analysis of shape and volume changes may assist in determining other factors that control this motion.

In conclusion, motion of the protruding wedge was independent of FHL activities, gender, age, BMI, height, weight, and foot orientation. No contralateral differences were observed. The wedge moved with changing Achilles tendon insertion angle and the sliding distance of the wedge increased with load, until it reached the most proximal point of the enthesis. The extent of this movement supports concepts that the wedge assists in lubricating the subtendinous region,⁷ reducing the level of wear at high load levels¹³; subsequent benefits may

clude the protruding wedge assisting in removing cellular debris generated by wear and tear within the retrocalcaneal bursa.⁸

REFERENCES

1. Ly JQ, Bui-Mansfield LT. 2004. Anatomy of and abnormalities associated with Kager's fat Pad. *AJR Am J Roentgenol* 182: 147–154.
2. Goodman LR, Shanser JD. 1977. The pre-Achilles fat pad: An aid to early diagnosis of local or systemic disease. *Skeletal Radiol* 2:81–86.
3. Bottger BA, Schweitzer ME, El-Noueam KI, et al. 1998. MR imaging of the normal and abnormal retrocalcaneal bursae. *AJR* 170:1239–1241.
4. Canoso JJ, Liu N, Traill MR, et al. 1988. Physiology of the retrocalcaneal bursa. *Ann Rheum Dis* 43:308–312.
5. Harris CA, Petudo AJ. 2006. Achilles tendon imaging. *Australas Radiol* 50:513–525.
6. Krips R, Brandsson S, Swensson C, et al. 2002. Anatomical reconstruction and Evans tenodesis of the lateral ligaments of the ankle: Clinical and radiological findings after follow-up for 15–30 years. *J Bone Joint Surg Br* 84:232–236.
7. Theobald P, Bydder G, Dent C, et al. 2006. The functional anatomy of Kager's fat pad in relation to retrocalcaneal problems and other hindfoot disorders. *J Anat* 208:91–97.
8. Shaw HM, Santer RM, Watson AH, et al. 2007. Adipose tissue at entheses: the innervation and cell composition of the retromalleolar fat pad associated with the rat Achilles tendon. *J Anat* 211:436–443.
9. Kachlik D, Baca V, Cepelik M, et al. 2008. Clinical anatomy of the retrocalcaneal bursa. *Surg Radiol Anat* 30:347–353.
10. Benjamin M, Redman S, Milz S, et al. 2004. Adipose tissue at entheses: the rheumatological implications of its distribution. A potential site of pain and stress dissipation? *Ann Rheum Dis* 63:1549–1555.
11. Shaw HM, Benjamin M. 2007. Structure-function relationships of entheses in relation to mechanical load and exercise. *Scand J Med Sci Sports* 17:303–315.
12. Morel M, Boutry N, Demondion X, et al. 2005. Normal anatomy of the heel entheses: anatomical and ultrasonographic study of their blood supply. *Surg Radiol Anat* 27:176–183.
13. Theobald P, Byrne C, Oldfield SF, et al. 2007. Lubrication regime of the contact between fat and bone in bovine tissue. *Proc Inst Mech Eng [H]* 221:351–356.
14. Khan Z, Faruqi Z, Ogyunbiyi O, et al. 2006. Ultrasound assessment of internal derangement of the knee. *Acta Orthop Belg* 72:72–76.
15. Dilley A, Odeyinde S, Greening J, et al. 2008. Longitudinal sliding of the median nerve in patients with non-specific arm pain. *Man Ther* 13:536–543.
16. Kachlik D, Baca V, Cepelik M, et al. 2008. Clinical anatomy of the calcaneal tuberosity. *Ann Anat* 190:284–291.
17. Snow SW, Bohne WH. 2006. Observations on the fibrous retinacula of the heel pad. *Foot Ankle Int* 27:632–635.